Electron pair production in p-Be and p-Au collisions at 450GeV/c

Guy Tel-Zur

Particle Physics Department
The Weizmann Institute of Science
Rehovot, Israel.

September 1996

Electron pair production in p-Be and p-Au collisions at 450GeV/c

Guy Tel-Zur

Particle Physics Department
The Weizmann Institute of Science
Rehovot, Israel.

Thesis presented to the Feinberg Graduate School
of the Weizmann Institute of Science for the degree of Ph.D. in Physics

supervisor: Prof. Itzhak Tserruya

September 1996

To Noemi and Etai

Abstract

This thesis deals with the measurements and results of inclusive e^+e^- pair production in p-Be and p-Au collisions at 450GeV/c. The work was performed in the framework of the CERES experiment which is mainly focused to the measurement of low-mass e^+e^- pairs ($m_{\mathrm{e^+e^-}} < 1.5$GeV/c^2) in nucleus-nucleus collisions at the CERN SPS energies. The proton measurements provide an essential reference basis in the search for new phenomena, QGP phase transition and chiral symmetry restoration, predicted to occur in the nucleus-nucleus measurements. Furthermore, the production of lepton pairs in hadronic collisions is an interesting topic in its own right, in particular, due to the long standing claim of an "anomalous" production of e^+e^- pairs below the ρ^0 meson mass. The emphasis of this work is in achieving the best accuracy in the measurements of low-mass electron pairs in p-Be collisions. The main result is that within the experimental errors, dominated by 20% systematical errors in the mass range $200 < m < 600$MeV/c^2, there is agreement between the measured invariant mass spectrum and the expected one from the known hadronic sources, and there is no need to invoke any new or "anomalous" source. We also present first results of low mass e^+e^- pair production in p-Au collisions, which are also reproduced by the known hadronic sources.

יצירת זוגות אלקטרונים בהתנגשויות פרוטון-בריליום ופרוטון-זהב ב- 450GeV/c

תמצית

עבודה זו עוסקת במדידת ובניתוח תוצאות יצירת זוגות אלקטרון-פוזיטרון בהתנגשויות p-Be ו- p-Au בתנע של 450GeV/c. העבודה בוצעה במסגרת ניסוי CERES שעיקרו מדידת זוגות e^+e^- במסה נמוכה, $m<1.5GeV/c^2$, הנוצרים בהתנגשויות גרעין-גרעין באנרגית מאיץ ה- SPS שב- CERN. מדידת התנגשויות הפרוטון משמשת כיחוס לחיפוש תופעות חדשות כגון מעבר פאזה לפלסמה של קווארקים וגלואונים (QGP) ושיחזור הסימטריה הקיראלית האמורות להתרחש בהתנגשויות אולטרא-יחסותיות בין גרעינים כבדים. יתרה מזאת, יצירת זוגות לפטונים בהתנגשויות הדרוניות הינה בעלת עניין בפני עצמה ובפרט בכל הנוגע לטענה העומדת בעינה מזה כשני עשורים בדבר ″אנומליה″ ביצירת זוגות לפטונים בתחום המסה הנמוכה. הדגש בעבודה זו הינו על השגת הדיוק הגבוה ביותר במדידת זוגות e^+e^- בעלי מסה נמוכה בהתנגשויות p-Be. התוצאה העיקרית הינה שבתחום השגיאה הניסיונית (המורכבת מ- 20% שגיאה סיסטמטית) ישנה התאמה בין ספקטרום המסה האינווריאנטית המדוד לבין החזוי על-פי המקורות ההדרוניים הידועים ולכן אין צורך בקיומו של מקור ″אנומלי″ להסברת הספקטרום המדוד. כמו-כן, מוצג ספקטרום המסה של זוגות e^+e^- הנוצרים בהתנגשויות פרוטון-זהב, אשר גם הוא ניתן להבנה על-סמך המקורות ההדרוניים הידועים.

Acknowledgments

I would like to thank all the CERES collaboration members and in particular the following friends and colleagues for their help: Camelia Botaz and and Sara Yasur for the computer administration. Zeev Fraenkel, Peter Glässel, Carlos de los Heros, Andreas Pfeiffer and Evgeny Socol for contributing discussions and in particular to Ilia Ravinovich and Victor Steiner who shared with me writing some significant parts of the analysis and the simulation programs. Finally, very special thanks to my supervisor Prof. Itzhak Tserruya for his help, explanations and support.

♡

Contents

List of Figures

List of Tables

Chapter 1

Physics Background

This work is dedicated to the analysis of e^+e^- pair production ($m_{\mathrm{e^+e^-}} < 1.5$GeV/c^2) in p-Be and p-Au collisions at 450GeV/c measured by the CERES (**Ch**er**e**nkov **R**ing **E**lectron **S**pectrometer) experiment in 1993 at the SPS accelerator at CERN. This chapter deals with the physics background needed for the rest of the work and it gives the motivation for performing the experiment. We begin with a short overview on relativistic heavy ion collisions which is the general framework of the CERES experiment.

1.1 The interest in dilepton pairs

1.1.1 Ultra relativistic heavy-ion collisions

The relatively new interdisciplinary field of ultra-relativistic heavy ions collisions has emerged from the domains of particle physics and nuclear physics. Combining the elementary-interaction aspect of high-energy physics with the macroscopic-matter aspect of nuclear physics, the subject of heavy-ion collisions is the study of *bulk matter* consisting of strongly interacting particles (hadrons/quarks). It may therefore be dubbed 'condensed matter physics' of elementary particles. The energy scale is given by Λ_{QCD} or the pion mass, both of the order of 150MeV. What makes this field particularly interesting is the prediction of QCD that at high energy densities matter is expected to undergo a phase transition to a new state called quark-gluon plasma[1] (QGP) where quarks and gluons are free in a volume large

---

[1] There is an enormous literature on QGP. A coverage of both theoretical and experimental aspects of the subject can be found in the Quark-Matter proceedings Refs. [3–13].

compared to the hadron size. Chiral symmetry restoration is also predicted to occur under those conditions. At low energy density, quarks and gluons are bound by the strong force into colorless objects, the hadrons (confinement). When increasing the energy density by increasing the temperature ('heating') or the matter density ('compressing'), a phase transition occurs, where partons are deconfined and chiral symmetry is approximately restored (QGP onset may take place at a different critical temperature than chiral symmetry restoration onset). In chiral symmetry restoration the quarks are expected to loose a large fraction of their mass and therefore a decrease in the mesons mass is expected. This subject is reviewed in [15]. The study of the phase diagram of strongly interacting matter is not only of interest to study and test QCD, but it might also shed light on important aspects of cosmology and astrophysics. The early universe presumably underwent the same phase transition $\sim 10^{-5}$ seconds after the Big-Bang. Thus the study of extreme states of matter created in high-energy nuclear collisions provide us with an opportunity of gaining insight into many important aspects in different fields of physics. The phase transition is predicted to occur at a baryon density of $10 - 15$ times the normal nuclear matter density or at a temperature of $\mathrm{T}_c = 150 - 200$MeV.

Among the best probes of the interior of the quark-gluon plasma during the earliest and the hottest phase of the collision are the electromagnetic channels, i.e. dileptons and photons, and therefore there is a considerable interest in lepton pair production in nuclear collisions. The advantage of dileptons as probes for QGP was emphasized by Shuryak [16,17]: the argument is that since dileptons interact only electro-magnetically, their mean free path is large compared to the size of the system formed in the collision. Therefore, once a lepton pair is produced, it will leave the interaction region and reach the detector without any further interactions carrying information from inside the interaction volume. The experimental situation on electromagnetic probes is reviewed in Refs. [18,19].

There are several interesting things to be observed in dilepton production in heavy-ion collisions:

- Thermal radiation: The thermal radiation can appear as virtual photons (dileptons) or as real photons and it can be emitted in the QGP phase as $q\bar{q}$ annihilation and also in the hadron gas (HG) phase, essentially as $\pi^+\pi^-$ annihilation. The first one might be observable only in the mass region above 1GeV/c^2 producing an essentially exponential spectrum with a slope param-

---

For a recent review of experimental results see [14].

eter reflecting the temperature of the system [20]:

$$\frac{d^2\sigma}{dm^2dy}\Big|_{y=0} \sim \exp\left(-m/T\right)$$

The $\pi^+\pi^-$ annihilation on the other hand, rises from threshold at $m = 2m_\pi$ and is dominated by the ρ^0 pole in the pion form factor; it is therefore expected to contribute in the region around and below the ρ^0-meson mass.

- The ϕ meson. The ϕ meson has a life time of $\tau = 48$fm/c, sufficiently large to decay outside the interaction volume. The ϕ meson, consisting of $s\bar{s}$ quarks, was suggested as an excellent probe of the QGP due to an expected strangeness enhancement and to the absence of the OZI rule which in regular matter suppress ϕ production [21].

- Lepton pairs from hadronic sources in the invariant mass range between 0.5–1GeV are important signals of the dense hadronic matter formed in the collision. They provide information about possible medium modifications, i.e. changes in the resonances widths and positions which are expected if chiral symmetry is restored [22, 23]. In particular, such changes could be detectable in the ρ^0 peak due to its short lifetime of 1.3fm/c [24, 25]. Furthermore, if the interacting system lives much longer than 2fm/c, as was pointed out by Heinz and Lee [26], several generations of thermal ρ^0 mesons would contribute to the spectrum, enhancing the ρ^0 yield. The ρ^0/ω can therefore serve as a "clock" to determine the lifetime of the system.

1.1.2 Lepton pair production in hadronic collisions

Lepton pairs produced in hadronic collisions have their own interest and they have been a subject of intensive studies over the last two decades. A schematic view of the e^+e^- invariant mass spectrum is shown in Figure 1.1. One can distinguish three regions in this spectrum:

1. The high mass region at $m \geq 3$GeV/c^2 includes the J/Ψ and the Ψ' resonances and a continuum dominated by Drell-Yan (D-Y) mechanism [27, 28].

2. The intermediate mass region, $m_\phi < m < m_{J/\Psi}$, is dominated by the semi-leptonic decay of the charmed mesons $D\bar{D}$ and by the D-Y process.

3. The low mass region at $m \leq 1\text{GeV/c}^2$, where most of the cross section lies, includes the Dalitz decays of the π^0, η, $\eta\prime$ and ω and the resonance decay of the ρ^0, ω and ϕ. These sources are considered in detail in the next section and in Chapter 4 in the context of an e^+e^- pair generator MC program which we have developed.

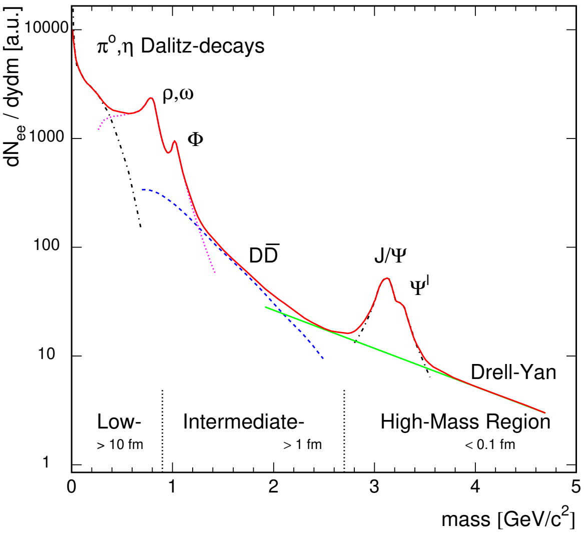

Figure 1.1: Schematic view of the e^+e^- mass spectrum in p-p collisions (not to scale).

This work deals with the low mass part of the e^+e^- mass spectrum. This region is of particular interest. From about 1976 several groups reported an excess in the dilepton mass continuum below the ρ^0 over what would be expected from Dalitz decays of known hadronic resonances. This continuum has been seen in both e^+e^- and $\mu^+\mu^-$ channels. A compilation of data from several experiments (covering a variety of systems and different colliding energies), with all known Dalitz decay contributions subtracted, is shown in Figure 1.2 [1]. The cross section has been normalized to the pion production at central rapidity[2]. Several features should be noted:

- The normalized data is independent of $\sqrt{s}$ in sharp contrast to the scaling with $m/\sqrt{s}$ for the Drell-Yan mechanism ($\sqrt{s}$ is the center of mass energy[3]).

---

[2] Rapidity and other kinematic variables are defined in Appendix A.

[3] For a list of symbols used in this work refer to Appendix E.

- The mass spectrum favors $\sim 1/m^2$ dependence.
- The integrated yield in the mass range $200 - 600$MeV/c^2 is about a factor of 3 above that expected from known Dalitz decays.

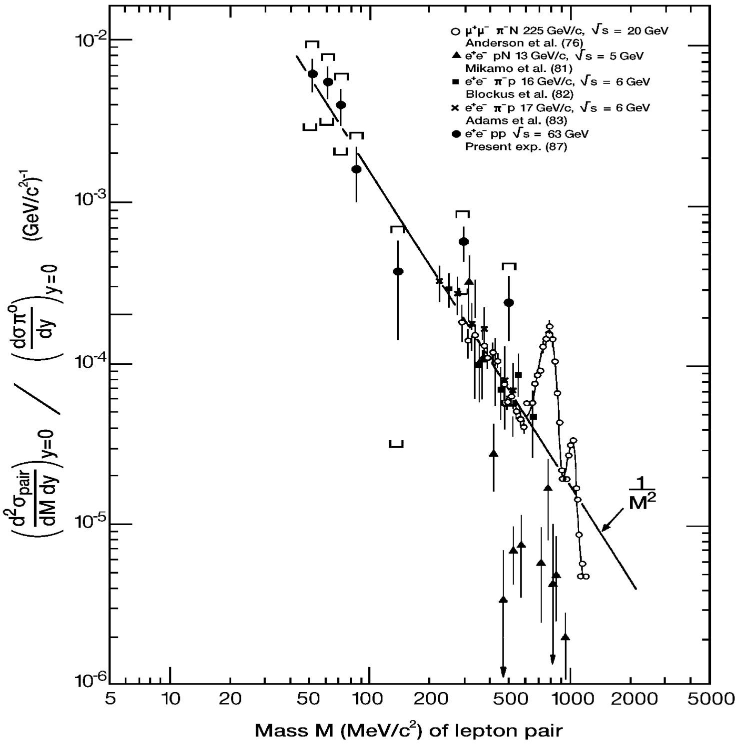

Figure 1.2: Dileptons mass spectrum in hadron-hadron collisions. (A compilation of results from 1976 until 1987, see Refs. in Table 1.1) [1].

This excess got the nickname "anomalous" pair production. The reports about anomalous pairs are listed in Table 1.1. The origin of these leptons was not well understood. One proposed explanation was the so-called soft annihilation model by V. Cerny et al. [41] following an idea by Bjorken and Weisberg [42]. In this model low-mass lepton pairs are created through the annihilation of many soft quarks and antiquarks produced during the hadronic collision (in contrast to the hard Drell-Yan process in which the annihilation occurs among the partons initially present in the incoming hadrons).

Collaborations	**Remarks**
Chicago-Princeton [29, 30]	$\mu^+\mu^-$ pairs from 150GeV p and π^- on Be at Fermilab
Bunnell et al. [31] Haber et al. [32]	$\mu^+\mu^-$ pairs from 15.5GeV/c $\pi^\pm$p at SLAC
SLAC-Duke-Imperial College [33]	e^+e^- pairs from 18GeV/c $\pi^\pm$p at SLAC.
Clark et al. [34] and Chilingarov et al. [35]	e^+e^- pairs from pp collisions at $\sqrt{s}$ = 53,63 at the CERN ISR
LASS spectrometer SLAC-J. Hopkins-Caltech [36, 37]	e^+e^- pairs from 16GeV/c π^-pGeV/c at SLAC
Mikamo et al. [38]	e^+e^- pairs from 13GeV/c p-Be collisions at KEK
Stony Brook - BNL-Pennsylvania [39, 40]	e^+e^- pairs from 17GeV/c π^-p

Table 1.1: Low mass dilepton experiments which reported on anomalous low-mass pair production.

The elucidation of this topic is one of the main focus of the present work, and will be discussed in Chapter 5 together with the recent results from the HELIOS collaboration.

1.2 Sources of electron pairs in the low mass region

In the mass region $m \leq 1.5$GeV/c^2 we can distinguish 2 main categories of electron pair sources:

- Resonance decays.
- Dalitz decays.

An additional source of e^+e^- pairs comes from hadronic bremsstrahlung. It contributes at the very low masses, and is practically negligible in our case due to the p$_T$ cut of 50MeV/c applied in the analysis to the e^- and the e^+ tracks, see Chapter 3. Finally, we also mention the semi-leptonic decays of charm mesons D, $\bar{D}$, which give also a negligible contribution in the mass range $m < 1$GeV/c^2 [43].

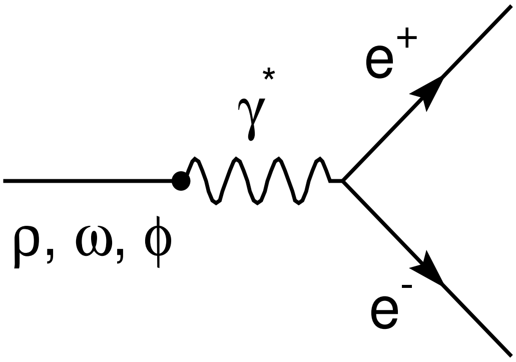

Figure 1.3: Diagram of the resonances decay $\rho, \omega, \phi \rightarrow e^+e^-$.

1.2.1 Resonance decays

In the mass range covered by CERES, the vector mesons which decay directly into e^+e^- pairs are:

- $\rho^0 \rightarrow e^+e^-$
- $\omega \rightarrow e^+e^-$
- $\phi \rightarrow e^+e^-$

The decay diagram is shown in Figure 1.3. The ρ^0 belongs to an iso-triplet together with the ρ^+ and the ρ^- (Isospin=1). It consists of u and d quarks in the following combination:

$$|\rho >= \frac{1}{\sqrt{2}}(|u\bar{u} > -|d\bar{d} >) \tag{1.1}$$

The physical ω and ϕ mesons are built from a mixture of the ϕ_0 and the ϕ_8 members of the singlet and octet families composing the vector mesons nonet:

$$|\phi >= |\phi_0 > \sin\theta - |\phi_8 > \cos\theta \tag{1.2}$$

$$|\omega >= |\phi_8 > \sin\theta + |\phi_0 > \cos\theta \tag{1.3}$$

The ϕ_0 and ϕ_8 quark composition is:

$$|\phi_0>= (|d\bar{d}> + |u\bar{u}> + |s\bar{s}>)/\sqrt{3} \tag{1.4}$$

$$|\phi_8>= (|d\bar{d}> + |u\bar{u}> - 2|s\bar{s}>)/\sqrt{6} \tag{1.5}$$

Comparing the measured masses of the ω and ϕ assuming that the (mass)^2 is given by the matrix element of the Hamiltonian between the states, i.e., $M_i^2 =< i|H|i >$ (see [44]) one gets $\theta \simeq 40^0$. For the particular case of $\sin\theta = 1/\sqrt{3},\ \theta \simeq 35^0$ the ω and ϕ become:

$$|\phi>= |s\bar{s}> \tag{1.6}$$

$$|\omega>= (|u\bar{u}> + |d\bar{d}>)/\sqrt{2} \tag{1.7}$$

that is the ϕ is mainly built from strange and anti strange quarks and the strangeness contribution to the ω is negligible. In addition, these expressions predict similar masses for ρ^0 and ω as well as larger mass for the ϕ - as observed.

1.2.2 Dalitz decays

The low mass range ($m \leq 0.65$GeV/c^2) e^+e^- spectrum is dominated by Dalitz decays:

- $\pi^0 \rightarrow e^+e^-\gamma$
- $\eta \rightarrow e^+e^-\gamma$
- $\eta\prime \rightarrow e^+e^-\gamma$

The vector meson ω has an additional decay (Dalitz-π^0) $\omega \rightarrow e^+e^-\pi^0$. The corresponding decay diagrams are shown in Figures 1.4 and 1.5.

The π^0, η and $\eta\prime$ are pseudo-scalars, $J^P = 0^-$, The π^0 quark assignment is:

$$|\pi^0>= (|u\bar{u}> + |d\bar{d}>)/\sqrt{2}$$

The η and the $\eta\prime$ are mixed states of the $|\eta_0>$ and the $|\eta_8>$ states in a similar way as was discussed in the case of the ω and the ϕ vector mesons:

$$|\eta>= |\eta_8> \sin\theta + |\eta_0> \cos\theta$$

$$|\eta\prime>= |\eta_0> \sin\theta - |\eta_8> \cos\theta$$

Therefore the η and $\eta\prime$ quark composition is:

$$|\eta >= (\frac{\cos\theta}{\sqrt{6}} - \frac{\sin\theta}{\sqrt{3}})|u\bar{u}> +(\frac{\cos\theta}{\sqrt{6}} - \frac{\sin\theta}{\sqrt{3}})|d\bar{d}> +(\frac{-2\cos\theta}{\sqrt{6}} - \frac{\sin\theta}{\sqrt{3}})|s\bar{s}>$$

$$|\eta\prime >= (\frac{\sin\theta}{\sqrt{6}} + \frac{\cos\theta}{\sqrt{3}})|u\bar{u}> +(\frac{\sin\theta}{\sqrt{6}} + \frac{\cos\theta}{\sqrt{3}})|d\bar{d}> +(\frac{-2\sin\theta}{\sqrt{6}} + \frac{\cos\theta}{\sqrt{3}})|s\bar{s}>$$

where a mixing angle of 11^0 gives the best agreement with the measured masses.

The e^+e^- pair production occurs via the decay of a virtual photon. Since in these cases the decaying particle is a composite one its form factor[4] must be taken into account, i.e. for the Dalitz decays the cross section is enhanced over that of a pure QED process. This is treated according to the Vector Dominance Model (VDM) which was first introduced by J.J. Sakurai in 1960 [45] and then was subsequently developed by a number of other workers (see Ref. [46] for a general review on the subject). The model is based on the assumption that during the photon-hadron interaction the incident photon is equivalent to a combination of vector mesons (which have the same quantum numbers as the photon, $J^{PC} = 1^{--}$). At high energy the electromagnetic current of the quarks is directly visible; however at low energies, where hadrons (rather than quarks) are the relevant degrees of freedom, the currents are realized in the form of vector mesons (ρ^0, ω, ϕ, ...). The

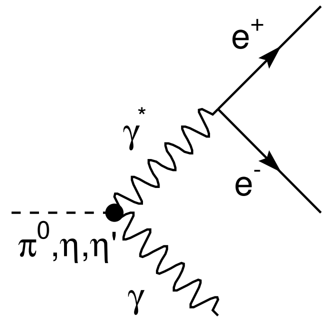

Figure 1.4: $\pi^0, \eta, \eta\prime \rightarrow e^+e^-\gamma$.

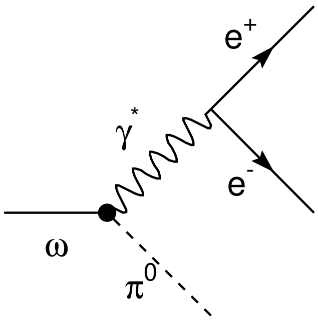

Figure 1.5: $\omega \rightarrow e^+e^-\pi^0$.

---

[4] The form factor, $F(q^2)$, is defined as the Fourier transform of the scatterer's charge distribution where q^2 is the hadronic 4-momentum transfer. It is related to the cross section according to $d\sigma/dq^2 = (d\sigma/dq^2)_{\mathrm{point}} \cdot [F(q^2)]^2$.

dominance of the vector mesons at low energy suggests the current-field identity:

$$J_\mu^{e.m.} = \sum_{v=\rho^0,\omega,\phi} \frac{em_v^2}{2g_{v\gamma}} v_\mu(x)$$

where $v_\mu(x)$ is the vector meson field. The corresponding Feynman VDM diagram is shown in Figure 1.6.

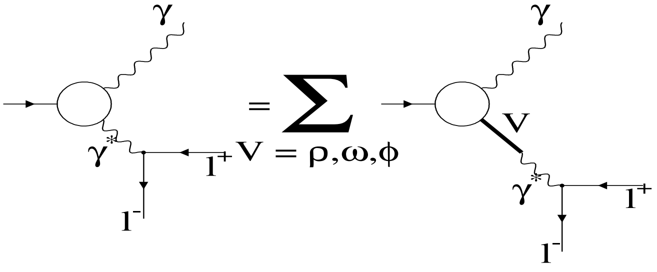

Figure 1.6: VDM diagram.

The coupling constants, g, are determined experimentally. However, based on the quark assignments for the vector mesons, see Equations 1.1,1.6 and 1.7, it is possible to estimate $1/g_{\rho\gamma}$: $1/g_{\omega\gamma}$: $1/g_{\phi\gamma}$ using the Van Royen-Weisskopf formula (see for example Ref. [44]):

$$\Gamma(v \to l^+l^-) = \frac{16\pi\alpha^2Q^2}{m_v^2}|\Psi(0)|^2$$

and upon assignment of the u,d and s charges into Equations 1.1, 1.7 and 1.6 one gets

$$\rho^0 : [\frac{1}{\sqrt{2}}(\frac{2}{3} - (-\frac{1}{3}))]^2 = \frac{1}{2}$$

$$\omega : [\frac{1}{\sqrt{2}}(\frac{2}{3} - \frac{1}{3})]^2 = \frac{1}{18}$$

$$\phi : (\frac{1}{3})^2 = \frac{1}{9}$$

and therefore:

$$1/g_{\rho\gamma} : 1/g_{\omega\gamma} : 1/g_{\phi\gamma} = 9 : 1 : 2$$

This means that the photon behaves as if it were 75% ρ^0, 8% ω and 17% ϕ. Thus the ρ^0 is the most important vector meson in mediating the photon-hadron interactions.

Figure 1.7 shows the square of the form factor of the η, ω and $\eta\prime$ Dalitz decays into dimuons, where the dots are the experimental points[5], the dashed curve is a VDM fit and the solid curve is the result of fitting the experimental data with a pole formula $|F(q^2)|^2 = (1 - q^2/\Lambda^2)^{-2}$ (see Chap 4 for the values of Λ). The VDM reproduces reasonably well the η and $\eta\prime$ data. However, there is a dramatic discrepancy between the experimental data points and the VDM prediction in the case of the ω electromagnetic form factor; for example, at a mass of 0.4GeV/c^2 the data points are higher than the VDM prediction by a factor of $\sim$ 10 [48]. The origin of this behavior is unclear and can not be explained by other models like the generalized-VDM in which heavier vector mesons are taken into account.

1.3 The CERES experiment

CERES is an experiment dedicated to the measurement of electron pairs and direct photons produced in hadron and nuclear collisions at the CERN SPS energies. The main motivation is to look for the QGP phase transition and/or chiral symmetry restoration. CERES is optimized to study the pair continuum in the low mass region up to $\sim$ 1.5GeV/c^2 and the vector mesons ρ^0, ω and ϕ . The apparatus also allows high-statistic studies of high-p$_T$ pions and of QED pairs produced in distant nuclear collisions. In the search for new physics, it is necessary to have a very good understanding of all the contributions from the known hadronic sources. This, together with the lack of precise quantitative predictions and the anomalous low-mass pairs discussed previously calls for a systematic approach measuring electron pairs in p-p and p-A collisions as the basis for identifying any possible deviation from the known physics in A-A collisions. In this spirit, the CERES program includes the measurement of the following systems: 450GeV/c p-Be, 450GeV/c p-Au, 200GeV/u S-Au and 160GeV/u Pb-Au collisions, refer to Table 1.2 for a brief summary.

The measurement of e^+e^- pairs in relativistic heavy-ion collisions is a very difficult one. In fact, CERES is the first experiment which measures e^+e^- pairs in

---

[5] There is only one measurement of the ω form factor performed by the Lepton-G experiment, based on 60 events [47].

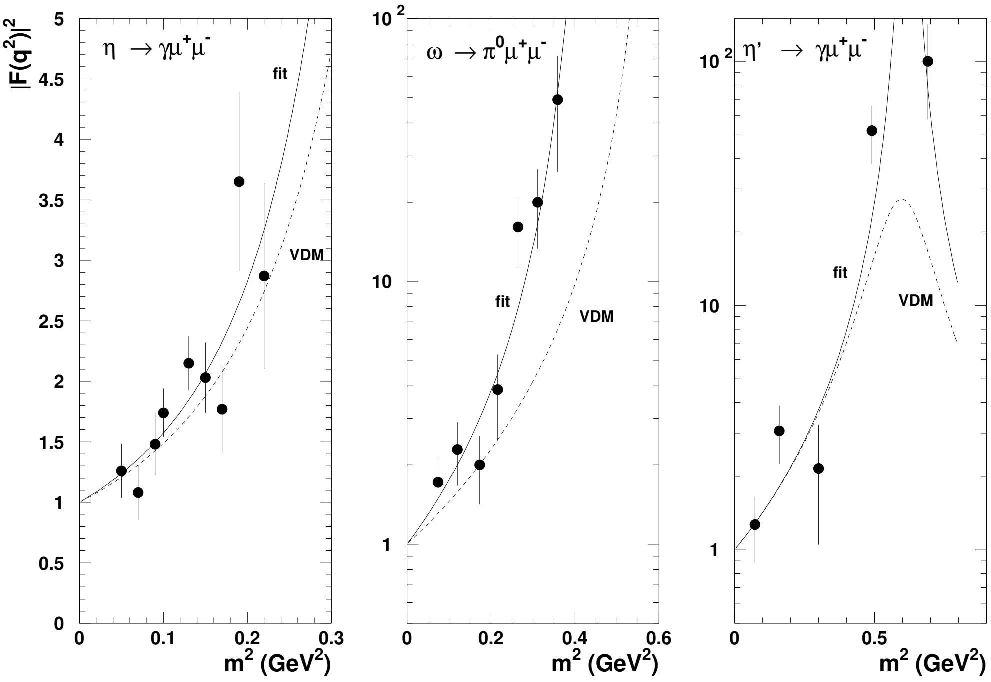

Figure 1.7: The square of the form factor of the η, the ω and the $\eta\prime$ Dalitz decays into dimuons.

nuclear collisions at the SPS energies. The main difficulty is the detection of a very weak signal with a production probability of $\sim 10^{-5}$ relative to pions in the environment of other electrons coming from trivial sources such as π^0 Dalitz decay and γ conversions and in the presence of hundreds of charged particles per event. This is a great experimental challenge. The CERES collaboration was the first group to propose and build a novel spectrometer that can cope with this difficult task. The spectrometer and its main properties are described in Chapter 2.

1.4 Goals of the 1993 p run

In the 1993 p run, the CERES spectrometer was used together with the TAPS electromagnetic calorimeter (see Section 2.2.4). Three types of measurements were carried out simultaneously:

- inclusive e^+e^- pair production (CERES stand alone data).
- inclusive γ production (TAPS stand alone data).
- $e^+e^-\gamma$ coincidence measurement (TAPS + CERES).

This proton run had 4 fold goals [49]:

1. To clarify the anomalous low-mass excess controversy as was discussed in section 1.1.2. At the time of planning the p run of 1993 HELIOS/1 presented preliminary results which showed no evidence for an excess in the dilepton mass spectrum [43]. This striking results which contradicted so many previous claims of anomalous pair production called for a confirmation by another independent measurement. In addition, the CERES measurement aimed at reaching better accuracy.

2. The TAPS stand alone measurements allow to determine individual meson production cross section through their $\gamma\gamma$ decay channels. Similar information can also be obtained by fully reconstructing the mesons through their $e^+e^-\gamma$ Dalitz decay mode. This allows a detailed understanding of the separate contributions to the inclusive e^+e^- spectrum and in particular of the $\eta \rightarrow e^+e^-\gamma$ channel which dominates the inclusive mass spectrum in the mass range $m = 0.2 - 0.6$GeV/c^2.

3. The coincidence measurements of CERES+TAPS allow to measure the ω form factor and to determine with a better accuracy whether the data are compatible with the VDM or not.

4. The p-Be and the p-Au measurements are important parts of the CERES systematic program. They serve as a reference for the other measurements of heavier systems, the S-Au and the Pb-Au as discussed previously.

My thesis deals with the p 1993 run and it is mainly focussed on the data analysis and the results on the inclusive e^+e^- pair production in p-Be and p-Au collisions.

year	**collision system**	**projectile mom./nuc. (GeV/c)**	$\mathbf{y_{cm}}$
1993	p-Be	450	2.90
1993	p-Au	450	2.36
1992	S-Au	200	2.57
$1994-6$	Pb-Au	160	2.92

Table 1.2: CERES systematic program. The center of mass rapidity was calculated using a simple geometrical model taken from [2].

Chapter 2

The CERES spectrometer

"Down the rabbit hole" - L. Carroll [50]

This chapter describes the difficulties in performing the CERES experiment and the unconventional spectrometer that was designed and built in order to overcome these difficulties. We also give a description of the trigger scheme used in the 1993 run and a quantitative account of the spectrometer performance in this run.

2.1 The Experimental Challenge

The measurement of e^+e^- pairs in hadronic collisions represents an experimental challenge because of the following 3 reasons:

- The need to be sensitive to a very weak source of e^+e^- pairs which for known hadron decays is at the level of $\sim 10^{-5}e^+e^-/\pi^0$ for $m > 200$MeV/c^2.
- The need to detect the e^+e^- pairs in the presence of many other charged particles, $dn_{ch}/d\eta \sim 4$ in p-Be , $dn_{ch}/d\eta \sim 7$ in p-Au, $dn_{ch}/d\eta \sim 150$ in central S-Au collision and up to $dn_{ch}/d\eta \sim 500$ per unit of rapidity for central Pb-Au collisions.
- and in the presence of a relatively much larger source of pairs originating from the Dalitz decays of π^0 and the conversion of γ rays which have a production probability of $\sim 10^{-2}/\pi^0$. They are the main sources for the combinatorial background which is the *problem* of this experiment. The combinatorial background arises from the fact that a priori the detected electron tracks do not preserve information about their parent particle. In an ideal detector with 100% track reconstruction efficiency, this would not be a problem, since the tracks from conversions and π^0 Dalitz decays form pairs with distinctive characteristic patterns (very small opening angle and very small mass). Therefore, once such a pair is recognized its two tracks are not paired to any other track of the same event. However, in a real detector, there is a finite track reconstruction efficiency and therefore, inevitably, single tracks from unrecognized conversions and π^0 Dalitz decays are combined to pairs with other tracks giving rise to the combinatorial background. The combinatorial background becomes much more severe at high multiplicities since it is proportional to the square of the number of charged particles, n_{ch}, while the signal from hadronic sources itself rises only linearly with n_{ch}.

2.2 Overall design of the CERES spectrometer

To cope with the above difficulties the CERES collaboration has developed a spectrometer with unique properties that are described in this section. The spectrometer, as used in the p run of 1993, is shown schematically in Figure 2.1. The essential components are two Ring Imaging Cherenkov detectors (RICH) - one situated before, the other after a short superconducting double solenoid and two silicon detectors: the first is a 64-pad detector (SiPD) which provides the interaction trigger, and the other is a radial drift chamber (SiDC) which provides a more precise event characterization off line and can be used to help the pattern recognition of RICH-1. The ring images are read out by UV-sensitive gas detectors consisting of three amplification stages, two Parallel-Plate Avalanche Chambers (PPAC) and one Multi-Wire Proportional Counter (MWPC) . The magnetic field provides an azimuthal kick between the two RICH radiators. The main coils and the outer warm correction coils shape the field lines such that the first RICH has practically zero field, and the second RICH has straight field lines pointing to the target i.e. parallel to the trajectories of the particles and therefore not affecting them (a few field lines are drawn in the lower part of Figure 2.1). The spectrometer covers the interesting region $2.1 < \eta < 2.65$ near mid-rapidity with 2π azimuthal symmetry and with a broad range of transverse momentum, p_T.

This is a rather unconventional design, in the sense that there is no real tracking of the particles, since a RICH detector measures only the direction of the particle not its origin. The electron identification is provided by the ring radius (with redundancy since the particle is identified in RICH-1 and RICH-2) whereas the charge and momentum are determined by the azimuthal displacement of the rings between RICH-1 and RICH-2.

The spectrometer has 4 unique properties that allow it to handle the difficult task of measuring the rare e^+e^- signal in spite of the huge background.

• Hadron blind: The radiators of the RICH detectors are filled with CH_4 at atmospheric pressure which has a γ_{th} value of $\gamma_{th} \simeq 32$ and are thus insensitive to most of the hadrons. The lightest hadron, the pion must have a momentum, $p > 4.5$GeV/c in order to produce Cherenkov photons. In addition to that, a pion will need to have a momentum $p > 14$GeV/c in order to produce a Cherenkov ring with a radius $R > 95\%$ of the saturated radius[1].

• UV-detectors location: The UV-photon detectors are located upstream of the target, i.e. outside the huge flux of forward-going particles.

• Minimum amount of material inside the spectrometer: In order to minimize γ conversions into e^+e^- pairs, the amount of material in the spectrometer acceptance is minimized down to a level of $< 1\%$ of a radiation length (not including the target). A list of materials and the corresponding radiation lengths is given in Table 2.3. An additional benefit of minimizing the material is the reduction of the

---

[1] The saturated Cherenkov ring radius is obtained as the particle speed approaches the speed of light. see Appendix B for basic Cherenkov radiation formulae.

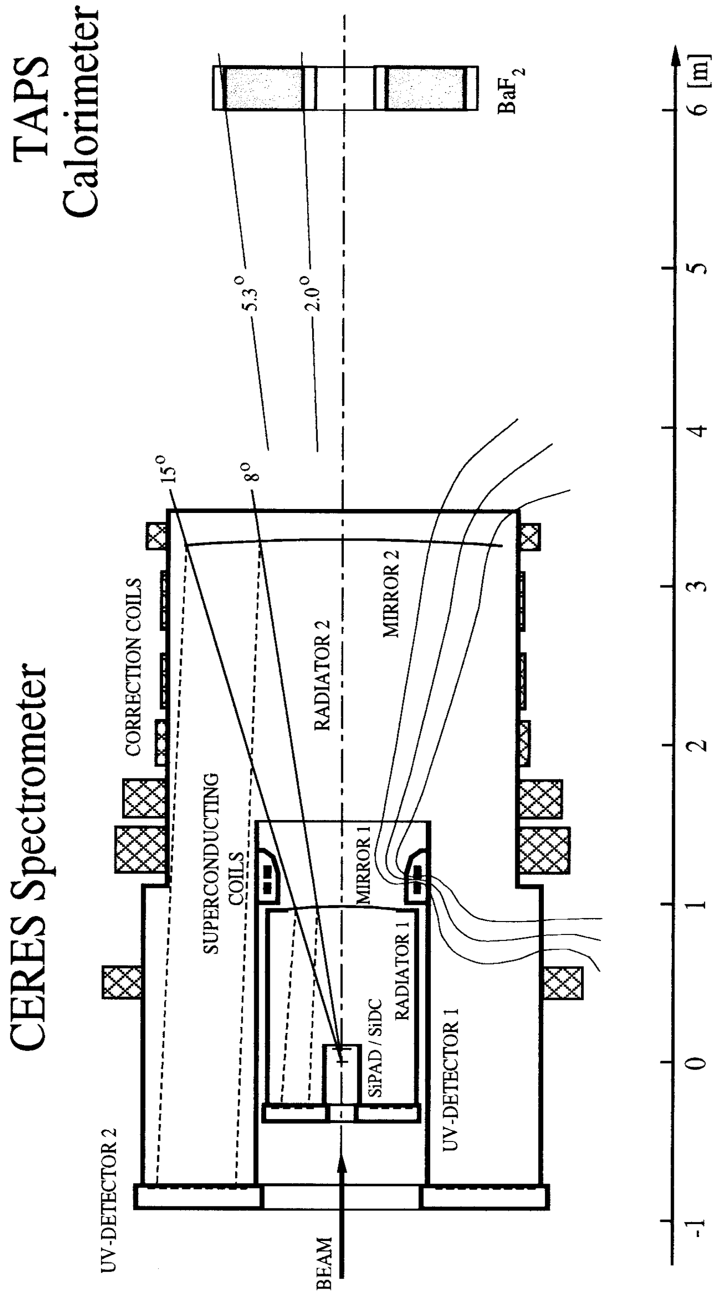

Figure 2.1: Schematic view of the CERES spectrometer with the TAPS calorimeter.

	RICH-1	**RICH-2**
η range	$1.88 - 2.81$	$2.03 - 2.65$
$\Delta\eta$	0.93	0.62
$< \eta >$	2.34	2.34
radiator length (cm)	90	175
radiator gas	CH_4	CH_4
$\gamma_{\rm th}$ (measured)	31.4	32.6
windows	CaF_2	quartz
RICH band width (eV)	$6.1 - 8.5$	$6.1 - 7.4$

Table 2.1: Specification of the RICH detectors.

multiple-scattering the electrons suffer.

- Magnetic field shaping The magnetic field shape is of particular importance. It preserves the original direction of the particles in RICH-1 thereby allowing to recognize conversions and π^0 Dalitz decays by their small opening angle.

2.2.1 RICH detectors

An electron produced in the target emits Cherenkov photons while traversing the radiator volume filled with CH_4. The Cherenkov light is reflected backward by a spherical mirror producing a ring image on the UV-detectors, located at the mirrors focal plane. The principle of formation of the ring image is demonstrated in Figure B.1.

The specifications of the two RICH detectors are summarized in Table 2.1. The spectrometer's acceptance is given by RICH-2 which covers the pseudo rapidity range $2.03 \leq \eta \leq 2.65$. RICH-1 has a somewhat larger acceptance because of its role as a veto detector: a π^0 Dalitz decay for which only one track is inside the fiducial acceptance, can be recognized by the presence of a close-by ring in the veto area of RICH-1.

In order to minimize e^+e^- pair production by γ conversions in UV-2 and to reduce multiple-scattering, the mirror of RICH-1 is made of only 1.1mm ($0.41\%X/X_0$) thick carbon fiber. It is built in one piece held only at the outer circumference. The second mirror is not constrained by the above requirement and therefore it is built from a standard glass, 6mm thick, segmented azimuthally into pieces.

The radiator and the UV detector are separated by a UV transparent window.

RICH-1 has a CaF_2 window (which has an upper cut-off at 8.5eV) whereas RICH-2 has a quartz window (cut-off at 7.4eV). The larger bandwidth of RICH-1 compensates for its shorter radiator length, keeping the performance of the two RICH detectors similar in terms of photons per ring (see Section 2.4.2). The average values of γ_{th} (the Lorentz factor for the threshold emission of Cherenkov photons) over the band width of the RICH detector are also given in Table 2.1.

2.2.2 UV detectors

The UV detectors are gas type chambers consisting of 3 amplification stages, two Parallel-Plate Avalanche Chambers (PPAC) and a Multi-Wire Proportional Counter (MWPC) operated with $94\%/6\%$ mixture of He/CH_4 and saturated vapor pressure of TMAE [Tetrakis (dimethylamine) ethylene] which is the photo-sensitive agent. In order to achieve a sufficient partial pressure, the TMAE is heated to 40^o, but in order also to prevent gas condensation and to avoid temperature gradients the whole spectrometer is operated at 50^o. The layout of the UV detectors is shown in Figure 2.2.

A Cherenkov photon entering the detector is converted into an electron by photo-ionization of a TMAE molecule. The conversion gap has a length of 15mm, ensuring an electron conversion efficiency of 90%[2]. The photo-electron drifts by the electric field to the first PPAC. The PPAC electrodes are made of stainless steel mesh of 50μm wire and a 500μm spacing glued to two concentric rings made of G10. There are no spokes connecting the two rings. Instead, the two rings keep the tension of the mesh and in turn the mesh keeps the two rings concentric. The resulting avalanche then drifts and is further amplified by the second PPAC. Then, a third amplification takes place in the MWPC. The MWPC consists of a mesh cathode and then a wired anode plane, followed by a second cathode which is the pad array readout. The anode plane of the MWPC is a wire plane divided azimuthally in 10 sectors (16 in UV-2) by radial spokes connecting the inner and outer frame. The wires are made of gold-plated tungsten, having a 30μm diameter and arranged with $2(3)$mm spacing in UV-1(UV-2). The spokes define the wire geometry (the wires are parallel to the central radius within a each sector) and provide the mechanical stability that the wires alone cannot supply.

---

[2] The photon mean free path in 40^0 saturated vapor pressure of TMAE was measured to be 6.6 ± 0.2mm [51].

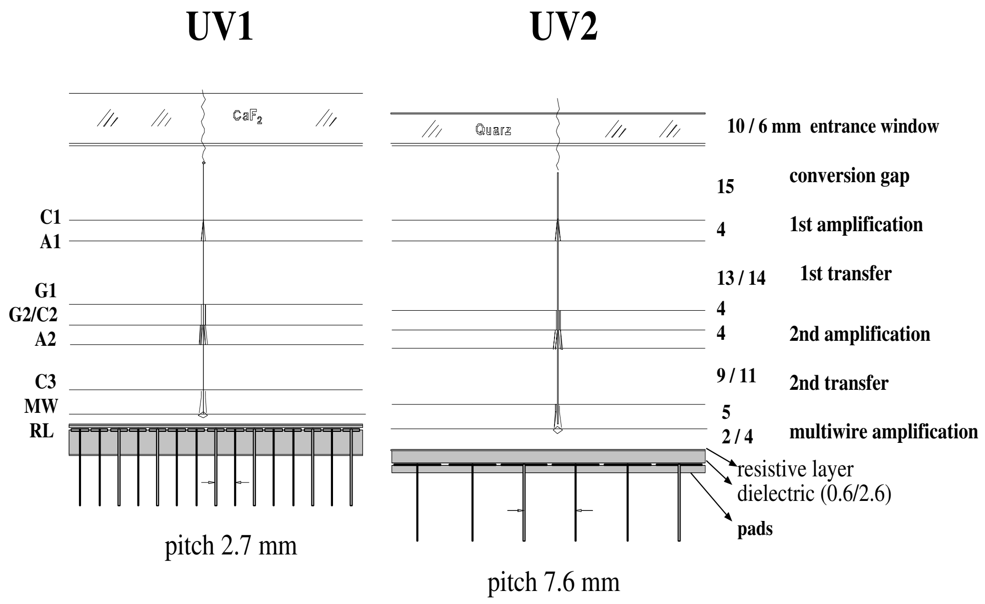

Figure 2.2: A schematic view of the UV detectors.

Pad readout

The avalanche in the wire amplification stage induces a positive signal on square pads (2.74×2.74mm^2 in UV-1 and 7.62×7.62mm^2 in UV-2) which are arranged on the backplane of the gas detector. In order to keep the pads at ground potential and to hermetically close the detector gas volume, the pad structure is covered with an insulating dielectric layer which is coated with a high ohmic Resistive Layer (RL). This layer defines the high voltage potential and is transparent for the fast signals induced by the avalanches. There are about $50,000$ pads in each detector. The pads are grouped into 256 (121) modules. The modules are built from 64-channel VLSI/CMOS amplifier and multiplexer chips, called CAMEX64A, and are plugged directly onto the detector backplane covering the whole acceptance . In RICH-1 the amplified analog signal is converted in the module into 256 digital levels. Reading the pad information is done in parallel by $16(14)$ chains in UV-1 (UV-2), where all pads with the same index of each module are read simultaneously.

	UV-1	**UV-2**
Active area inner radius (mm)	140	534
Active area outer radius (mm)	392	1091
Pad size (mm)	2.74×2.74	7.62×7.62
Total active area (m^2)	0.42	2.84
Number of pads readout	53800	48400
Number of modules	210	400
Pads per module	8×32	11×11
Total readout time (μs)	280	1600
Calibration (electrons/count)	2700	2300

Table 2.2: Parameters of UV detectors and pad readout.

A summary of the pad readout parameters is given in Table 2.2. For further details see [52].

2.2.3 Silicon Pad Detector and Silicon Drift Chamber

CERES uses two additional detectors, a Silicon radial drift chamber (SiDC) and a Silicon pad detector (SiPD) located close to the target at $z = 74$ and 91mm respectively. The target area arrangement is shown in Figure 2.4. The Silicon pad detector (SiPD) is used as a fast first level multiplicity trigger. It covers the pseudorapidity interval $1.7 < \eta < 3.7$. The SiPD has 64 elements arranged in 8 concentric rings of 8 azimuthal sectors each. The rings cover equal pseudo rapidity intervals of $\Delta\eta = 0.25$. The pad information is read digitally, i.e. number of firing pads, but analog information reading is also possible and is used for high multiplicity collisions of heavy-ions. A typical Si-pad event display is shown in Figure 2.3. For further information about the SiPD see reference [53]. The Silicon drift Chamber (SiDC) is used for vertex reconstruction using hits in the SiDC and their correlated Cherenkov ring centers in RICH-1. The SiDC can also be used to discriminate between single and double hits (a conversion pair) using its dE/dx information. The SiDC plays an essential role in the high multiplicity events of nucleus-nucleus collisions. Its benefit, however, is marginal in p-Be and p-Au collisions. For that reason, and also because the detector used in 1993 run suffered from low efficiency, [54], the SiDC information was not used in this work. For further reading about the SiDC see reference [55]. The Silicon pad detector and the silicon drift chamber, mounted in the target area of the CERES experiment, are shown in

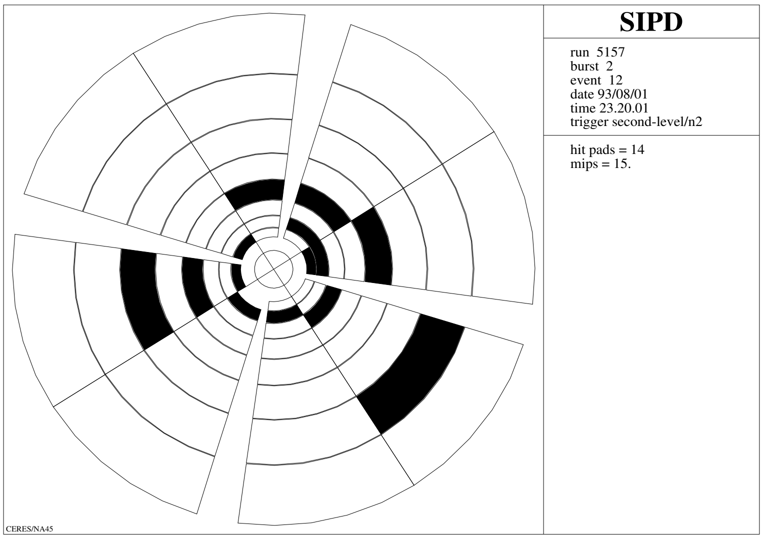

Figure 2.3: A typical event in the 64 pad Silicon detector where each black cell denotes a hit.

Figure 2.4.

2.2.4 TAPS calorimeter

The 1993 set-up included also the electromagnetic calorimeter of the TAPS collaboration. In its original design the TAPS calorimeter consisted of a Two-Arm-Photon-Spectrometer [57] which was reconfigured into an annular shape, and was mounted downstream of CERES ($3.1 \leq \eta \leq 4.0$). The calorimeter consists of 384 BaF_2-detectors each one with an hexagonal shape, 5.9 cm diameter, and 12 radiation lengths. The detector arrangement and a typical TAPS event, in the 1993 setup, is shown in Figure 2.5

2.3 The CERES Trigger Scheme

Since the signal we are looking for is so rare, taking untriggered data is not practical; one would have to record a huge amount of events with a tiny fraction of them containing an electron pair. Therefore, in order to enrich the data sample, a trigger is essential in particular in the p run. For that, CERES has developed an intelligent

z (cm)	**Component**	**Material**	**X** (cm)	**X_0** (cm)	**X/X_0** (%)
0	Segmented target	Au	$29 \times 50 \cdot 10^{-4}$	0.334	1.1(1)
	Target support foils (50%)	mylar	$29 \times 6 \cdot 10^{-4}$	28.7	0.03
	or 1 piece target	Be	3	35.3	0.85
7.4	Si drift detector	Si	$280 \cdot 10^{-4}$	9.36	0.30
	Si drift det. protection foils	mylar	$2 \times 30 \cdot 10^{-4}$	28.7	0.02
	Si drift det. ceramics bars				0.20(1)
9.1	Si pad detector	Si	$300 \cdot 10^{-4}$	9.36	0.32
	Si pad det. protection foils	mylar	$160 \cdot 10^{-4}$	28.7	0.06
10	Target zone	air	10	30420	0.03
10	Radiator 1 entrance window	mylar	$2 \times 50 \cdot 10^{-4}$	28.7	0.03
88	Radiator 1 gas (50%)	CH_4 at 50^0	88	79102	0.06
	Total				
	with Au target				2.15
	with Be target				1.87
100	Mirror 1	Carbon	0.11	26.7	0.41
102	Magnetic field zone	He	48	$48 \cdot 10^4$	0.01
150	Radiator 2 entrance window	mylar	$2 \times 80 \cdot 10^{-4}$	28.7	0.06
325	Radiator 2 gas (50%)	CH_4 at 50^0	175	78102	0.22
	Total				
	with Au target				2.85
	with Be target				2.57

Table 2.3: List of materials and the corresponding radiation lengths in the CERES spectrometer used in 1993.

1) The effective target radiation length is given by half the thickness of one disk plus some small contribution from other disks. The number quoted includes this effect which has been determined from a Monte Carlo simulation [56].

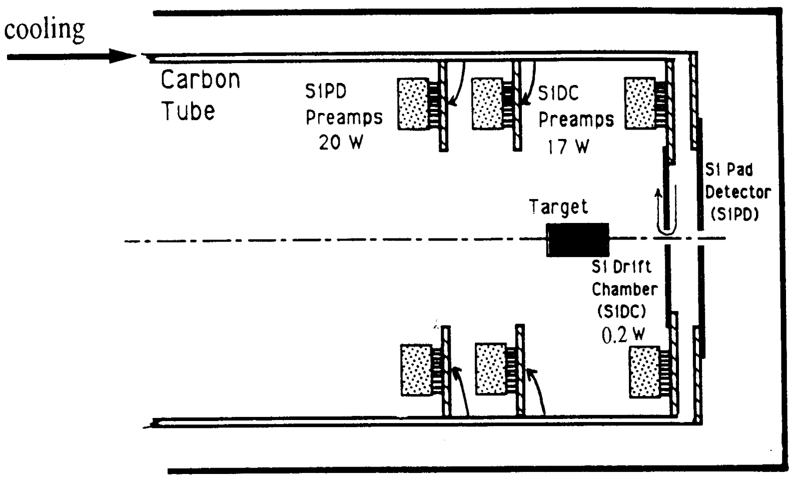

Figure 2.4: The Silicon pad detector and the silicon drift chamber in the target area of the CERES experiment.

trigger which is able to recognize rings in RICH-1 by performing a relatively fast pattern recognition. In the 1993 data taking CERES used a 3-level trigger scheme. The first level trigger is on the charged particle multiplicity in the Silicon pad detector. The other two triggers do a fast ring pattern recognition in RICH-1. In the next three sub-sections each of the triggers is discussed.

2.3.1 First Level Trigger

The first level trigger (FLT) is based on the SiPD detector. The first level trigger is practically a minimum bias interaction trigger providing a fast decision, within 0.2μs. A minimum bias interaction is defined by requiring a minimum number of charged particles in the SiPD within the CERES acceptance. Since the particle multiplicity is low in the p induced reactions every hit pad is counted as one charged particle. The specific FLT conditions that were used in the p run of 1993 are given in Section 3.1.2.

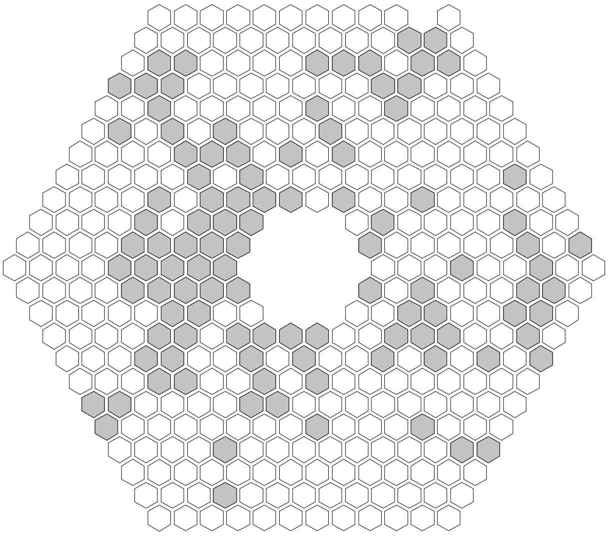

Figure 2.5: TAPS detector arrangement and typical event in the 1993 run. The dark cells are detectors which absorbed energy.

2.3.2 Intermediate Level Trigger (ILT)

The ILT triggers in a relatively short time on at least two ring candidates in RICH-1 by doing a coarse pattern recognition. The ILT was specifically developed for the 1993 run where it was inserted between the FLT and the SLT. The ILT in principle, does the same as the SLT (see next sub-section) but on a 16 times coarser grid: One ILT pixel contains the analog sum information of 16 pads (every second pad in x and y) from an array of 8×8 original pads. The summation is performed in two steps. First, 4 pads in a row of 8 pads which we call a strip are summed. Four of these strips, representing one ILT pixel, are then summed up and passed to a processor whenever their sum exceeds a chosen threshold. After the readout of all the strips the ILT processor itself is started. The processor first performs a cluster removal and then a simple pattern recognition: a minimum number of set pixels within an annular mask $R \pm \Delta R$ (where R is the saturated ring radius and $\Delta R = 0.25R$), is considered as a ring candidate. A trigger is generated whenever the number of candidates ≥ 2, otherwise the readout sequence is aborted. The operation of the ILT is illustrated in the sequence of Figures 2.6 to 2.9. Figure 2.6 shows a raw event in RICH-1 displaying two clear rings. Figures 2.7 and 2.8 display the strip and pixel pattern generated by the coarse sum analog and Figure

2.9 shows all the candidates found by the ILT (represented by the square boxes). Clearly the two rings have been found. The total decision time of the ILT is 35μs.

2.3.3 Second Level Trigger (SLT)

The SLT task is to perform a fast recognition of at least two isolated rings. The SLT goes through the following steps:

- Cleanup - big clusters of pads (produced by the passage of a charged particle through the detector) are removed since they confuse the pattern recognition.

- A search for rings in the whole UV-1 area - This is done by performing a point to ring Hough transformation [58], namely, for each pad in the UV-1 detector a ring with the nominal asymptotic radius is assigned. The transformed image exhibits therefore an intensity distribution with a pronounced maximum at the location of the ring center. The principle of the technique is illustrated in Figure 2.10.

- A ring candidate is identified as a peak in the Hough array. The maxima are searched above some lower threshold (in order to reject pion rings which have smaller radius and therefore weaker contribution to the amplitude or other background) and below an upper threshold which rejects very close pairs (γ conversions).

- Finally, the algorithm requires at least two ring candidates separated by a minimum distance, in order to reject the close rings from the abundant π^0 Dalitz decays.

The SLT uses $1/4$ of the UV-1 pad information (every second pad in x and y) for the ring pattern recognition. The hardware is based on an array of 160×160 processors with a capacity of full parallel processing at a rate of $\sim 6 \times 10^{11}$ operations/sec. The SLT decision is available within 140μs.

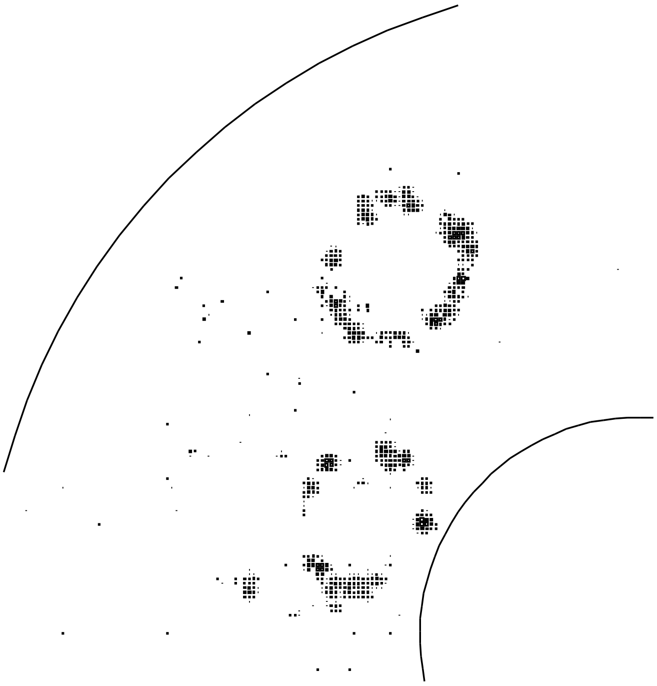

Figure 2.6: A raw event.

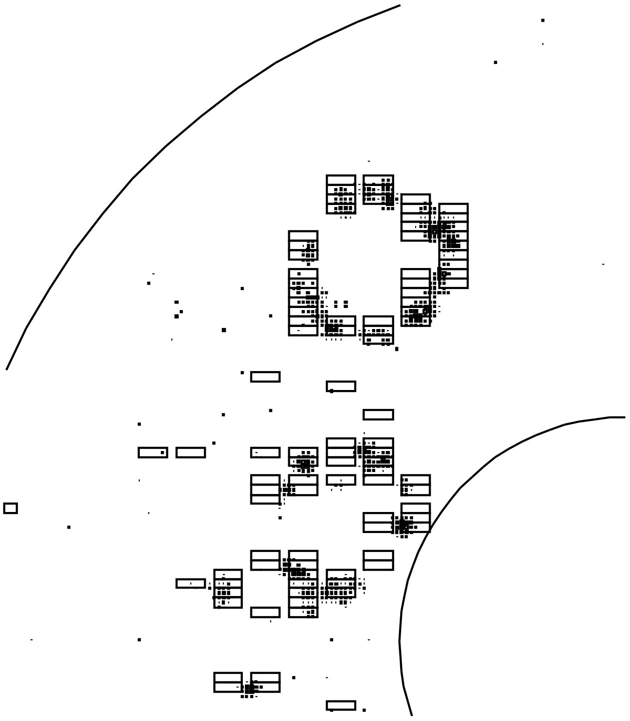

Figure 2.7: ILT strips.

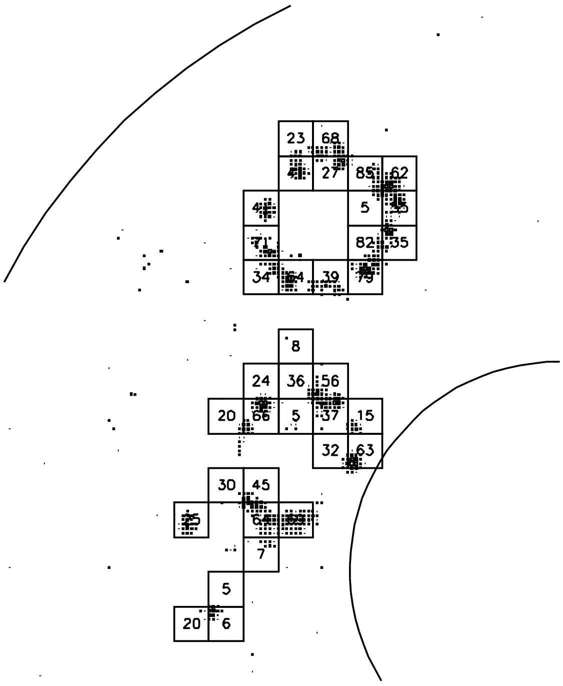

Figure 2.8: ILT pixels of the same event.

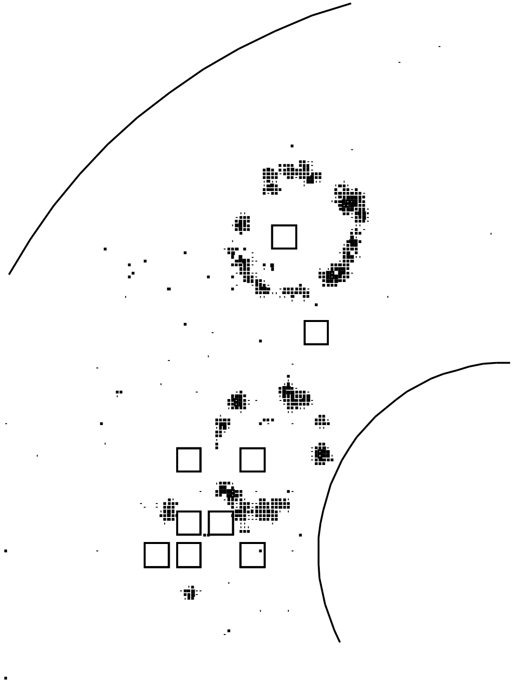

Figure 2.9: ILT decision array.

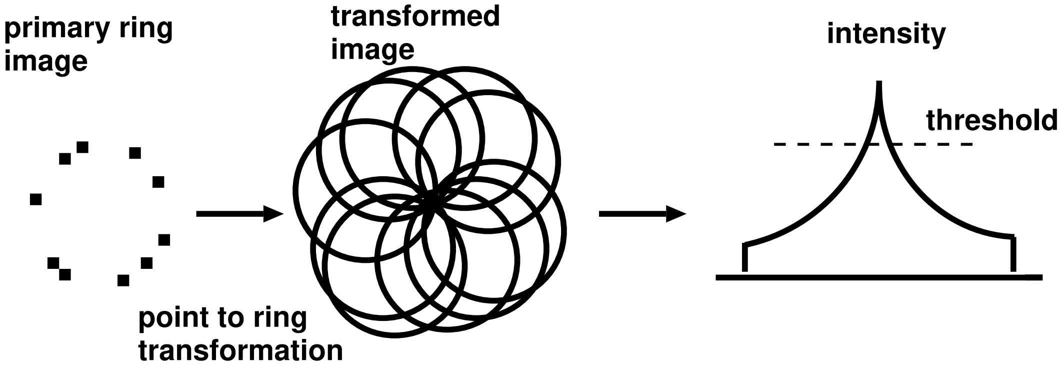

Figure 2.10: Ring candidate search by a Hough transformation.

2.4 Spectrometer Performance in the 1993 p Run

2.4.1 Gain of UV detectors

The gain of the detector is an important parameter in the performance of the spectrometer. It determines the fraction of converted photons which are actually detected and also the total ring amplitude, a quantity which is important for recognizing conversion pairs. However, the gain is not constant and it varies in two ways, as a function of time and as a function of the location on the detector. The time dependent gain variations arise from changes in the atmospheric pressure, temperature and the voltage settings in the various amplification stages. The gain variation as a function of time is shown in Figure 2.11, and the gain distribution, which is the projection of Figure 2.11 on the gain axis, is shown in Figure 2.12, yielding a global average gain of $(4.1 \pm 0.5) \times 10^5$ ($(3.7 \pm 0.5) \times 10^5$) electrons in UV-1 (UV-2).

The spatial gain inhomogeneity arises from the differences in the gaps between the detector stages due to the mechanical tolerances, distortions caused by the strong electric field and variations in the electronic gain of the readout modules. These variations are easily corrected on a pad by pad basis. The total pad amplitude correction is done by assuming that the temporal and the spatial fluctuations are independent, therefore, for each pad i:

$$A_i^{\text{corrected}} = C_T \cdot C_S^i \cdot A_i$$

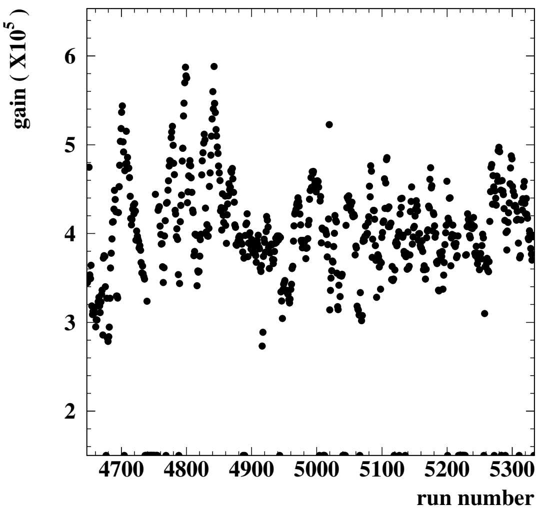

Figure 2.11: UV-1 gain variations as a function of time, represented by the run number.

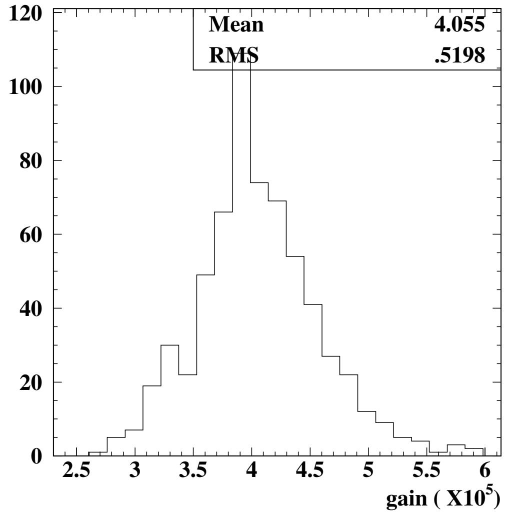

Figure 2.12: UV-1 gain distribution (each entry is from a single run), $\bar{g} = (4.1 \pm 0.5) \times 10^5$.

where C_T is the temporal and C_S is the spatial correction factors:

$$C_T = \frac{<\text{ global average gain over all runs }>}{<\text{ average gain of given run }>}$$

The spatial correction factor (calculated only from a single run or from a few runs where the temporal changes can be neglected) is given by:

$$C_S^i = \frac{<\text{ average amplitude from all pads }>}{<\text{ average amplitude of pad i }>}$$

2.4.2 Number of Photons per Ring

The number of photon hits per ring, N, is of crucial importance for recognizing a ring in the presence of background hits. The measured number of hits/ring is extracted from a sample of π^0 Dalitz pairs[3] and is shown in Fig. 2.13. Since the

---

[3] A π^0 Dalitz pair has a distinctive pattern consisting of two close rings in RICH-1 matched to two rings in RICH-2. To reduce the probability of fake tracks, when the number of hits per ring in RICH-1 was studied we required $N \geq 8$ on the number of hits per ring in RICH-2 and vice versa when studying the number of hits per ring in RICH-2.

Cherenkov photon emission process follows the Poisson statistics a fit was included in the figure. For a radiator of length L the average of the Poisson distribution is

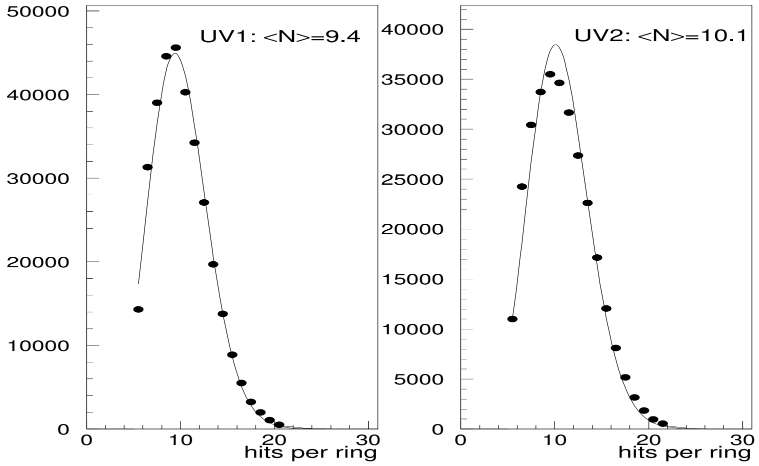

Figure 2.13: Hits per ring in RICH-1 (left) and in RICH-2 (right). The continuous line is a Poisson fit which gives an average of 9.4(10.1) hits in RICH-1 (RICH-2).

expected to be [59]:

$$N = N_0 \cdot L/{\gamma_{th}}^2 \tag{2.1}$$

where γ_{th} is the Lorentz factor for the threshold speed of the charged particle which produces the Cherenkov photons in the radiator gas. N_0 is the figure of merit of the RICH detector. It is obtained by folding the quantum efficiency of the TMAE over the band width of the RICH; RICH-1 (RICH-2) is sensitive to photons in the range $6.1 - 8.5$eV ($6.1 - 7.4$eV). These boundaries are determined by the ionization threshold of the TMAE and the window transmission cut-off, the different upper values in both detectors reflecting the different window materials, a CaF_2 for RICH-1 and quartz for RICH-2, giving a final number of photons per ring similar to that in UV-2. The value obtained for the theoretical N_0 is 276cm^{-1} (134cm^{-1}) for RICH-1 (RICH-2). There are several mechanisms that degrade the theoretical value of N_0 which are: imperfect radiator transparency and mirror reflectivity, hit losses due to spokes in the window support, efficiency of the conversion gap and the transparency of the first anode grid of the UV chambers and finally, additional losses are due to the zero suppression applied on the pad signal which discards low amplitude hits. These losses are quoted in Table 2.4 and amount to $\epsilon_{\rm RICH} = 0.57$ (0.56) in RICH-1 (RICH-2). Therefore the effective value of N_0 is 157cm^{-1} (75cm^{-1}) in RICH-1 (RICH-2). The expected value of the average number of photon hits per ring, calculated using Equation 2.1 is 14.3 (12.3) UV-1 (UV-2). The number of resolved hits per ring, N_{res}, is somewhat smaller due to pile-up losses, when the distance between two hits is smaller than the double-hit resolution distance, $\sigma_{dhr} = 2.5(2.0)$ pads in UV-1 (UV-2). The pile-up probability for a ring with $< N >$ hits and radius R is:

$$p = 1 - \exp(-\frac{< N > \sigma_{dhr}}{2\pi R})$$

The expected number of resolved hits is therefore 9.7 (9.7) in RICH-1 (RICH-2). This number can be compared with the measured number of 9.4 (10.1) hits per ring, see Figure 2.13. As a cross check the number of hits before pile-up can be measured experimentally by dividing the total ring amplitude (sum analog) by the single hit amplitude. The ring amplitude is equal to 2445 (2270) counts in UV-1 (UV-2) and the average hit amplitude is 175 (185) counts, Therefore, the number of hits before pile-up is $N = 14.0$ (12.3), in good agreement with the theoretical prediction. The Cherenkov photon yield is summarized in Table 2.4.

2.4.3 Single-Hit Resolution

The single-hit resolution (s.h.r) is an important quantity in determining the momentum and mass resolution of the spectrometer, see next section. The s.h.r. is the r.m.s dispersion of photon hits along the radial direction in a Cherenkov ring. The hit dispersion is due to the multiple-scattering in the radiator and other momentum independent processes: the chromatic-aberration, the mirror quality, the single-electron diffusion in the conversion region and the readout accuracy; the chromatic-aberration is the dominant one, see Table 2.5. The expected s.h.r, based on the values specified in Table 2.5, at high momentum where multiple-scattering is negligible, is 1.23 (0.69) mrad in UV-1 (UV-2).

In Figure 2.14 the measured single-hit resolution, obtained from a sample of π^0 Dalitz pairs with electron momentum $p > 1$GeV/c is shown. The peaks in the plots of Figure 2.14 correspond to the Cherenkov ring saturation radius, in mrad. The widths are the s.h.r.: $\sigma_{\rm s.h.r} = 1.39$ (0.89) mrad in UV-1 (UV-2) very close to the expected ones.

	RICH-1	**RICH-2**
$\mathbf{N_0}^{\textbf{theoretical}}$ textbf(cm)$^{-1}$	**276**	**134**
mirror reflectivity	0.85	0.85
radiator transparency	0.98	0.96
window transparency	0.93	0.93
first grid transparency	0.89	0.89
photo-absorption	0.90	0.90
signal threshold	0.92	0.92
total losses	0.57	0.56
$\mathbf{N_0}^{\textbf{eff}}$ **(cm)**$^{-1}$	**157**	**75**
γ_{th}	31.4	32.6
radiator length L_{eff} (cm)	90	175
N expected	**14.3**	**12.3**
N observed (summed amplitude)	**14.0**	**12.3**
double hit resolution (pads)	2.5	2.0
Cherenkov ring radius (pads)	14.56	16.39
N expected after pile-up	**9.7**	**9.7**
N observed (resolved hits)	**9.4**	**10.1**

Table 2.4: Number of Cherenkov photons per ring.

2.4.4 Momentum and Mass resolution

The momentum resolution is determined by the quality of the track match, σ_θ, assuming that the radial and azimuthal resolutions are identical. σ_θ depends on the ring center resolution, σ_r, of the RICH detectors, which itself depends on the single-hit resolution, $\sigma_{\mathrm{s.h.r.}}$:

$$\sigma_r = \frac{\pi\sigma_{\mathrm{s.h.r.}}}{2\sqrt{N-2}} \tag{2.2}$$

where N is the number of photon hits on the ring. Equation 2.2 is exact for infinite momentum. σ_θ depends also on the momentum via the multiple-scattering in the material between RICH-1 and RICH-2 ($X/X_0 = 0.7\%$) which is dominant at low momentum. The multiple-scattering contribution is given by [60]:

$$\sigma_{M.S.} = \frac{13.6\mathrm{MeV}}{\beta c p} z \sqrt{\frac{X}{X_0}} (1 + 0.038 \ln \frac{X}{X_0}) \tag{2.3}$$

therefore, the multiple-scattering contribution is about $0.92/p$ [mrad/(GeV/c)].

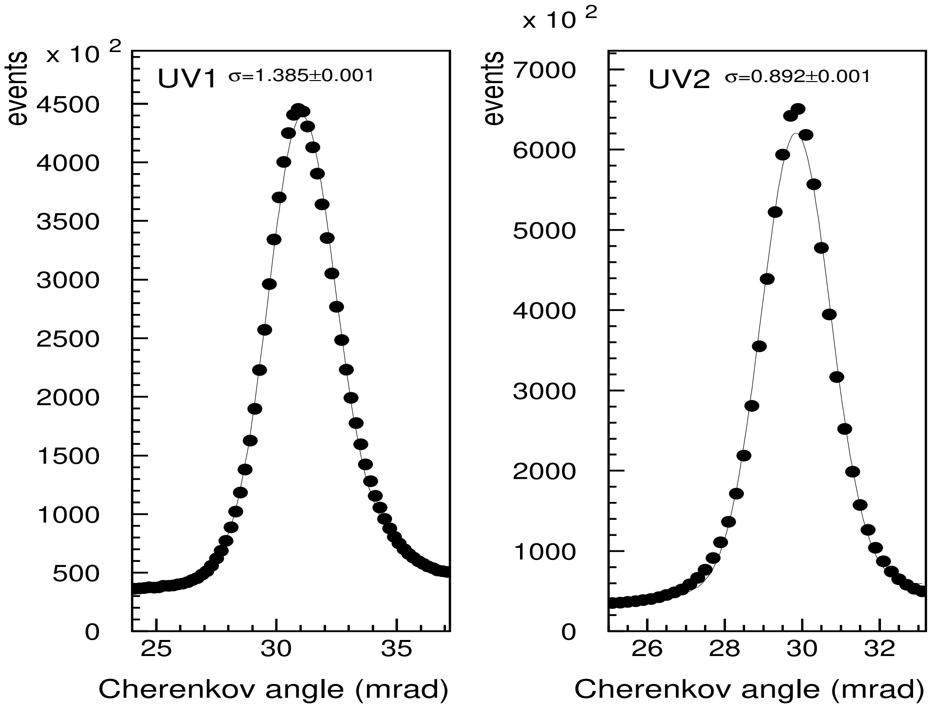

Figure 2.14: Single-Hit Resolution, RICH-1 (left) and RICH-2 (right). The continuous line is a fit of a Gaussian and a linear background which gives a s.h.r of $\sigma = 1.39(0.89)$ mrad in RICH-1 (RICH-2).

The complete expression for the expected track match, σ_θ, is finally given by:

$$\sigma_\theta(p) = \sqrt{\sigma^2_{M.S.} + \sigma^2_{r1} + \sigma^2_{r2}} \tag{2.4}$$

A plot of the track match as a function of the momentum p is given in Figure 2.15. where the measured data points were fitted by:

$$\sigma_\theta(p) = \sqrt{(c_1/p)^2 + c_2^2} \tag{2.5}$$

with $c_1 = 1.1$mrad·GeV/c and $c_2 = 1.30$mrad. c_1/p represents the multiple-scattering contribution and is close to the expected value, while c_2 reflects the track match contribution at infinite momentum and is larger by nearly 40% from the expected track match based on the measured s.h.r. using Equations 2.2 and 2.4 which

(r.m.s in mrad)

	RICH-1	**RICH-2**
chromatic aberration in CH_4	1.13	0.53
readout accuracy	0.33	0.24
single electron diffusion	0.37	0.10
mirror quality	< 0.10	0.35
total	1.23	0.69
measured value	1.39	0.89

Table 2.5: Contributions to the single-hit resolution.

is equal to 0.94mrad. This discrepancy is not yet understood. A possible explanation for it is inter-calibration problems between the RICHes.

The electron momentum is measured by its azimuthal deflection, $\Delta\phi$, in the magnetic field between RICH-1 and RICH-2:

$$\Delta\phi = (120\mathrm{mrad} \cdot \mathrm{GeV/c})/p \tag{2.6}$$

The momentum resolution is therefore:

$$\frac{\sigma_p}{p} = \frac{\sigma_{\Delta\phi}}{\Delta\phi} = \frac{\sigma_{\Delta\phi} \cdot p}{120} \tag{2.7}$$

where p is in GeV/c and ϕ is in mrad. $\sigma_{\Delta\phi}$ is given by:

$$\sigma_{\Delta\phi} = \sigma_\theta/\theta \tag{2.8}$$

that is σ_ϕ is larger for smaller polar angles. At the high momentum limit, Equation 2.7 becomes:

$$\frac{\sigma_p}{p} = \frac{\sigma_\theta}{\theta}\frac{p}{120} \tag{2.9}$$

For an average polar angle of 11^0 and the measured ring center resolution of 1.3mrad, the momentum resolution at 1GeV/c is about 5.6%.

The mass resolution is obtained from the momentum resolution. It is estimated, using the event generator (see Chapter 4) by a convolution of the electron momentum with the momentum resolution and then constructing the electron pair mass using Equation 3.2. The mass resolution as a function of the mass is shown in Figure 2.16 and is about 10% at the ρ^0/ω-peak.

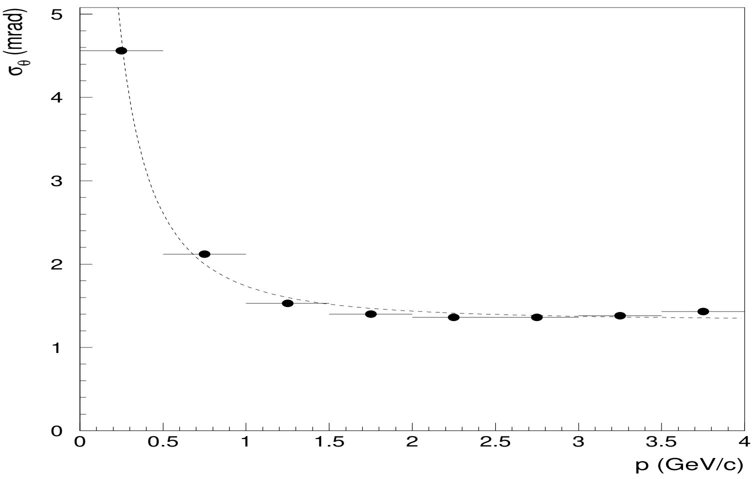

Figure 2.15: Track match, σ_θ, vs. momentum.

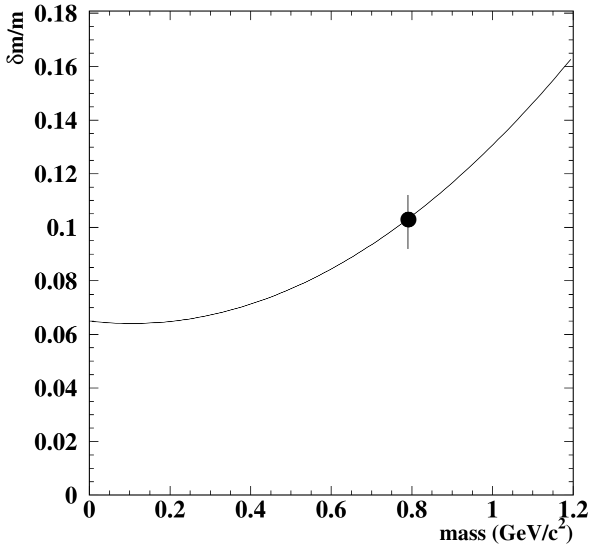

Figure 2.16: Relative mass resolution vs. mass, obtained from the momentum resolution. The data point refers to the experimental mass resolution extracted from the 1993 p run at the ρ^0/ω peak.

Chapter 3

The 1993 p Run and the Analysis Procedure

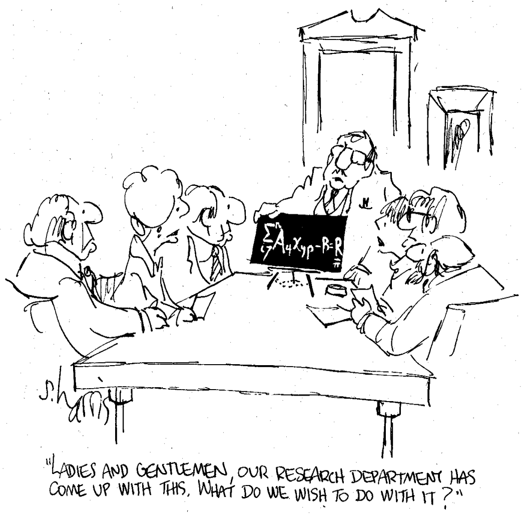

Figure 3.1: From Physics Today, August 1990.

This chapter deals with the 1993 proton running conditions, the beam, target and trigger. The off-line analysis program and its basic steps up to the extraction of the signal are then described.

3.1 The 1993 running conditions

3.1.1 Beam and target

The SPS delivered to the CERES spectrometer a 450GeV/c proton beam with an average intensity of 4×10^6 protons per burst. The SPS cycle had a duration of 14.4sec which included 4.4sec for the burst itself.

Specification of the targets that were used are summarized in Table 3.1. The Be target consisted of a 3cm long wire of 1.2mm diameter. The gold target was segmented and consisted of 29 disks of 50μm thickness and 600μm diameter mounted on 6μm mylar foils separated by 1.6mm. The design of the segmented target represents a compromise between two contradictory needs: on one hand the target should be thick in order to achieve a high interaction rate and therefore to collect sufficient statistics. On the other hand in order to minimize γ conversions and double interactions, the target should be thin. Using a segmented target with appropriate gaps between the disks achieves both goals.

	Be	**Au**
Type	one piece	segmented
Number of disks	1	29
Thickness/disk	30mm	50μm
Diameter (mm)	1.2	0.6
$\lambda/\lambda_I(\%)$	7.4	2.3
X/X_0 (%)	0.8	1.1

Table 3.1: Target specifications.

3.1.2 Trigger conditions

The FLT trigger is provided by the SiPD detector. In the 1993 p run a digital reading of the SiPD detector was used, this mean that each hit in the SiPD is counted as 1 charged particle regardless of any possibility of pile-up of particles. The FLT requirement was $n_{ch} \geq 2$, that is at least two charged particle hits in 4 rings of the SiPD covering the pseudo rapidity $1.95 < \eta < 2.95$, i.e. bracketing the CERES acceptance. This data taking mode is called “un-triggered data” as opposed to “triggered” data taking mode using the ILT+SLT where at least 4 (6) charged particles in the SiPD detector were required in the p-Be (p-Au) run respectively. This means that in an event with 2 electrons the actual multiplicity is $n_{ch} - 2$ (in fact, on the average it is somewhat less because of pile up hits. see Section 5.3.).

3.1.3 Trigger enrichment and performance

The trigger duty is to enrich the data sample with the desired type of events. The trigger enrichment is the product 3 factors: the FLT bias, the ILT+SLT rejection factor (the trigger ability to reject undesired events) and the ILT+SLT efficiency (the fraction of desired events that are kept by the trigger).

$$\boxed{\text{TRIGGER ENRICHMENT =BIAS} \times \text{REJECTION} \times \text{EFFICIENCY}}$$

If we denote by S_i (S_o) the input (output) signal and by N_i (N_o) the incoming (outgoing) events then,

trigger efficiency = S_o/S_i
trigger rejection = N_i/N_o

The FLT introduces a bias since for the events with an e^+e^- pair the effective trigger is $n_{ch} \geq 2$. The FLT bias is therefore defined as the ratio of interactions with $n_{ch} \geq 2$ and with $n_{ch} \geq 4$. This ratio was periodically monitored on-line during the whole experiment, where each measurement was determined from an average over several bursts, yielding an average value of 2.42 ± 0.25 in p-Be (see Figure 3.2) and 1.42 ± 0.07 in p-Au. The ILT and SLT combined rejection factor was also periodically monitored on-line, yielding an average of 122 ± 16 (106 ± 11) in p-Be (p-Au). The ILT rejection factor and the combined ILT+SLT rejection factor are shown in Figure 3.3. The ILT and SLT together have an efficiency of 0.55 ± 0.05 both in p-Be and p-Au; this value is obtained using a trigger emulator software that is fed with Monte-Carlo events: Electron pairs are generated using an event generator (see next chapter) which then, using a spectrometer simulation program, produce MC rings; this program is explained in Section 5.2 in the context of determining the pair reconstruction efficiency which is done in a similar way. The MC rings are overlayed on real un-triggered data, in order to simulate the right background. The trigger efficiency is then defined as the ratio between the number of events which passed the trigger emulator to the number of generated events. The overall trigger enrichment factor obtained is 162 ± 31 (83 ± 12) for the p-Be (p-Au).

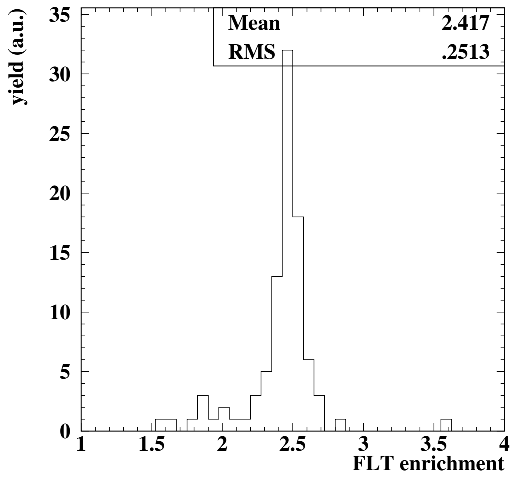

Figure 3.2: The FLT bias in p-Be.

3.2 Sample size

3.2.1 The p-Be run

The SLT p-Be run took place during 41 days in July-August 1993. 644 runs were analyzed, with about $17,000$ events/run. In the whole p-Be sample there were nearly $130,000$ SPS bursts, with an average of 190 bursts/run, that is about 90 events/burst. Of these events $\sim 10.3 \times 10^6$ were valid events in terms of a right trigger pattern and right event labels. This is therefore the analyzed p-Be sample size. The number of minimum biased events obtained by multiplying the sample size by the trigger enrichment is $\sim 1.67 \times 10^9$ events. The p-Be sample size is summarized in Table 3.2. Assuming $1.7 \cdot 10^9$ minimum bias events times pair reconstruction efficiency of about 0.53 (see Chapter 5) times the expected e^+e^- yield, for $m > 200$MeV/c^2 of $\sim 1 \cdot 10^{-5}$ per event there should be about 9000 pairs in the p-Be data sample. The p-Be data taking included also about 1.8×10^6 events in untriggered mode (FLT data). These events were examined but were not included in this analysis since their contribution to the final e^+e^- pair sample is negligible.

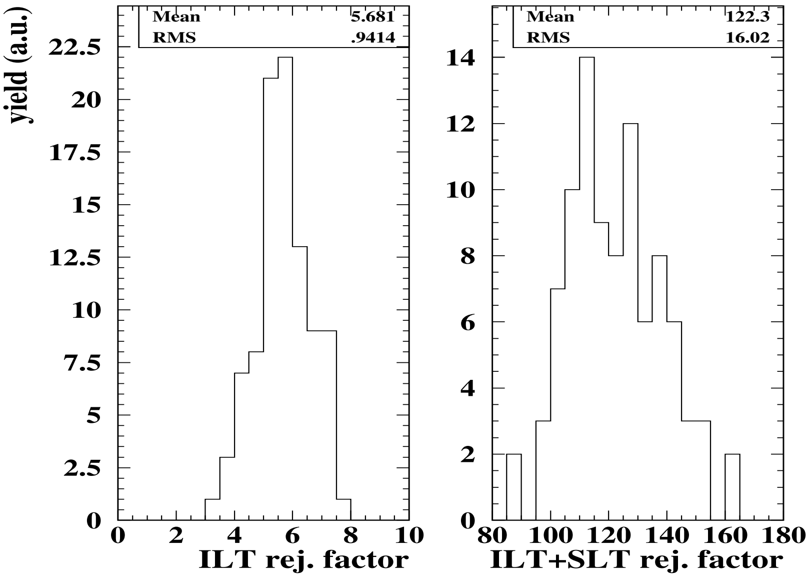

Figure 3.3: ILT (left) and the combined ILT+SLT (right) rejection factors.

3.2.2 The p-Au run

The SLT p-Au run took place in August 1993 during 9 days. A total of 163 runs were analyzed, where in each run there were also about 17,000 events. In the p-Au sample there were nearly 40,000 SPS bursts with on the average 240 bursts per run, that is about 70 events/burst. The analyzed p-Au sample contains $\sim 2.56 \times 10^6$ events. The number of minimum bias events obtained by multiplying the sample number by the trigger enrichment is $\sim 2.2 \times 10^8$ events. The p-Au sample size is summarized in Table 3.2.

reaction	sample size	FLT bias	ILT+SLT		overall enrichment	min. bias events
			rejection	efficiency		
p+Be	10.3×10^6	2.4	122	0.55	162	1.67×10^9
p+Be	1.8×10^6	2.4	untriggered data		2.4	4.3×10^6
p+Au	2.6×10^6	1.4	106	0.55	83	2.16×10^8

Table 3.2: p-Be and p-Au sample size.

3.3 Data analysis procedure

The event analysis software performs two basic tasks. The first one is the event pattern recognition, i.e. the identification of at least 2 tracks with a minimum p_T. The main steps here are as follows:

- Event clean-up.
- Find UV-photon hits.
- Find ring candidates.
- Fit electron rings and get the exact ring coordinates.
- Find electron tracks.

The second task deals with the extraction of the signal, i.e. the invariant mass spectrum of the e^+e^- pairs.
The main steps here are as follows:

- Identify electron pairs from the trivial sources: π^0 Dalitz decay and γ conversions.
- Rejection of single tracks originating from trivial sources.
- The surviving tracks are combined into pairs of unlike sign (+-) and like sign (++,- -).
- The desired signal is obtained by subtracting the like sign pairs from the unlike sign pairs.

These steps are discussed in detail below:

3.3.1 Event clean-up

Most of the p-Be and p-Au events in the UV detectors are empty. They have a low background and a very low probability to contain rings. Those are effectively rejected by the trigger system. A typical SLT event with two clearly visible rings is shown in Figure 3.4. One can see there in addition to the rings and isolated UV-photon hits also electronic noise and occasionally a large track or a big cluster of pads created by the passage of a charged particle through the detector. These must be removed at the beginning of the analysis, in order to lower the background and minimize the number of fake rings. An event clean-up procedure is therefore performed. The most important cleanup elements are: the removal of isolated 1 and 2 pads clusters which are mainly due to pedestals fluctuations (a typical UV photon hit has on the average about 6 pads), removal of line of pads and removal of large-saturated ionization tracks. The same event as in Figure 3.4 is shown once more in Figure 3.5 after the cleanup.

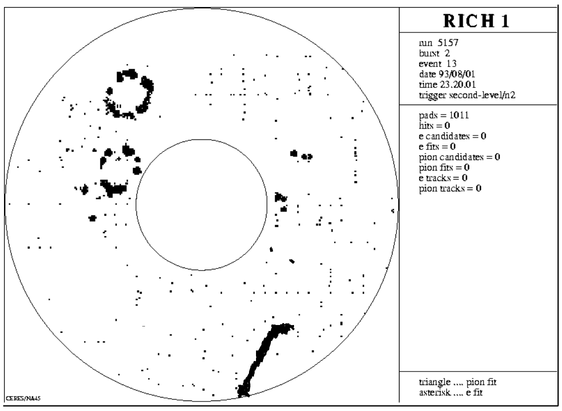

Figure 3.4: A typical raw event, before clean-up, in RICH-1.

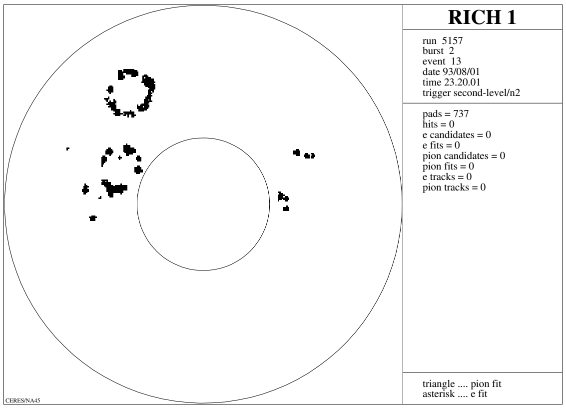

Figure 3.5: The same event after cleanup.

3.3.2 Hits detection

A hit is a cluster of detected active pads that corresponds to a single UV-photon. Typical hits on a ring are shown in Figure 3.6. An ideal hit looks like a mountain with a peak at the middle and the total hit amplitude has an exponential distribution characteristic of the amplification of a single electron primary charge in the UV detector. The hits are determined from the clusters of pads that survived the cleanup. If a cluster contains more than one clear and isolated maxima, it is assumed that it is built from pile up of hits, then the cluster is splitted into several sub-clusters. The final hit position is computed as the center of gravity of all the pads in the cluster or the sub-cluster.

3.3.3 Ring candidates

Although events which passed the trigger system should contain in principle at least two ring candidates, it should be remembered that the trigger system searches

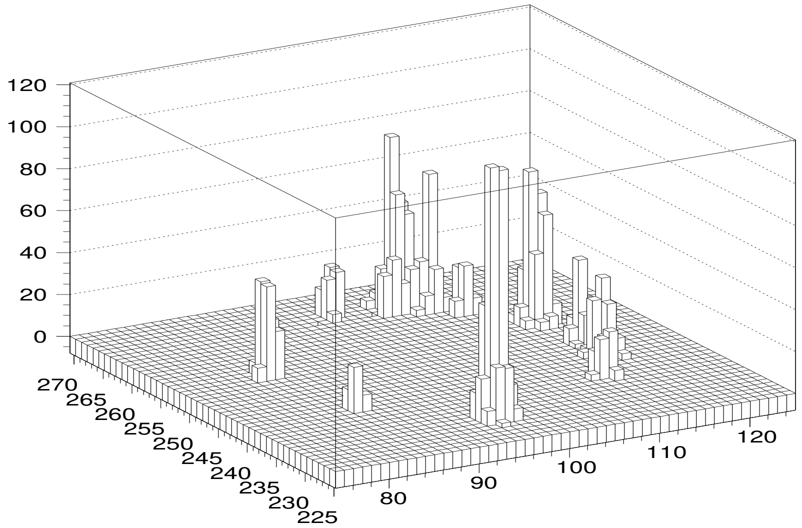

Figure 3.6: Typical pattern of photon hits on a ring.

for rings on a course grid and therefore it can get into a wrong decision. In addition, even if a ring exists there is no a priori knowledge where the ring center is located. Therefore, the point to ring Hough transformation for rings search in the whole detector area is done once more, as in the SLT, this time, software wise and on the fine scale of the detector pads and for both detectors. The algorithm was already explained in section 2.3.3. The advantage of the Hough transformation is its relative high speed compared to other methods, for example, recognizing rings by performing a convolution between the event image and a ring mask, using FFTs. Other methods for recognizing Cherenkov rings in a given pattern using Neural-Networks are mentioned in [61] for back-propagation methods, and in [62] using non-adaptable networks which are best solved on massively parallel architectures. The candidate search is performed first in RICH-2 and a minimum of 2 candidates is required to proceed with the event analysis.

3.3.4 Finding the exact rings centers

The exact ring position is finally determined using a minimization procedure starting with the ring candidate position and all the N hits in a box of $\pm 1.5R$ around the candidate position, where R is the a priory known ring radius. The potential function being minimized, using MINUIT [63], is:

$$F = \frac{1}{N-1}\sum_{i=1}^{N} 1 - \exp(-\frac{(r_i - R)^2}{2\sigma^2}) \tag{3.1}$$

where σ is the potential width, see ref. [64] for further details. In Figure 3.7 an exact ring center, marked by an asterisk, was found close to one of the candidate ring centers, marked by a cross. Another method for circle fitting can be found in [65].

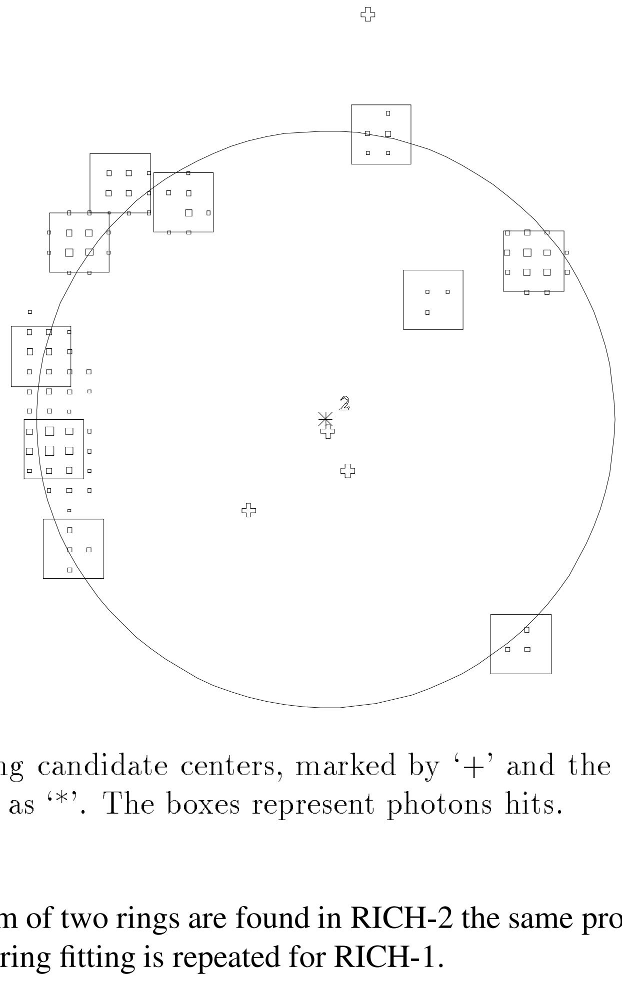

Figure 3.7: Ring candidate centers, marked by '+' and the final exact ring center, marked as '*'. The boxes represent photons hits.

If a minimum of two rings are found in RICH-2 the same procedure of candidate search and ring fitting is repeated for RICH-1.

High momentum charged pions can produce Cherenkov rings, see Appendix B. The pion ring radius, which depends on its momentum, is smaller than the electron radius and is recognized by a fitting procedure which does not constrain the ring radius to the saturated value as for the electron but allowing it to vary.

3.3.5 Tracks reconstruction

The next step in the analysis is to correlate rings from the first RICH with rings in the second RICH, i.e. to form the electrons tracks. A track is defined by its momentum, p and its θ and ϕ angles in RICH-1 (before the magnetic field). With this knowledge in hand one can build the electron four-vector, $p^{(4)}$. After passing RICH-1 the electron is deflected by the magnetic field in the azimuthal direction, clockwise or counter-clockwise according to its charge, whereas the polar angle is kept unchanged (besides a small deflection due to the focusing effect of the magnetic field). The deflection is inversely proportional to the particle momentum, see Equation 2.6. In correlating the electron ring in RICH-2 to its ring in RICH-1, a transverse momentum cut of $\mathrm{p}_T > 50$MeV/c is applied, thus limiting the region of search of the electron location in RICH-2 in the azimuthal direction. The actual region were the associated ring in RICH-2 is searched, has a 'butterfly' shape when looking in polar coordinates, see Figure 3.8, where the azimuthal deflection, $\Delta\phi$, is in the abscissa and the radial shift, $\Delta\theta$, is in the ordinate. In the radial direction the region is limited by the ring center resolution at the infinite momentum limit (see Section 2.4.3). As the momentum decreases, the searched area increases due to the multiple-scattering, producing the 'butterfly' shape. The shape is not symmetric in the θ direction because of the focusing effect of the magnet mentioned previously.

An example of a match between a double ring in RICH-1 and two rings in RICH-2 is shown in Figure 3.9; this is the typical pattern produced by a γ conversion pair.

3.3.6 Data reduction

The data sample that has survived the above steps still suffers from the presence of fake rings and from a large combinatorial background. Fake rings are removed by applying "quality cuts" on the ring properties, e.g. a minimum number of hits/ring is a useful cut since a ring with too few hits has a high probability to be a fake one. Another example of a quality cut is the sigma of the fitted ring; rings with larger sigma, see Equation 3.1, are more probable to be fakes. In Figure 3.10 the variations of the signal, S, and the signal-to-background ratio, S/B, defined in the next section, as a function of the fitted ring sigma are shown. The cut is such that

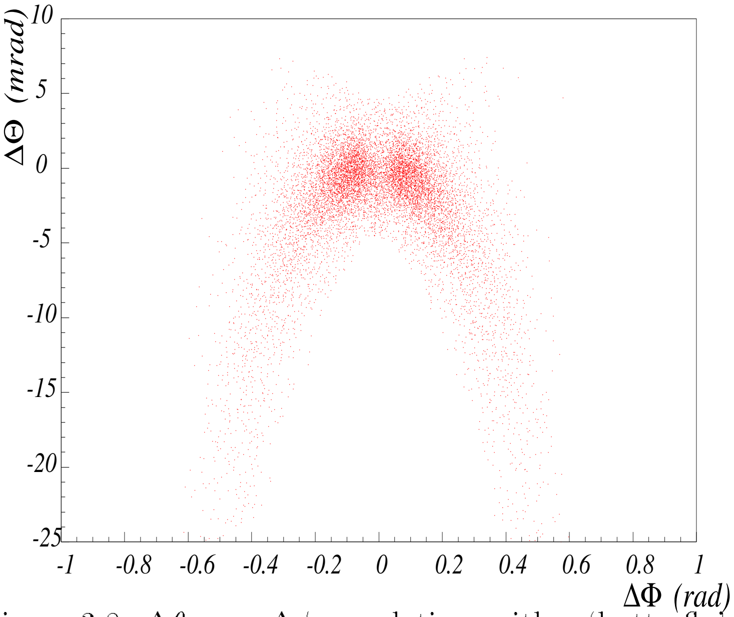

Figure 3.8: $\Delta\theta$ vs. $\Delta\phi$ correlation, with a 'butterfly' shape. The plot was produced by accumulating many tracks.

only rings which satisfy the condition $\sigma_{fit} < x$ where x is the abscissa in the plots are accepted. This behavior of the signal and the signal to background as a function of the cut strength is typical also for the rest of the cuts where an improvement in the signal to background ratio is accompanied by a loss in the signal. Therefore, we try to improve the S/B but with the minimum possible loss in the signal.

3.3.7 Extraction of the signal

The next step in the analysis after fake tracks are removed is to identify all the contributions to the combinatorial background. In Figure 3.11 typical patterns that may occur in an event are sketched: on the top is the desired open pair where clearly isolated rings in RICH-1 have the corresponding rings in RICH-2. We would be happy to have from those as many as possible! (see Figure 3.14 and 3.15). In the middle of figure 3.11 are shown a typical π^0 Dalitz pair (left) and a conversion pair (right). A Dalitz pair is easily recognized because it has small invariant mass and its RICH-1 rings have a small opening angle. As mentioned before, a conversion pair is identified by its characteristic "V" pattern of one double ring in UV-1 and two open rings in UV-2. (a pair with zero mass has a zero opening angle giving rise to two overlapping rings in RICH-1, see Equation 3.2 below). The bottom

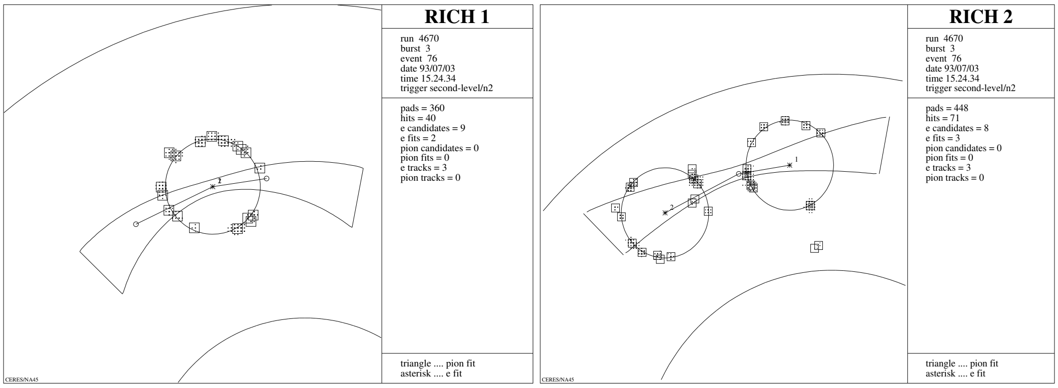

Figure 3.9: A single ring in RICH-1 is matched to two rings in RICH-2 which were found inside the butterfly search area. This is a typical γ conversion pair.

of Figure 3.11 shows a partially reconstructed π^0 Dalitz pair (left) and a partially reconstructed conversion (right), where one ring in RICH-2 was not found, either because of inefficiency of the pattern recognition or because of the 50MeV/c p_T cut.

Therefore, the analysis proceeds through the next 3 steps:

- Fully reconstructed γ conversion and π^0 Dalitz pairs identified by the pattern described above. They are marked and not being paired with the other tracks[1].

- Single tracks from γ conversion and π^0 Dalitz decays are rejected: The identification of a single ("1 leg") π^0 Dalitz track is done by searching for an additional close ring in RICH-1 (within an angular distance of less than 35mrad) that does not belong to a track. A single conversion track can also be identified: since the conversion rings overlap in UV-1, the expected number of hits/ring and the total ring amplitude should be larger than that of a single ring. These properties are used to cut on the maximum number of hits/ring and on the maximum allowed total ring amplitude. The differences between single and double rings in terms of the number of hits/ring and the ring total amplitude are shown, for the p-Be data, in Figures 3.12 and 3.13.

---

[1] Note that the π^0 Dalitz decays having an opening angle smaller than the double ring resolution of RICH-1 will produce a V pattern as most of the γ conversions do, and conversely, a few γ conversions are opened enough by the multiple-scattering to produce the characteristic pattern of a π^0 Dalitz decay.

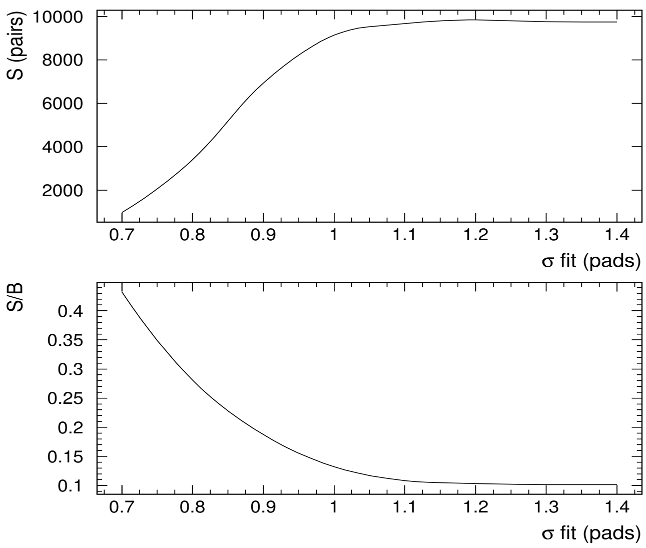

Figure 3.10: Variation of the signal (upper plot) and the signal to background ratio (lower plot) as a function of a cut on the fitted ring sigma, see text.

- The rest of the tracks are combined into pairs which participate in the electron-positron sample together with the fully reconstructed π^0 Dalitz pairs. A textbook example of an open pair in RICH-1 and RICH-2 is shown in Figures 3.14 and 3.15.

The signal, S, can be determined by the following two methods:

- $S = U - L$

or

- $S = U - 2\sqrt{(++) \cdot (--)}$

Where U is the unlike sign and L is the like sign pairs. In the first method the background, B, is equal to L, while in the second method the background is twice the geometrical mean of the $(++)$ and the $(--)$. Both methods give essentially the same results since $(++) \approx (--)$.

The pair invariant mass squared is determined from the two electron tracks by:

$$m^2 = s = (p_1^{(4)} + p_2^{(4)})^2$$

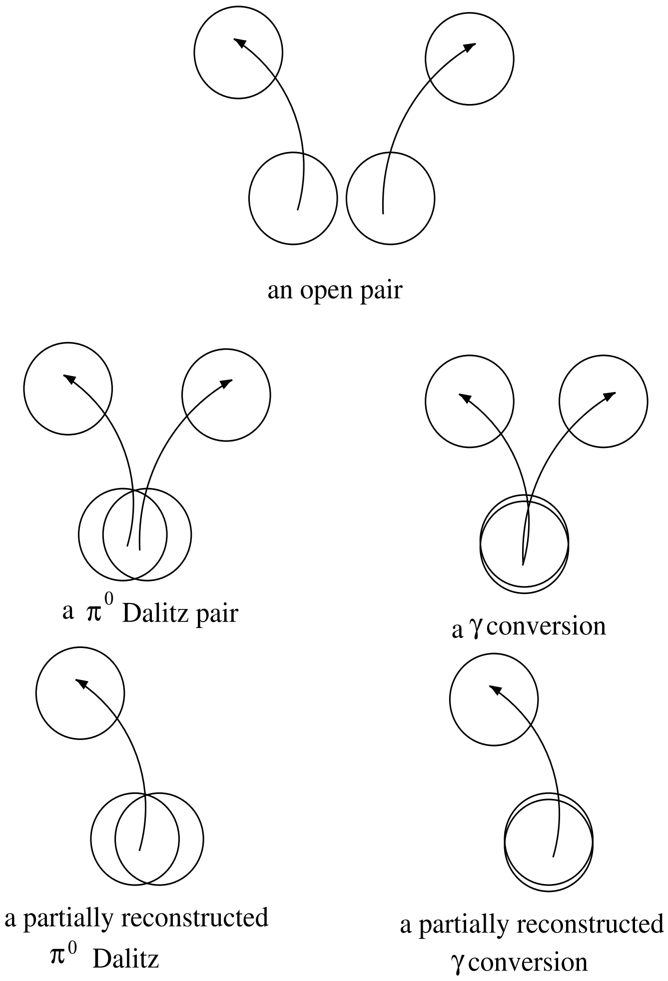

Figure 3.11: All possible types of unlike sign electron pairs that may occur in an event.

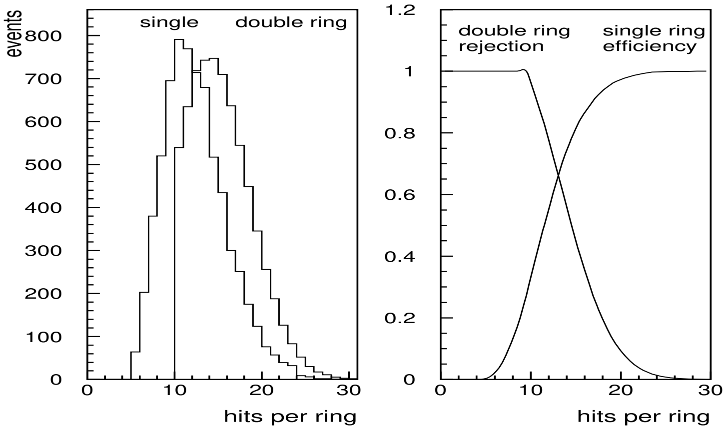

Figure 3.12: The difference in the hits/ring distribution between single and double (conversion) rings in UV-1 -left. The corresponding double ring rejection probability and the single ring efficiency curves based on the number of hits cut - right.

where, $p^{(4)}$ is the electron 4-momentum.

$$m^2 = (E_1 + E_2)^2 - (\vec{p_1} + \vec{p_2})^2$$

for highly relativistic electrons $E \simeq p$, and therefore:

$$m \simeq \sqrt{2p_1p_2(1-\cos\Omega)} \tag{3.2}$$

where the momentum is determined from the deflection between UV-1 and UV-2, see Equation 2.6, and Ω is the opening angle calculated from $\cos\Omega = \hat{r_1}\cdot\hat{r_2}$, where:

$$\hat{r_i} = (\sin\theta_i\cos\phi_i, \sin\theta_i\sin\phi_i, \cos\theta_i)$$

and $i = 1, 2$ for the two electrons in RICH-1.

3.3.8 Results

The p-Be results, for $m > 200\mathrm{MeV/c^2}$, are presented in Table 3.3 [2]. The three lines

---

[2] In this work the quoted signal to background is calculated for $m > 200\mathrm{MeV/c^2}$, even if a mass spectrum is shown also for $m < 200\mathrm{MeV/c^2}$. The reason is that at lower masses

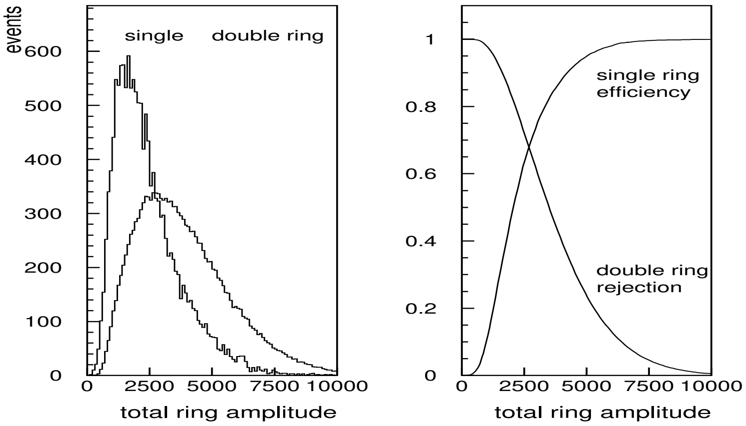

Figure 3.13: The difference in the ring amplitude between single and double (conversion) rings in UV-1 - left. The corresponding double ring rejection probability and the single ring efficiency curves based on the ring amplitude cut - right.

in the table correspond to 3 different levels of signal to background, obtained by choosing tighter cuts ($S/B = 0.10, 0.45$ and 1.04). The first column is the number of unlike sign pairs ($+-$), U. The second column is the number of like sign pairs L. In the third column the signal S, defined as $S = U - L$, is given. The relative error in the signal is shown in the next column and it is calculated from:

$$\Delta S = \sqrt{(\Delta U)^2 + (\Delta L)^2}$$

Assuming:

$$\frac{\Delta U}{U} \sim \frac{1}{\sqrt{U}}$$

and

$$\frac{\Delta L}{L} \sim \frac{1}{\sqrt{L}}$$

we get,

$$\Delta S = \sqrt{U + L}$$

---

the S/B is very good and the mass region of interest is above the π^0 Dalitz contribution.

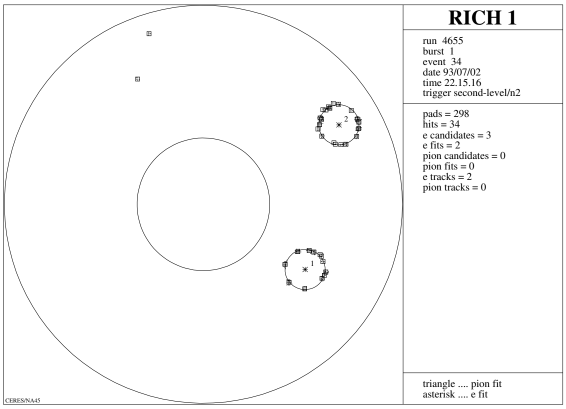

Figure 3.14: A typical open-pair in RICH-1.

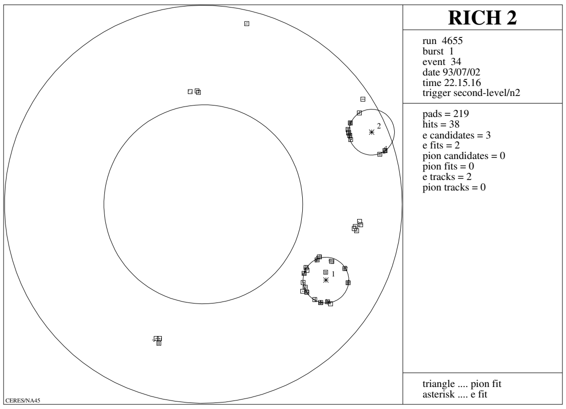

Figure 3.15: The same event in RICH-2.

unlike sign $\mathbf{U} = (+-)$	**like sign** $\mathbf{L} = (--) + (++)$	**signal** $\mathbf{S} = \mathbf{U} - \mathbf{L}$	$\frac{\Delta \mathbf{S}}{\mathbf{S}}$ (%)	$\frac{\mathbf{S}}{\mathbf{B}}$	**bkgd free equivalent**
$105,871$	$96,123$	$9,748 \pm 449$	4.6	0.1	470
$18,483$	$12,727$	$5,756 \pm 177$	3.1	0.45	$1,060$
$6,786$	$3,334$	$3,452 \pm 101$	2.9	1.04	$1,170$

Table 3.3: The analyzed p-Be sample for 3 levels of S/B for $m > 200\text{MeV/c}^2$.

In the 5th column S/B is given where the background, B, is simply the number of like-sign pairs, L. The last column of the table shows the background-free equivalent number of pairs, N, i.e. the signal size with the same statistical accuracy if it were to be absolutely free of background. N is therefore obtained by the relation:

$$\frac{\Delta S}{S} \sim \frac{\Delta N}{N} \sim \frac{1}{\sqrt{N}}$$

The passage from the first line to the second line of Table 3.3 is obtained by applying several cuts: limiting the number of fitted electron rings ($n \leq 3$) acts as an event cleaning step, in addition 3 quality cuts are applied (number of hits/ring$\geq$ 6, variable fit radius is not smaller than 13.7 pads in RICH-1 (see Section 3.3.4) and the sigma of the fitted ring radius is less than 1 pad) all these steps remove fake and pion rings. Finally, 2 physical cuts are applied (total ring amplitude ≤ 5000 counts, which reject conversion rings in RICH-1 and 2^0 angular cut on the closest ring which does not belong to a track to reject partially reconstructed Dalitz pairs).

The passage from the second line to the third line of Table 3.3 is obtained simply by adding the requirement of only 2 electron tracks in the event!

One can see that the number of background-free equivalent pairs improves dramatically between the first and the second lines of the table. However, there is not much improvement by going from the second line to the third line, although the S/B improves by a factor of 2.3. The relation between the signal and the background-free signal to the S/B is plotted in Figure 3.16,

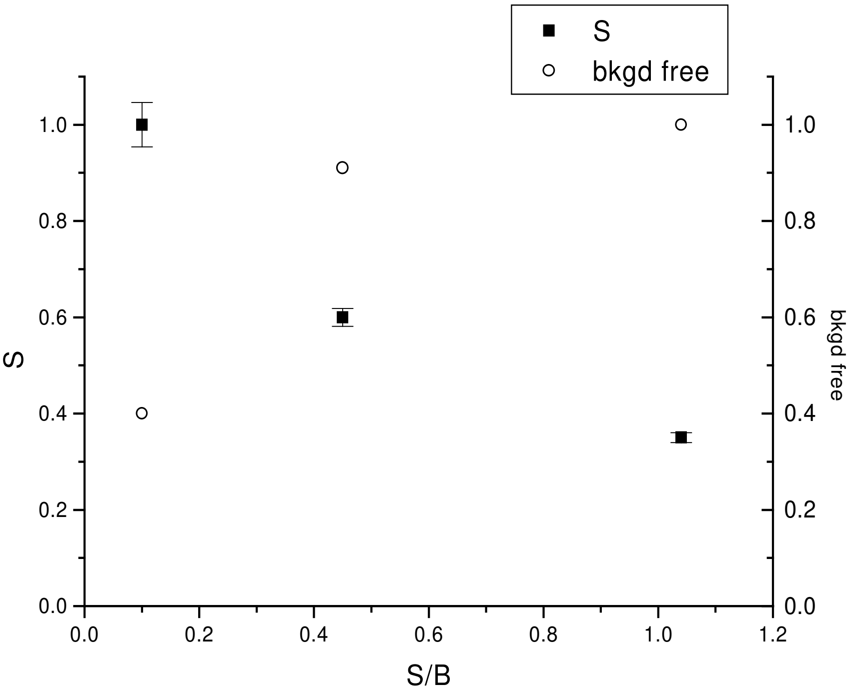

Figure 3.16: The signal and the background-free signal as a function of the S/B. (Both the signal and the background-free were normalized to 1 at their maximum value.)

The e^+e^- mass spectrum for $S/B = 0.45$ is shown in Figure 3.17. The unlike-sign and the like-sign pairs (shaded) are shown on the left hand side. The signal, obtained by subtracting the like-sign pairs from the unlike-sign pairs (with statistical errors included) is shown on the right hand side of the figure.

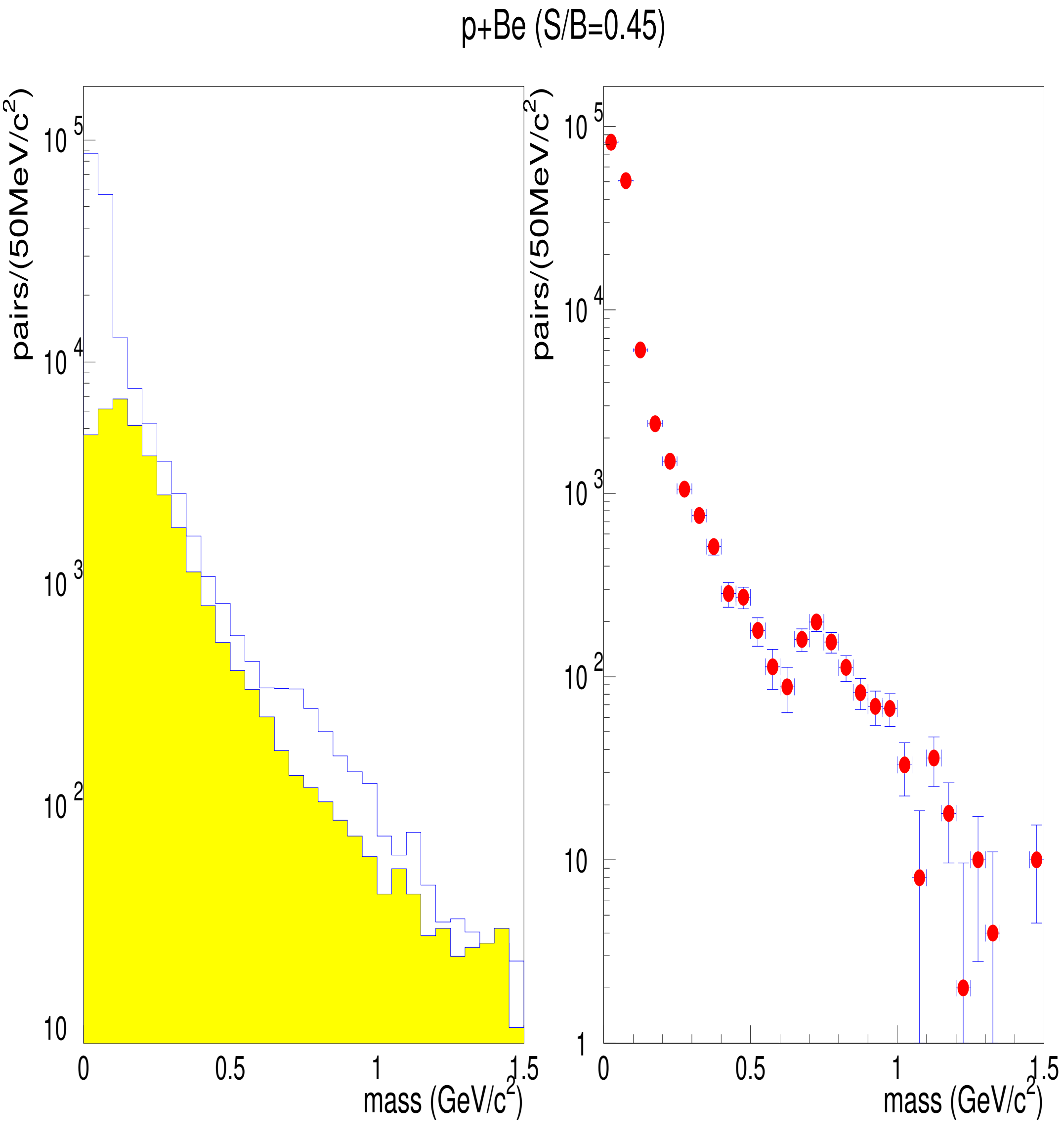

Figure 3.17: e^+e^- mass spectrum for $S/B = 0.45$. The unlike-sign and the like-sign pairs (shaded) are shown in the left side. The signal, i.e. unlike-sign minus the like-sign pairs (with statistical errors included) is shown in the right side. In these plots a $p_T > 50$MeV/c cut and a 2^o opening angle cut were applied.

Chapter 4

The Event generator

"Tenenbaum's Law of Replicability:
The most interesting results happen only once [66]"

In the framework of this thesis, we have developed an event generator which generates e^+e^-pairs from all known hadronic sources that contribute to the mass range covered in the CERES experiment [67]. This is an essential tool to compare the measured e^+e^-invariant mass spectrum to the expectation from known sources and to address the controversial issue of "anomalous" pair production.

The hadronic sources for electron-positron pairs in the low mass region accessible by CERES are: π^0, $\eta(547)$, $\rho^0(770)$, $\omega(782)$, $\eta\prime(958)$ and the $\phi(1020)$. The ρ^0, ω and ϕ are vector mesons, $J^{PC} = 1^{--}$, and therefore can decay to e^+e^- while the π^0, η and $\eta\prime$, $J^{PC} = 0^{-+}$, have a Dalitz decay channel to $e^+e^-\gamma$. The ω has an additional channel to e^+e^-via a Dalitz decay to $e^+e^-\pi^0$. The event generator simulates all these hadronic e^+e^- production processes, namely[1]: $\rho^0, \omega, \phi \rightarrow e^+e^-$, $\pi^0, \eta, \eta\prime \rightarrow e^+e^-\gamma$ and $\omega \rightarrow e^+e^-\pi^0$.

As it will be explained in the next chapter, the CERES results are absolutely normalized to represent the pair production probability per event and per charged particle multiplicity measured in the CERES rapidity acceptance. Therefore, we

---

[1] Other e^+e^-channels, e.g. $\eta \rightarrow e^+e^-\pi^+\pi^-$ or $\phi \rightarrow \eta e^+e^-$ are neglected because their total cross section is small or because they contribute a negligible amount in a given mass range compared with other processes. This also applies for charm contribution which was studied by HELIOS and found to be insignificant in the low-mass region [43].

must normalize the event generator in the same way in order to compare the two. This can easily be done. Since the generator contains the π^0 Dalitz channel, all the contributions can be relatively normalized with respect to the π^0. They are then multiplied by the $\frac{n_{\pi^0}}{n_{\text{ch}}}$ ratio which is approximately equal to 0.5 and can be estimated from the NA27 results in p-p at 400GeV [68], see Section 4.5.

The event generator produces hadrons over the full phase space using a modified Bourquin-Gaillard (B-G) parameterization of the cross section, $\frac{d^2\sigma}{dp_T^2 dy}$, see section 4.3. After the decay, the e^+ and e^- are subject to the acceptance cuts of the detector and the cuts of the data analysis procedure, allowing to generate an inclusive mass spectrum which we call a cocktail plot, since it contains all processes with their proper strength.

In this chapter we describe in detail the information required for the estimation and normalization of the various processes. We also discuss in detail the production (y and p$_T$ distribution) and decay properties (form factor, angular distribution) of the sources.

4.1 Relative particle production cross sections

We now specify the cross section of all the relevant particles with respect to the π^0 in one unit of rapidity around center of mass, see second column of Table 4.1. This information is primarily obtained from the $\gamma\gamma$ TAPS measurement (in the pseudo rapidity interval $3.1 < \eta < 4.0$) which took place during the joint CERES-TAPS p run of 1993 [69]. TAPS ratios for the η and the ω mesons are:

$$(d\sigma_\eta/dy)/(d\sigma_{\pi^0}/dy) = 0.065 \pm 0.010$$

and

$$(d\sigma_\omega/dy)/(d\sigma_{\pi^0}/dy) = 0.091 \pm 0.010$$

These results are lower by about 30% with respect to the NA27 results [68], however they are supported by another measurement by HELIOS which found an η/π^0 ratio of 0.057 ± 0.007 averaged over the p$_T$ range from 0 to 1.5GeV/c [70]. Actually, the η/π ratios of CERES-TAPS, HELIOS and NA27 are in rather good agreement for p$_T > 0.4$GeV/c. At lower p$_T$ HELIOS and CERES-TAPS data are also in agreement, however NA27 did not measure below p$_T < 0.4$GeV/c and therefore relied on an extrapolation to determine the total cross section and this may be the source of the discrepancy.

The ρ^0/π^0 ratio was not measured by TAPS. This ratio was derived assuming $d\sigma_\omega/dy = d\sigma_{\rho^0}/dy$ following quark-parton models that predict equal total cross section for the ρ^0 and the ω [71]. This assumption is confirmed by NA27 and other experimental results [68, 72, 73] within an accuracy of about 10%. We therefore obtain

$$(d\sigma_{\rho^0}/dy)/(d\sigma_{\pi^0}/dy) = 0.091 \pm 0.014$$

particle	$(\frac{\mathrm{d}\sigma/\mathrm{dy}}{\mathrm{d}\sigma_{\pi^0}/\mathrm{dy}})_{\mathrm{y}=0}$	decay process	branching ratio to e^+e^- [60]
π^0	1	$\pi^0 \rightarrow e^+e^-\gamma$	$(1.198 \pm 0.032) \times 10^{-2}$
η	0.065 ± 0.010 (a)	$\eta \rightarrow e^+e^-\gamma$	$(5.0 \pm 1.2) \times 10^{-3}$
ρ^0	0.091 ± 0.014 (b)	$\rho^0 \rightarrow e^+e^-$	$(4.46 \pm 0.21) \times 10^{-5}$
ω	0.091 ± 0.010 (a)	$\omega \rightarrow e^+e^-$ $\omega \rightarrow e^+e^-\pi^0$	$(7.15 \pm 0.19) \times 10^{-5}$ $(5.9 \pm 1.9) \times 10^{-4}$
η'	0.024 ± 0.004 (b)	$\eta' \rightarrow e^+e^-\gamma$	$(6.4 \pm 3.0) \times 10^{-4}$ (b)
ϕ	0.0044 ± 0.0008 (b)	$\phi \rightarrow e^+e^-$	$(3.09 \pm 0.07) \times 10^{-4}$

(a) TAPS. (b) see text.

Table 4.1: Relative cross section of the relevant mesons and their branching ratio to e^+e^-.

Since we do not have also our own measurement of the ϕ meson relative yield, we derive it assuming $\phi/(\rho^0 + \omega) = 0.024 \pm 0.005$ from NA27 [68] and obtain:

$$(d\sigma_\phi/dy)/(d\sigma_{\pi^0}/dy) = 0.0044 \pm 0.0008$$

There is no data for the η' production cross section. We have assumed it to be $1/3$ of the η total production cross section. This result is derived in Ref. [74], where η/π and η'/π are extrapolated from high p_T measurements. Using this information and our p_T-y parameterization (see Section 4.3) we derive:

$$(d\sigma_{\eta'}/dy)/(d\sigma_{\pi^0}/dy) = 0.024 \pm 0.004$$

There is also no information available for the $\eta' \rightarrow e^+e^-\gamma$ branching ratio. However, the branching ratio of the η' to $\mu^+\mu^-\gamma$ does exist: BR($\eta' \rightarrow \mu^+\mu^-\gamma$) = $(1.04 \pm 0.26) \times 10^{-4}$ [60]. Assuming e/μ universality, namely that the e/μ ratio in one meson decay is the same for another meson, we use the ratio:

$$\frac{\Gamma(\omega \rightarrow e^+e^-\pi^0)}{\Gamma(\omega \rightarrow \mu^+\mu^-\pi^0)} = 6.15 \pm 0.40$$

Vector Meson	**Mass** (**MeV/c^2**)	**Full width** (**MeV/c^2**)
ρ^0	770	151
ω	782	8.4
ϕ	1020	4.4

Table 4.2: Mass and width of the three lowest vector mesons.

taken from Ref. [60] to derive BR($\eta' \rightarrow e^+e^-\gamma) = (6.4 \pm 1.7) \times 10^{-4}$.

4.2 e^+e^-mass generation

4.2.1 Direct decay of vector mesons

Table 4.2 gives a short summary of the mass and width of the ρ^0, ω and ϕ vector mesons.

The vector meson mass is generated according to the Gounaris-Sakurai (G-S) parameterization [75]. The advantage of this parameterization over the classical Breit-Wigner (B-W) formula is that it takes into account some corrections derived on the basis of the vector-meson dominance model:

$$F_{GS}(m) = \frac{N_1}{m_\rho^2 - m^2 + i m_\rho \Gamma_\rho (\frac{m^2/4 - m_\pi^2}{m_\rho^2/4 - m_\pi^2})^{3/2} \frac{m_\rho}{m}}$$

The ρ^0 meson G-S line shape is therefore:

$$\frac{dN}{dm} = \frac{N_2}{(m_\rho^2 - m^2)^2 + m_\rho^2 \Gamma_\rho^2 (\frac{m^2/4 - m_\pi^2}{m_\rho^2/4 - m_\pi^2})^3 (\frac{m_\rho}{m})^2} \qquad (4.1)$$

An s-wave B-W shape is:

$$\frac{dN}{dm} = N_3 \frac{1}{\pi} \frac{\Gamma/2}{(m - m_\rho)^2 + (\Gamma/2)^2} \qquad (4.2)$$

and a p-wave B-W shape is:

$$\frac{dN}{dm} = N_4 \frac{m m_\rho \Gamma_\rho}{(m^2 - m_\rho^2)^2 + m_\rho^2 \Gamma_\rho^2} \qquad (4.3)$$

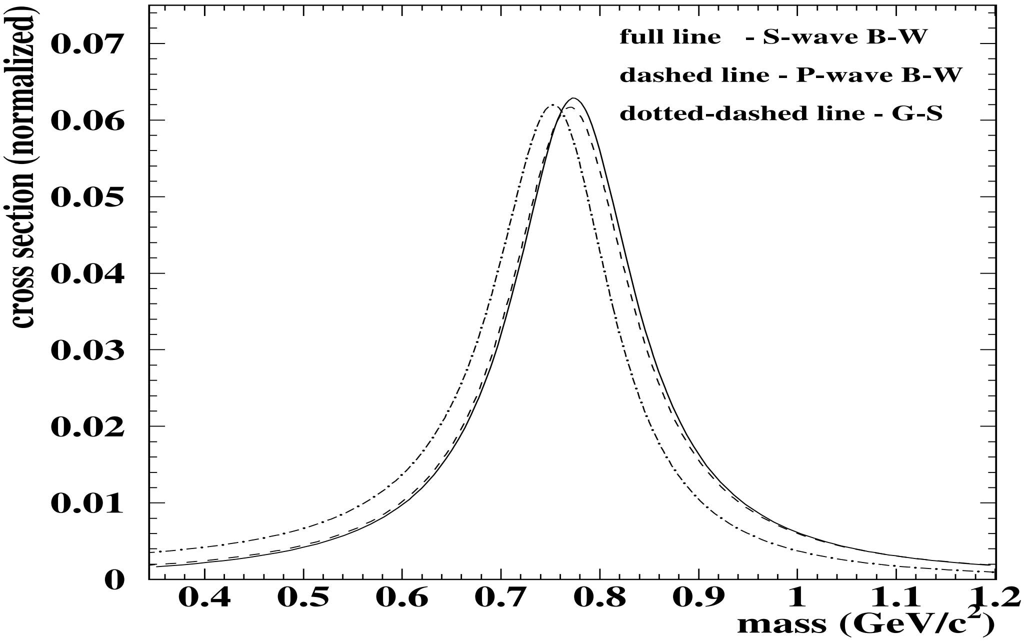

Figure 4.1: A comparison between the an s-wave (full line) and a p-wave Breit-Wigner (dashed line) with the Gounaris-Sakurai (dotted-dashed line) parameterizations for the ρ^0 meson.

The N_i are normalization constants.

A comparison between s and p waves Breit-Wigner and the Gounaris-Sakurai parameterizations, Equations 4.1, 4.2 and 4.3, is given in Figure 4.1. The main difference between the two B-W formulae which are very similar and the G-S formula is the shift of the peak position of about 15MeV/c^2.

ρ^0/ω interference

The ρ^0 and ω have masses close to each other and the same quantum numbers except for the isospin and therefore interfere in common decay channels. The ρ^0 mainly decays into $\pi^+\pi^-$ and the ω into 3 pions, $\pi^+\pi^-\pi^0$ (88.8%), but the ω also has a 2.21% branching ratio into $\pi^+\pi^-$, which indicate that the ω is not a pure state.

The common decay channels where interference takes place are:

$$\rho^0/\omega \to \pi^+\pi^-$$

$$\rho^0/\omega \to \pi^0\gamma$$

$$\rho^0/\omega \to \text{dileptons}$$

In the absence of any interference the mass spectrum is obtained by:

$$|F_{\rho^0}|^2 + w^2|F_\omega|^2 \tag{4.4}$$

while if interference is taken into account the mass line shape is given by:

$$|F_{\rho^0} + we^{i\alpha}F_\omega|^2 \tag{4.5}$$

The F's are the form factors, e.g. Breit-Wigner shapes:

$$F = \frac{1}{\sqrt{\pi}} \frac{\sqrt{\Gamma/2}}{m - m_V + i\frac{\Gamma}{2}}$$

α is the interference angle. w is the weight between the cross sections of the ρ^0 and the ω to e^+e^-:

$$w = \sqrt{\frac{\sigma_\omega \cdot \mathrm{BR}_{\omega\to e^+e^-}}{\sigma_{\rho^0} \cdot \mathrm{BR}_{\rho^0\to e^+e^-}}}$$

In order to obtain a realistic mass spectrum Equations (4.4) and (4.5) should be convoluted with the mass resolution.

There is very little experimental information about the ρ^0/ω interference in p-p collisions. The recent HELIOS studies of dimuons produced in p-Be collisions at 450GeV/c favor an interference angle of $\alpha = 2 \pm 1.2$ radians [43,74]. To illustrate the effect of such an interference in our case we show in Figure 4.2 the mass line shape of Equation (4.4) compared with the mass line shape of Equation (4.5) with $\alpha = 2$ radians (approximated mass resolution is included). One sees a decrease of $\sim 10\%$ in the cross section at the ρ^0/ω peak together with a slight shift of about 10MeV in the peak. Since this effect is so small and its uncertainties very large, the results that will be presented later do not include ρ^0/ω interference.

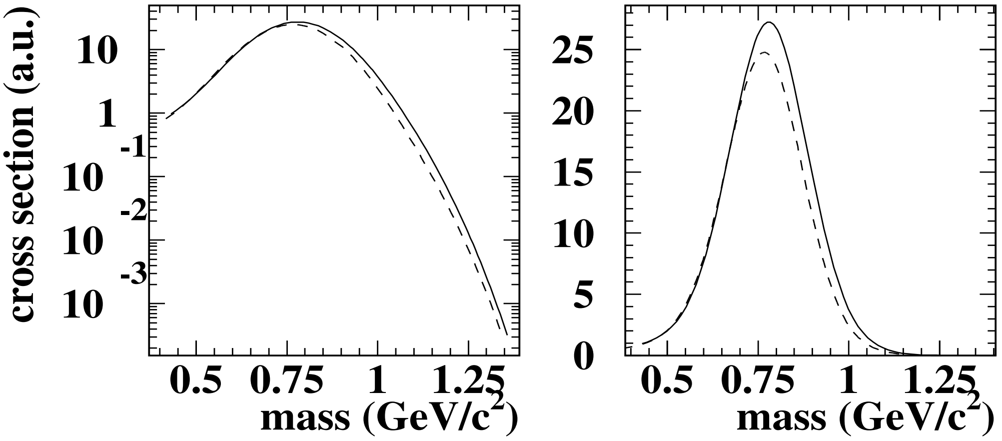

Figure 4.2: Non-interference line shape (full line) and ρ^0/ω interference line shape with $\alpha = 2$ radians (dashed line). Left plot is in logarithmic scale. Right plot is the same in linear scale.

4.2.2 e^+e^-pairs from Dalitz decay

The π^0, η and $\eta\prime$ decays to $e^+e^-\gamma$

The e^+e^- pair mass from Dalitz decays is generated using the Kroll-Wada QED expression [76] multiplied by a form factor [48]:

$$\frac{d\sigma}{dm} = \frac{4\alpha}{3\pi}\Gamma_{\gamma\gamma}\frac{1}{m}(1-\frac{m^2}{m_p^2})^3(1+\frac{2m_e^2}{m^2})\sqrt{1-\frac{4m_e^2}{m^2}}|F(m^2)|^2 \tag{4.6}$$

where m is the e^+e^- mass and m_p is the pseudo scalar mass (π^0, η or $\eta\prime$). $\Gamma_{\gamma\gamma}$ is the partial width into $\gamma\gamma$. The form factor $F(m^2)$ is normalized such that $F(0) = 1$, and it contains, according to the vector dominance model in its simplest form, one term which is parameterized in the pole approximation as:

$$F(m^2) = \frac{1}{1-m^2/\Lambda^2} \tag{4.7}$$

The actual values of Λ are adopted from [48], see Table 4.3.

Meson	Λ (GeV/c^2)
π^0	0.43 ± 0.06
η	0.72 ± 0.09
ω	0.65 ± 0.03
η'	0.77 ± 0.09(*)

(*) but since $m_{\eta'} > m_{\rho^0}$, Λ was taken somewhat arbitrarily above $m_{\eta'}$ in order to avoid divergence around m_{ρ^0}.

Table 4.3: Values of the pole term in the pole approximation of the form factor.

The $\omega \rightarrow e^+e^-\pi^0$process

The e^+e^-mass spectrum for the $\omega \rightarrow e^+e^-\pi^0$ decay is generated according to [48]:

$$\frac{d\sigma}{dm} \propto \frac{1}{m}\sqrt{1-\frac{4m_e^2}{m^2}}[1+\frac{2m_e^2}{m^2}][(1+\frac{m^2}{m_\omega^2-m_{\pi^0}^2})^2-\frac{4m_\omega^2 m^2}{(m_\omega^2-m_{\pi^0}^2)^2}]^{3/2} \times |F|^2 \tag{4.8}$$

where m is the e^+e^-mass. This expression reduces to the usual Dalitz decay expression, Equation 4.6 when the π^0 is replaced by a photon.

The form factor is taken in the pole approximation, Equation 4.7, with a value taken from [48], see Table 4.3. There is only one measurement of the ω form factor, by the Lepton-G experiment, and it does not agree with the VDM prediction, as already discussed in Section 1.4 and Figure 1.7 thereat.

A comparison between e^+e^-pairs generated using the 'measured' [47] and the VDM form factors is shown in Figure 4.3, for pairs in the CERES acceptance (an angular cut of 2^o is applied to the pair and each electron has a p$_T$ $>$ 50MeV/c). In the rest of this work the e^+e^-event generator uses the measured ω form factor.

4.3 p$_T$ and y distribution of the parent particles

The invariant differential cross section $E\frac{d^3\sigma}{d\vec{p}}$ can be expressed as a function of the transverse momentum, p$_T$ and the rapidity y, using the Jacobian

$$\frac{\partial(p_T,\phi,y)}{\partial(p_x,p_y,p_z)} = Ep_T$$

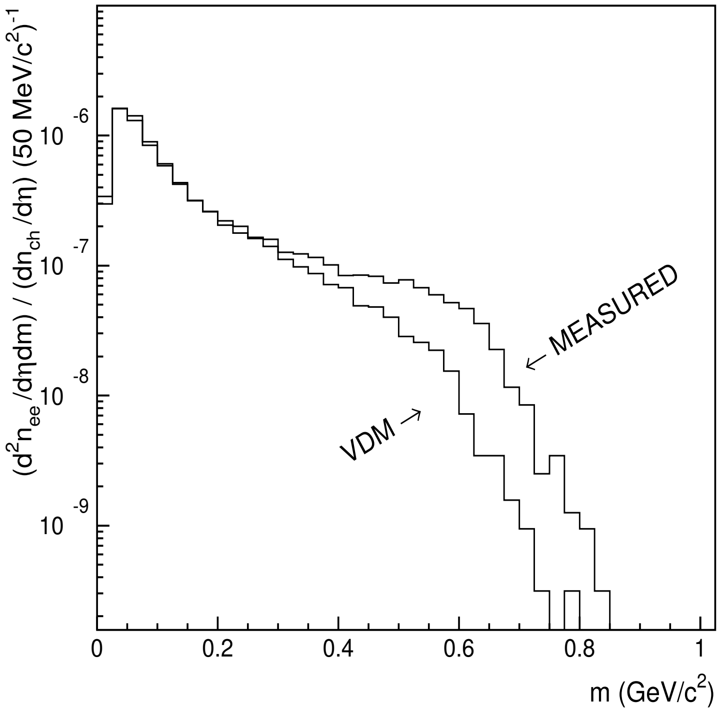

Figure 4.3: The $\omega \rightarrow e^+e^-\pi^0$decay using the measured and VDM form factor (with a pair opening angle cut of 2°, a p_T cut of 50MeV/c on the electrons and in the CERES acceptance).

as:

$$E\frac{d^3\sigma}{dp_x dp_y dp_z} = \frac{1}{p_T}\frac{d^3\sigma}{dp_T d\phi dy}$$

Integrating the above expression over ϕ and assuming azimuthal symmetry one gets,

$$E\frac{d^3\sigma}{d\vec{p}} = \frac{1}{\pi}\frac{d^2\sigma}{dp_T^2 dy}$$

A p_T-y parameterization of the cross section is very useful since the p_T is invariant under a Lorentz transformation along the longitudinal direction and the rapidity distribution shape is preserved and only gets shifted by the rapidity of the moving frame. In this work we use a p_T-y parameterization for the differential cross section based on the successful universal Bourquin-Gaillard parameterization [77,78], which was suggested about twenty years ago and since then fitted well various kinds of data:

$$\frac{1}{\pi}\frac{d^2\sigma}{dp_T^2dy} = \frac{A}{(m_T+B)^C}f(y)\left\{\begin{array}{ll} e^{-p_T} & \text{for } p_T < 1\text{GeV/c} \\ e^{-D(p_T-1)/\sqrt{s}}e^{-1} & \text{for } p_T > 1\text{GeV/c} \end{array}\right.$$

where $B = 2$GeV, $C = 12.3$, $D = 23$GeV, $\alpha = 5.13$ and $\beta = 0.38$ were found by fitting several inclusive π^- experiments in the range 6GeV< $\sqrt{s} < 53$GeV. The transverse mass, m_T, (sometimes also called the transverse energy) is defined in Appendix A and

$$f(y) = e^{-\alpha/Y^\beta}$$

where,

$$Y = y_{max} - y = \ln(\frac{E^{max} + p_L^{max}}{E + p_L})$$

(subscript L (T) is for the longitudinal (transverse) component).
y_{max} is defined as:

$$y_{max}(p_T) = \ln(\frac{E^{max} + p_L^{max}}{m_T})$$

and the maximum allowed meson momentum and energy are:

$$p_L^{max} = \sqrt{p_{max}^2 - p_T^2}, \qquad E^{max} = \sqrt{\frac{s}{4} + m^2}$$

An important consequence of the Bourquin-Gaillard parameterization is known as "m_T scaling", in which the p$_T$ distribution of one particle can be derived from a known p$_T$ distribution of another particle, that is:

$$f(p_T, A) = \left(\ \frac{m_T(p_T,\pi^0)+2}{m_T(p_T,A)+2}\ \right)^{12.3} f(p_T,\pi^0) \tag{4.9}$$

The main drawback of the Bourquin-Gaillard parameterization is that it has a cusp at $y = 0$ which is neither plausible nor supported by the experimental data (see Figure 4.4). Therefore, we have modified the B-G parameterization by replacing the function $f(y)$ by a smoothed function at $y = 0$:

$$f(y) = e^{-\frac{y^2}{2Y^2}}$$

Our parameterization reproduce very well a large amount of momentum and rapidity distributions of particles produced in p-p, p-nucleus and nucleus-nucleus collisions [67]. A couple of examples are given in Figures 4.4 and 4.5.

Figure 4.4 shows a comparison between the modified rapidity parameterizations and measured data, from NA35 π^- produced in 200GeV/n S-S collisions [79]. The original B-G parameterization is also shown in the figure. The modified B-G p_T parameterization is compared with pion p_T spectrum from p-p collisions at 400GeV/c measured by NA27 [68] in Figure 4.5.

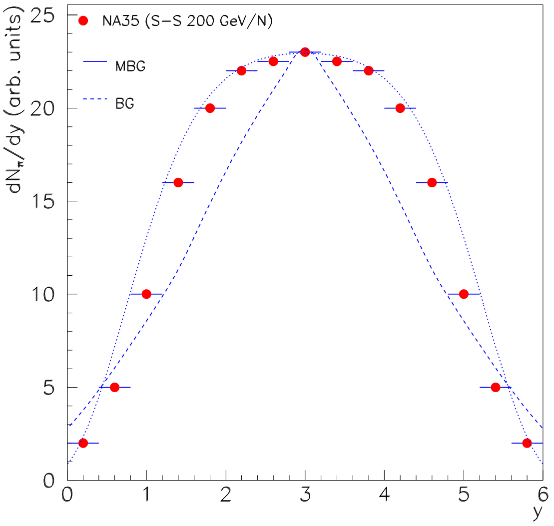

Figure 4.4: The original B-G and the modified B-G (MBG) parameterizations are compared with the NA35 π^- rapidity distribution.

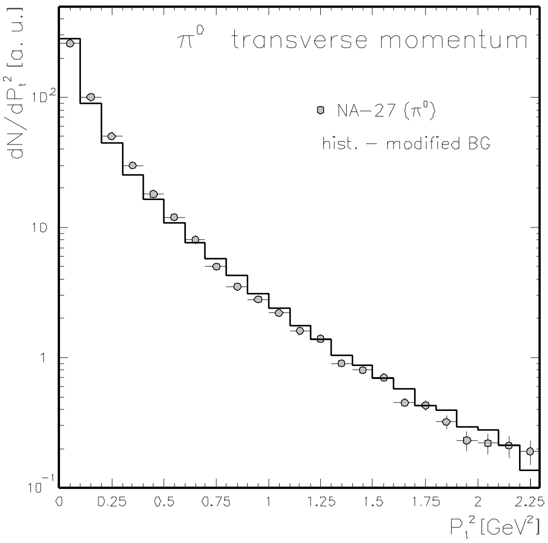

Figure 4.5: The modified B-G p_T parameterization is compared with N27 π^0 p_T spectrum.

The rapidity distribution depends on the particle mass, the larger the mass the narrower it becomes. The rapidity distributions of the π^0, η and ϕ, assuming they have the same total cross section, are shown in Figure 4.6. This fact is important when one estimates the differential cross section in a limited rapidity window, e.g. in the CERES acceptance around $y = 2.35$. In Figure 4.7 the fraction of the cross section falling in one unit of rapidity around the center rapidity of CERES assuming the modified B-G parameterization for the relevant parent particles is shown.

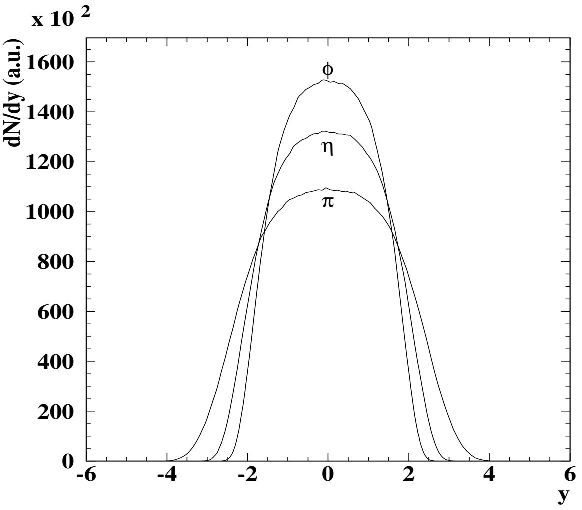

Figure 4.6: The modified B-G rapidity distribution of some of the relevant parent particles, assuming they all have the same normalization.

4.4 Angular distribution

The parent angular distribution in the laboratory frame is derived in the following way: assuming that m and (p_T-y) are already defined, then the transverse mass, m_T, and the longitudinal momentum, p_L can also be calculated (see Appendix A). From p_T and p_L the polar angle, θ is found by:

$$\theta = \tan^{-1}\left(\frac{p_T}{p_L}\right)$$

The azimuthal angle, ϕ, is assumed to be uniformly distributed between 0 to 2π.

For the Dalitz decay, the electron angular distribution is determined in two steps: first, the meson decays to $\gamma\gamma^*$ where the virtual photon has an isotropic distribution, then, the virtual photon decays into e^+e^- and the electron angular distribution is done according to $f(\theta) \sim 1 + \cos^2\theta$. The electrons angular distribution in the laboratory frame is obtained by two consecutive Lorentz transformations, from the pair frame to the parent frame and from there to the laboratory frame.

For the vector mesons, the decay angular distribution depends on the polarization P of the vector meson and is given by $1 + P\cos^2\theta$.

Figure 4.8 compares the angular distribution for no polarization i.e. for isotropic and for full polarization ($P = 1$) i.e. $1 + \cos^2\theta$ distributions. The left plot shows

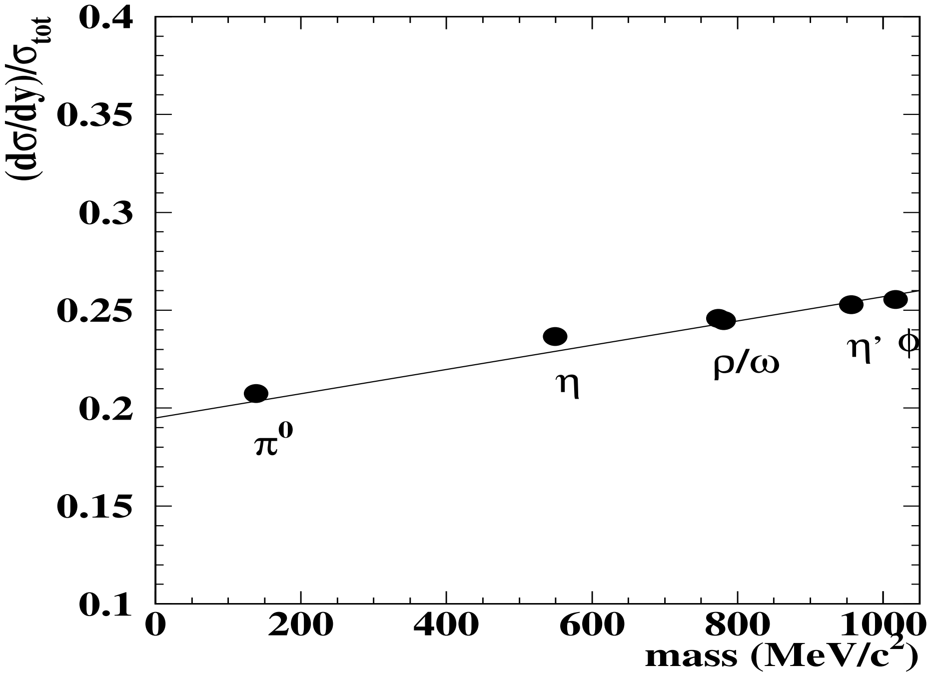

Figure 4.7: The cross section fraction in one unit of rapidity around $y = 2.3$ assuming the modified B-G parameterization.

the angular distribution in full space while the right plot shows the angular distribution in the CERES acceptance. One can see that in the acceptance the two distributions can not be distinguished. Therefore, the polarization distribution of the ρ^0 can not be addressed by CERES. The polarization parameterization however affects the yield of e^+e^-pairs: by assuming in the event generator a term of the form $f(\theta) \sim 1 + P\cos^2\theta$ with $P = 1$ for the decay angle of the ρ^0/ω one would get about 20% less yield in the acceptance compared with a uniform angular distribution. The ρ^0/ω region for fully polarized and isotropic decay angle is shown in Figure 4.9. Very little is known about the value of P. There exists a measurement of muon pairs in the ρ^0/ω region that found a very small value of P which is consistent with an unpolarized distribution [80]. Therefore, we shall assume in the event generator an isotropic angular distribution for the decay angle of the vector mesons.

4.5 Absolute normalization of the Event Generator

In order to compare the MC with the data, the MC pairs are subject to the same cuts as the data (the e^+ and the e^- must be inside the acceptance, they should be above a p$_T$ cut of 50MeV/c and the pair opening angle should be larger than 35mrad). Secondly, since the data are normalized to the charged particle rapidity density (Equation 5.2), the MC is also normalized in the same way, i.e. the normalization (which is given relative to π^0 in Table 4.1) is changed to represent the e^+e^-probability per charged particle by multiplying with the ratio[2]:

$$\frac{n_{\pi^0}}{n_{\mathrm{ch}}}\Big|_{y=0} = 0.48 \pm 0.03$$

This ratio is extrapolated from the NA27 rapidity measurements of the π^0 and of the charged particles $\pi^{\pm}$,$K^{\pm}$ p and $\bar{p}$ [68]. The proton cross section is of course enhanced at the beam rapidity, therefore, in order to estimate the proton production yield we assumed $\sigma_p \simeq \sigma_{\bar{p}}$.

In Figure 4.10 a cocktail plot of all the above processes is shown together with the individual contributions. The shaded band represents the $\pm 1\sigma$ error on the total spectrum. The generator errors are discussed in Section 5.6.1. In this figure, a p$_T$ cut of 50MeV/c on the electrons and an angular cut of $2°$ (35mrad) on the pair opening angle were applied in addition to the CERES acceptance cut.

---

[2] Whenever we specify a quantity measured at a certain rapidity, e.g. $\frac{n_{\pi^0}}{n_{\mathrm{ch}}}|_{y=0}$, we mean that this quantity is measured in one unit of rapidity centered around the specified value, i.e. $-0.5 < y < +0.5$.

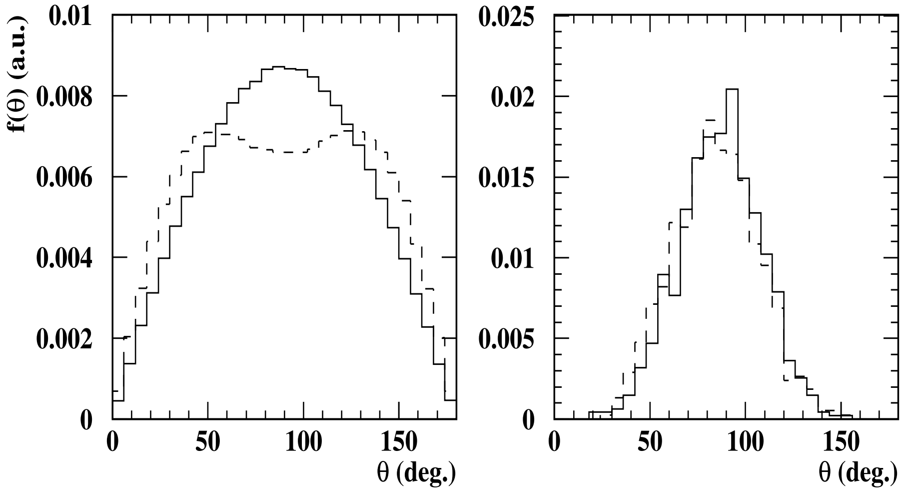

Figure 4.8: Electron polar angle distribution. Isotropic (full line) and a $1+\cos^2\theta$ (dashed line) distributions. Left plot is the angular distribution in full space. Right plot is the angular distribution in the CERES acceptance.

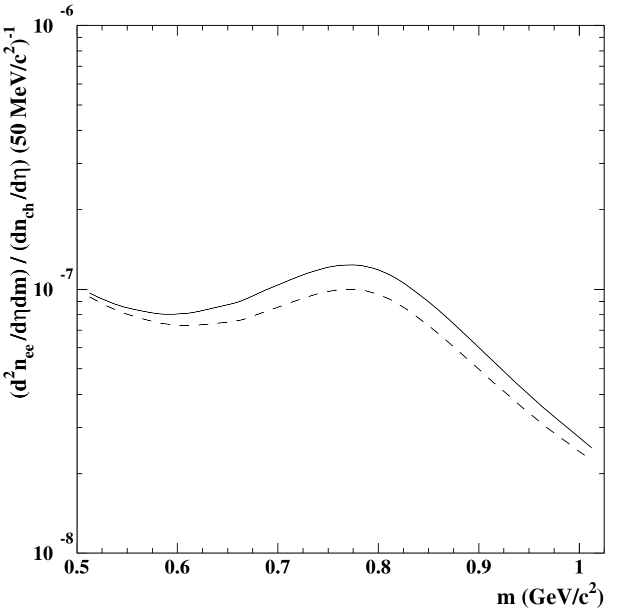

Figure 4.9: A comparison between a flat (full line) and a $f(\theta) \sim 1+\cos^2\theta$ (dashed line) polarization angle distribution.

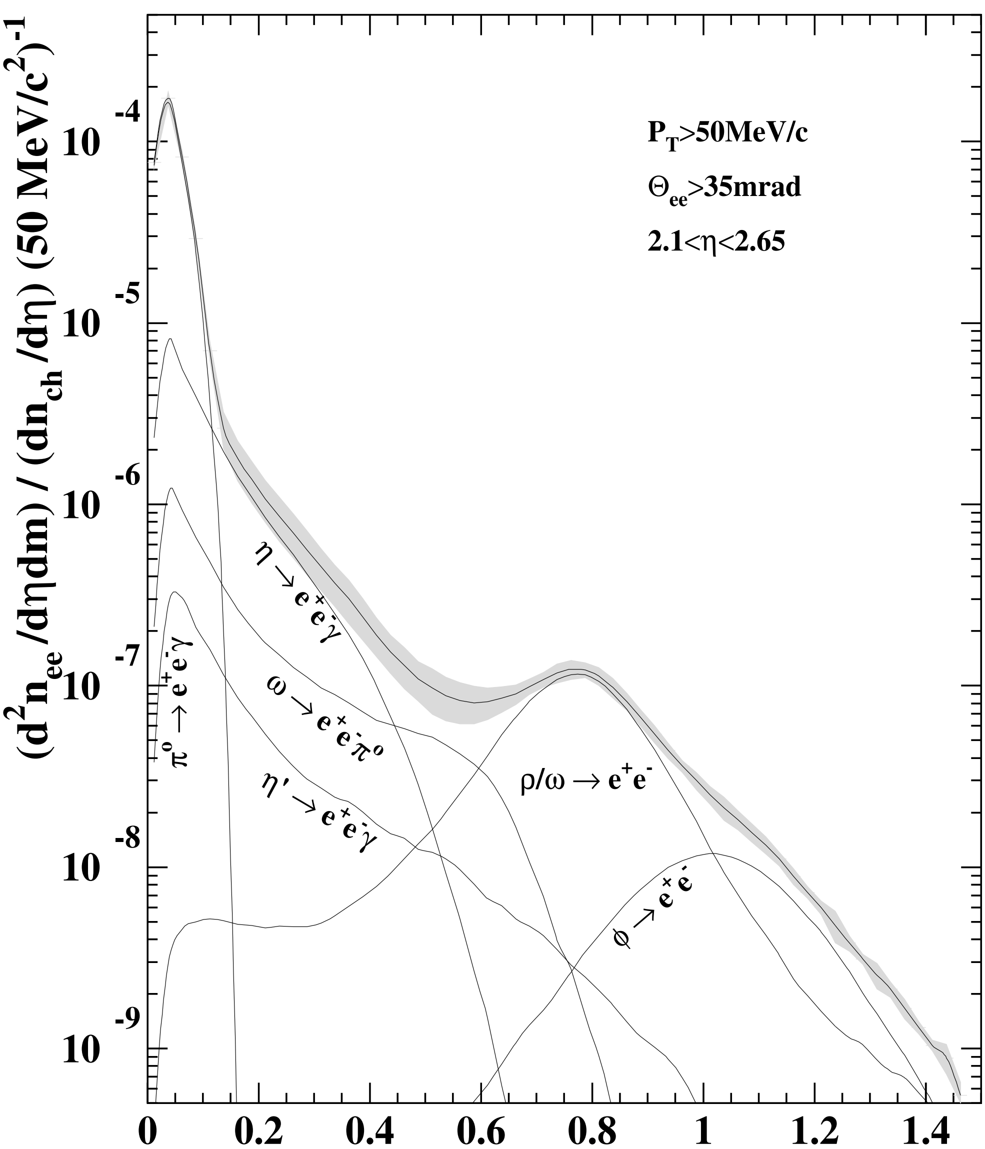

Figure 4.10: Cocktail plot of all the relevant e^+e^-processes. The gray area in this and in the following plots corresponds to the $\pm 1\sigma$ interval. (generator curves were smoothed).

Chapter 5

Physics Results

"In which it is shown that Phileas Fogg has gained nothing by his tour around the world, unless it be happiness" - J. VERNE

This chapter deals with the results of low mass electron pairs produced in p-Be and p-Au collisions at 450 GeV/c. We first discuss the normalization procedure of the data and compare the invariant mass spectrum to the expected one from the known hadronic sources. We then present a detailed analysis of the main sources of error both in the data and the Monte-Carlo event generator. Finally, we conclude with a discussion of the results and with a general outlook on the CERES program.

5.1 Absolute normalization of the data

The basic assumption in the interpretation of the series of measurements performed by CERES of p-p, p-A and A-A collisions is that, in the absence of a new physics, an A-A collision can be considered as a mere superposition of nucleon-nucleon collisions. This implies that the particle production ratios remain constant or in other words that the e^+e^-pair production probability per event scales with the event multiplicity:

$$\left(\frac{dN_{ee}/dy}{dN_{ch}/dy} \right)_{pp} = \left(\frac{dN_{ee}/dy}{dN_{ch}/dy} \right)_{pA} = \left(\frac{dN_{ee}/dy}{dN_{ch}/dy} \right)_{AA} \tag{5.1}$$

Following that assumption, we normalize the data to represent the pair production probability per charged particle within the CERES rapidity acceptance ($2.1 < \eta < 2.65$):

$$\frac{d^2 n_{e^+e^-}/d\eta dm}{dn_{ch}/d\eta} = \frac{N_{rec}(m)}{N_{events}} \times \frac{1}{\text{trigger enrichment } \cdot \epsilon_{rec}(m) \cdot < dn_{ch}/d\eta > \cdot \Delta\eta} \tag{5.2}$$

where,
N_{rec} is the number of reconstructed pairs as a function of the pair invariant mass.
N_{events} is the total number of analyzed events, as quoted in Table 3.2.
ϵ_{rec} is the pair reconstruction efficiency of the off-line analysis. This factor is discussed in the next section.
The trigger enrichment is the product of the FLT bias, b_{FLT}, the ILT+SLT rejection factor, R_T and the ILT+SLT efficiency, ϵ_T. These 3 terms are discussed in Section 3.1.3, where it is shown that for p-Be collisions: $b_{FLT} = 2.42 \pm 0.25$, $R_T = 122 \pm 16$ and $\epsilon_T = 0.55 \pm 0.05$, yielding a trigger enrichment of 162 ± 31. The corresponding values for p-Au are: $b_{FLT} = 1.42 \pm 0.07$, $R_T = 06 \pm 11$ and $\epsilon_T = 0.55 \pm 0.05$ yielding a trigger enrichment of 83 ± 12.
$\Delta\eta = 0.55$ is the CERES fiducial acceptance.
$< dn_{ch}/d\eta >$ is the charged particle rapidity distribution per unit of rapidity at the CERES acceptance and it is discussed in Section 5.3.

5.2 Pair reconstruction efficiency

The pair reconstruction efficiency, ϵ_{rec}, is a measure of the off-line analysis software ability to recognize electron pairs provided that they are in the spectrometer acceptance. The pair efficiency therefore depends on the pattern recognition of the software and on the rejection cuts that are applied on the data sample in order to reduce the combinatorial background and to improve the S/B ratio (see Table 3.3). The pair reconstruction efficiency is determined using the event generator which generates electron pairs in the spectrometer acceptance together with a second Monte-Carlo program which simulates the spectrometer response and in particular the electron rings in the UV detectors. In order for this program to be realistic it uses the measured spectrometer specifications:

- Number of hits/ring. This number has a Poisson distribution with an average number of 15.5 (13.4) hits in RICH-1 (RICH-2) in order to obtain the observed value of 9.4 (10.1) resolved hits per ring, after taking into account the photon losses by pile-up and amplitude threshold, see Section 2.4.2.

- Hit amplitude. Each hit is assigned an amplitude from an exponential distribution with an average of 4.1×10^5 (3.7×10^5) electrons per photon as measured in UV-1 (UV-2).
- Hit size. Once the hit amplitude is fixed, this amplitude is distributed among the participating pads around the hit center using a two dimensional Gaussian shape (with a radial r.m.s of 1 pad). Hits that fall on the detector spokes are removed.
- Position resolution. The generated hit and ring center position take into account the single-hit resolution and the multiple-scattering, see Section 2.4.3.
- Magnetic field deflection. The UV-2 ring center location takes into account the magnetic field deflection in the azimuthal direction, see Equation 2.6 and a small decrease in the polar angle toward the beam axis due to the magnetic field focusing effect.

The MC generated rings are then overlayed on real un-triggered data, in order to simulate the right background. This overlayed event is then passed through the full off-line event analysis chain, including the full trigger emulation. The pair reconstruction efficiency is defined as the ratio between the number of reconstructed MC pairs to the number of generated MC pairs which passed the trigger (emulator). The result as a function of the e^+e^-pair mass is shown in Figure 5.1. At low masses the e^+e^-pairs tend to be close and therefore the pair reconstruction is limited by the double ring resolution; in addition, the electron tracks have low momentum and hence multiple-scattering is more pronounced, this distort the rings and makes the pattern recognition less efficient. Therefore, at lower masses ϵ_{rec} decreases. For $m > 200$MeV/c^2 the pair reconstruction efficiency ϵ_{rec} is $\simeq 0.53$. This means that the single track efficiency is $\simeq 0.73$ and the single ring efficiency is about $\simeq 0.85$ ($\epsilon_{rec} = \epsilon^2_{track} = \epsilon^4_{ring}$).

5.3 Charged particle rapidity density

For the normalization of the p-Be data, we need the average number of charged particles per unit of rapidity within the CERES acceptance, under the proper trigger conditions. During the SLT data taking, we required as a first level trigger,

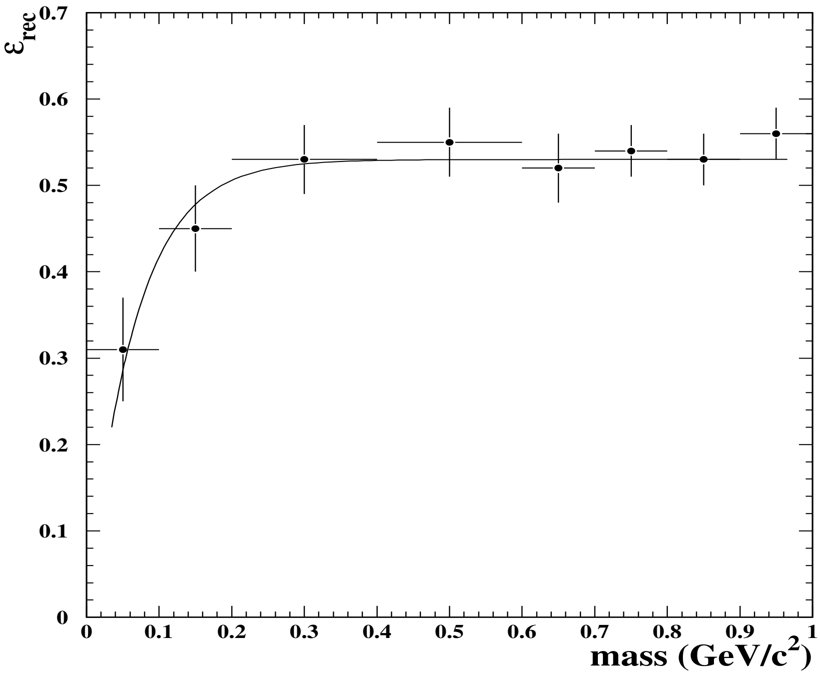

Figure 5.1: Pair reconstruction efficiency versus mass, for S/B=0.45 (a fit of the form $p_1(1 - \exp(-p_2 m))$ is applied, and the asymptotic value is $\epsilon_{rec}^{\infty} = p_1 = 0.53$.

$n_{ch} > 3$ in the silicon pad detector, rings $2 - 5$ which cover the pseudo-rapidity interval $1.95 < \eta < 2.95$. Since in the interesting events with one open pair, the electron and the positron contribute –to first order– two hits to the silicon pad detector, the effective trigger is $n_{ch} > 1$. We therefore need the $< dn_{ch}/d\eta >$ under this condition. In the following we describe the procedure used to derive that information. The starting experimental information is the charge distribution of the events which passed the whole analysis chain including all rejection cuts and with $m > 200$MeV/c^2. The events with an unlike-sign pair have an average charge distribution of 6.70 whereas the like-sign ones have a value of 6.86. The subtraction of the two is shown in Figure 5.2 and gives an average charge distribution of 6.38.

However, the distribution shown in Figure 5.2 does not represent the minimum bias charge distribution associated with our data. In order to get that we have to perform two corrections:

a. subtract the contribution Δ of the electron and the positron hits in the silicon pad detector. In an empty detector, since the pair is rather open $\Delta \simeq 2$. However due to pile-up, the contribution is somewhat smaller. The true horizontal scale of Figure 5.2 is $x' = x - \Delta$ where x denotes the measured total number of hits and x' the real number of charged particles. We have calculated the value of Δ assuming that the hits in the silicon pad detector are uniformly distributed among the 32 pads (4 rings $\times 8$ azimuthal sectors).

b. The shape of the charge distribution of Figure 5.2 is distorted, since the probability to have an electron pair in the event is proportional to the number of charged particles in that event. To restore the minimum bias charge distribution, the vertical scale is divided by the original multiplicity, i.e. $y' = y/x'$.

The minimum bias charge distribution obtained after performing the two corrections is shown in Figure 5.3. The average charge multiplicity for $n_{ch} > 1$ is then:

$$< dn_{ch}/d\eta >= 3.81$$

Three additional small corrections should be applied to this value of $< dn_{ch}/d\eta >$. The first is to take into account the SiPD dead area, this will raise $< dn_{ch}/d\eta >$. The second correction is to take into account e^+e^- pairs which are produced from γ conversions in the target and in the spectrometer material up to the SiPD (mainly from the SiDC). The two close electrons from the γ conversion will contribute a single hit on the SiPD. The third correction is to consider also δ electrons which are produced in the material before the SiPD by the beam. These three effects are all very small, at the few percent level; the last two compensate for the first one so that the net effect in $< dn_{ch}/d\eta >$ is nearly negligible.

Consistency checks

a) $\mathrm{n_{ch}}$ from FLT tapes.

Two FLT runs were taken by requiring $n_{ch} > 3$ on the same rings 2–5 as in the SLT data. The corresponding n_{ch} distribution shown in Figure 5.4 has an average value $< dn_{ch}/d\eta >= 5.78$. This can be compared to the value $< dn_{ch}/d\eta >= 5.47$ derived from Figure 5.3 under the same condition $n_{ch} \geq 4$.

b) FLT bias

The FLT introduces a bias since for the events with an e^+e^-pair the effective trigger is $n_{ch} > 1$. The FLT bias is therefore defined as the ratio of interactions with $n_{ch} > 1$ and with $n_{ch} > 3$. This ratio was monitored on-line during the whole experiment yielding an average value of $b_{FLT} = 2.42$. From Figure 5.3 we derive a value of 2.36.

Conclusion

From all the above we conclude that the average n_{ch} of the p-Be data is 3.8 with a systematic error of $\sim 5\%$.

$$< dn_{ch}/d\eta >= 3.8 \pm 0.2$$

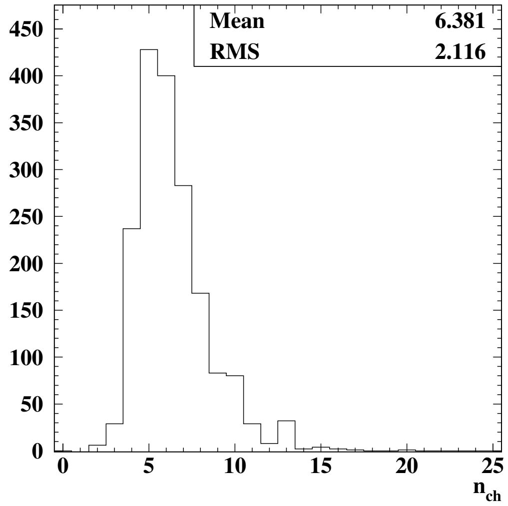

Figure 5.2: rings 2–5, $\Delta\eta = 1$ raw n_{ch} distribution of unlike-like sign pairs.

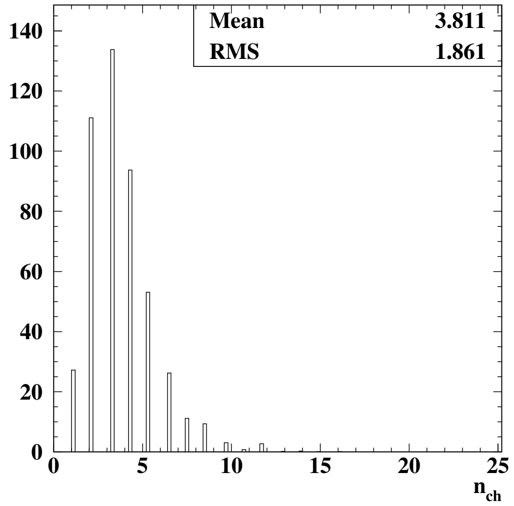

Figure 5.3: rings 2–5, $\Delta\eta = 1$ corrected n_{ch} distribution of unlike-like sign pairs.

5.4 p-Be Mass Spectrum

In this section we compare the invariant mass spectrum measured in p-Be to the expected yield from the known hadronic decays. We use two different methods in this comparison, both exploiting the results obtained within the same run in conjunction with the TAPS calorimeter.

a) In the first method, the data are normalized according to Equation 5.2 and the hadronic cocktail uses the particle production ratio $\pi^0 : \eta : \omega = 100 : 6.5 \pm$

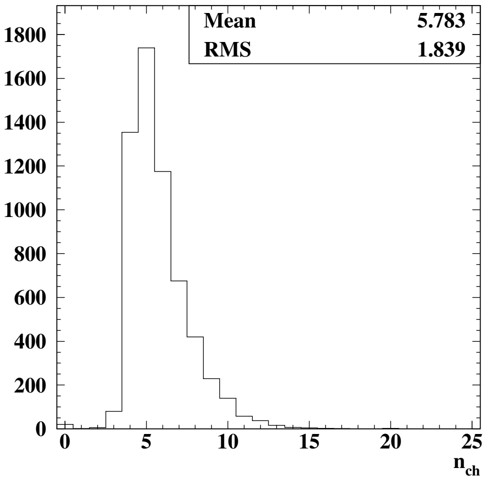

Figure 5.4: FLT run with $n_{ch} > 3$.

$1 : 9.1 \pm 1$ as determined by TAPS at $\eta = 3.4$ from the $\gamma\gamma$ decay channel of these particles [69] (see Table 4.1 and text thereby). The results are shown in Figures 5.5 and 5.6 for a signal to background of 0.1 and 0.45 respectively[1]. The bars in the data points represent the statistical errors and the brackets represent the systematical errors plotted independently. The total yield expected from the known hadron decays is shown by the solid line with $\pm 1\sigma$ uncertainty represented by the hatched band. The figures show also the various hadronic contributions separately. A detailed discussion of all the error sources both in the data and in the generator is given in Section 5.6.

b) The major drawback of the above comparison between the event generator and the data is the relatively large error of the event generator in the mass range $0.2 < m < 0.55$ dominated by the $\sim 24\%$ error in the $\eta \rightarrow e^+e^-\gamma$ branching ratio. Adding to that the η cross section error from the TAPS measurement ($\sim 16\%$) and the other systematic errors in the event generator, the overall error in this mass range becomes $\sim 30\%$. We therefore use a different method of comparison between the event generator and the data, which does not require a

---

[1] In all the e^+e^- mass figures there is no pair acceptance correction of the data. Instead, the simulated events are subject to the pair acceptance cut of the spectrometer. Mass resolution is added to the simulated events using a convolution between the electrons momentum and the spectrometer momentum resolution function.

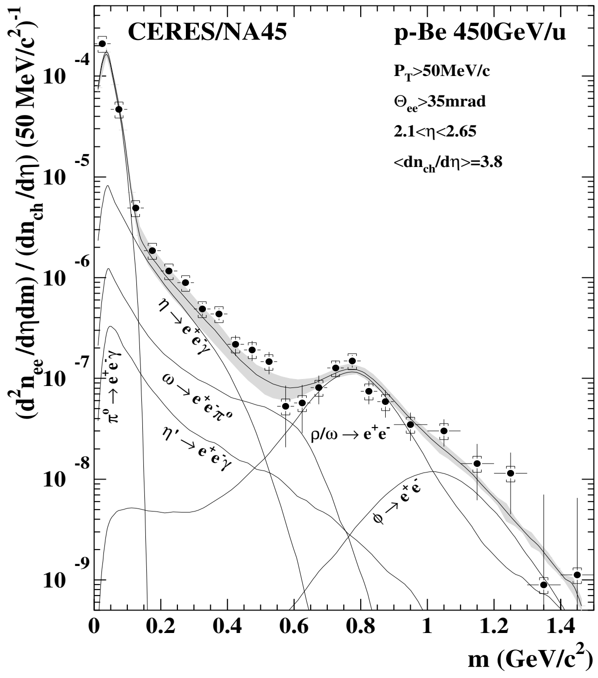

Figure 5.5: The final p-Be mass spectrum with statistical and systematical errors, for a signal to background of 0.1.

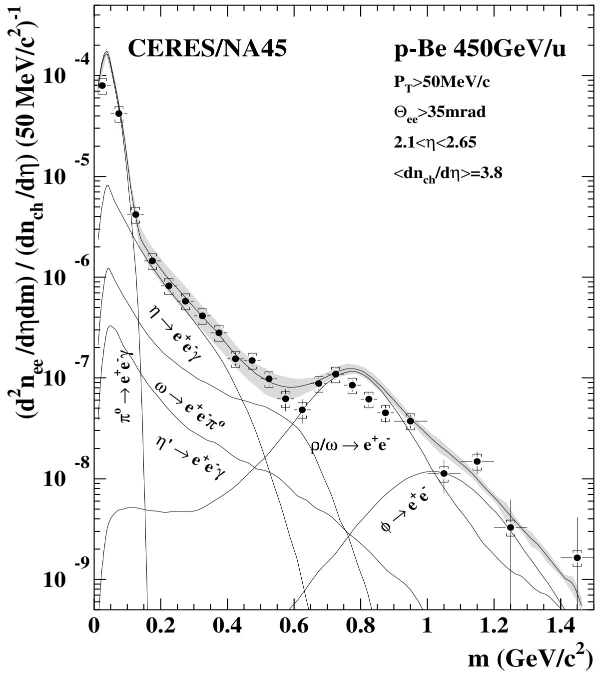

Figure 5.6: The final p-Be mass spectrum with statistical and systematical errors, for a signal to background of 0.45.

knowledge of the η branching ratio into $e^+e^-\gamma$. This method is based on a direct normalization of the π^0 and η exclusive yields in the event generator according to the $\pi^0, \eta \to e^+e^-\gamma$ yield as reconstructed in the CERES-TAPS coincidence measurements: $2,366 \pm 461$ η Dalitz decays and $3,011 \pm 241$ π^0 Dalitz decays[2] [81]. After taking into account the photon acceptance and reconstruction efficiency the inclusive yields of e^+e^- pairs from the η and π^0 Dalitz decays are $23,743 \pm 4,626$ and $47,849 \pm 3,830$ respectively[2]. The other hadronic processes are normalized with respect to the η using the same ratios as in the previous method. Instead of the $\sim 30\%$ error in the mass range $0.2 - 0.6$GeV/c^2 as mentioned above, the error now is dominated by the precision in the $\eta \to e^+e^-\gamma$ measurement, mainly limited by the reconstruction efficiency of the associated photon, resulting in a total error of $\sim 19\%$. Another advantage of this normalization method is that all the systematic errors in the data drop. However, this method introduces larger errors above the η region, since the yield of the relevant particles (ρ^0, ω and ϕ) is derived from the η yield and the η branching ratio error enters there. Therefore, the overall error at masses $m > 0.6$GeV/c^2 is about 37%. A preliminary comparison between the event generator and the p-Be data, of $S/B = 0.45$ using this normalization scheme is shown in Figure 5.7. Note, that the vertical scale represents now the raw yield i.e. the measured e^+e^- pairs per 50MeV/c^2 mass bins. With both normalization methods, the data are well reproduced by the hadronic cocktail as can be seen in Figures 5.5 and 5.6 and there is no need to invoke any source of anomalous pairs production. This statement will be quantified in Section 5.6 after a detailed error analysis.

5.5 p-Au Mass Spectrum

The 1993 p-Au mass spectrum is given in Figure 5.8. The data normalization is done according to the first method discussed in Section 5.4. Although this mass spectrum suffers from lower statistics, it appears that, as in the p-Be data, there is an agreement between the data and the event generator indicating that no new unconventional sources should be invoked in order to explain also the p-Au mass spectrum. A remarkable different mass spectrum however is observed in the S-Au collisions as will be discussed later, see Figure 5.16.

---

[2] The errors represent statistical and systematic.

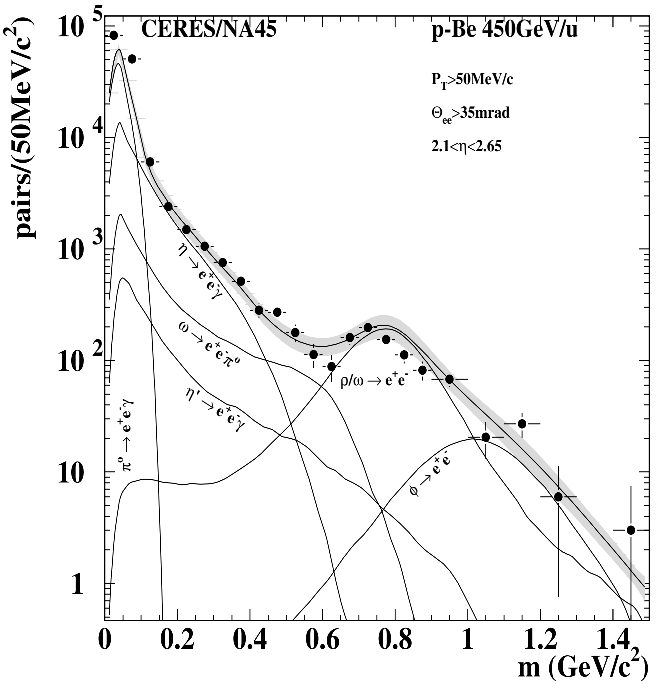

Figure 5.7: A preliminary comparison between the event generator and the p-Be data ($S/B = 0.45$), using a direct normalization of the event generator based on the measured exclusive yield of π^0 and $\eta \rightarrow e^+e^-\gamma$ (see text).

5.6 Error analysis

In order to be able to derive any decisive conclusion about the existence of an anomalous e^+e^-source one should control all the error sources involved. Therefore, we invested, in the context of this work, a considerable effort in determining and minimizing these errors. The error analysis steps are sketched in Figure 5.9. The errors are divided into two major classes: errors in the event generator and errors in the data. Whereas the errors in the generator are mainly systematic, in the data we will distinguish separately the statistical and the systematical errors.

We discuss now in detail each error source separately.

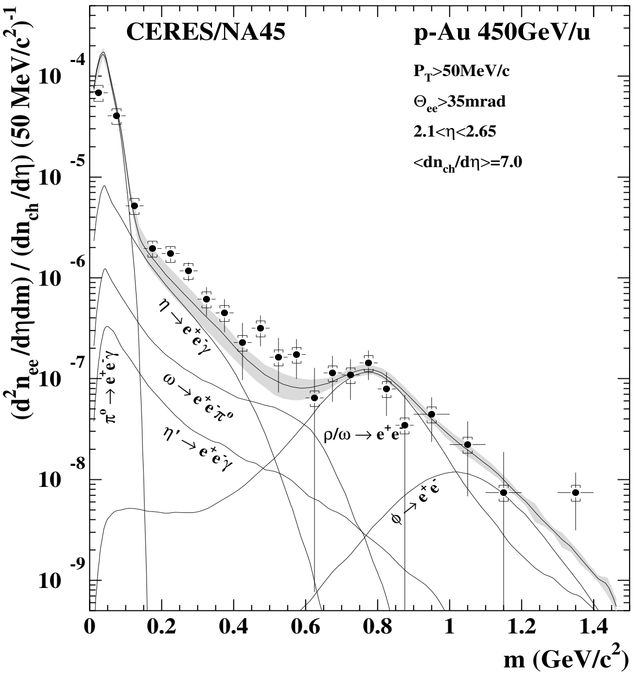

Figure 5.8: The 1993 p-Au mass spectrum.

5.6.1 Errors in the Event Generator

The sources of error in the event generator are in:
1) The parent particles cross section.
2) The branching ratios to e^+e^-.
3) The parameterizations and the form factors.
4) The $\frac{n_{\pi^0}}{n_{\mathrm{ch}}}$ ratio.
We now shall discuss each of the these error sources:

Parent particles cross section

The parent particles cross section and their associated errors are taken from the TAPS measurements; these numbers are quoted in Table 4.1 and discussed in Section 5.4.

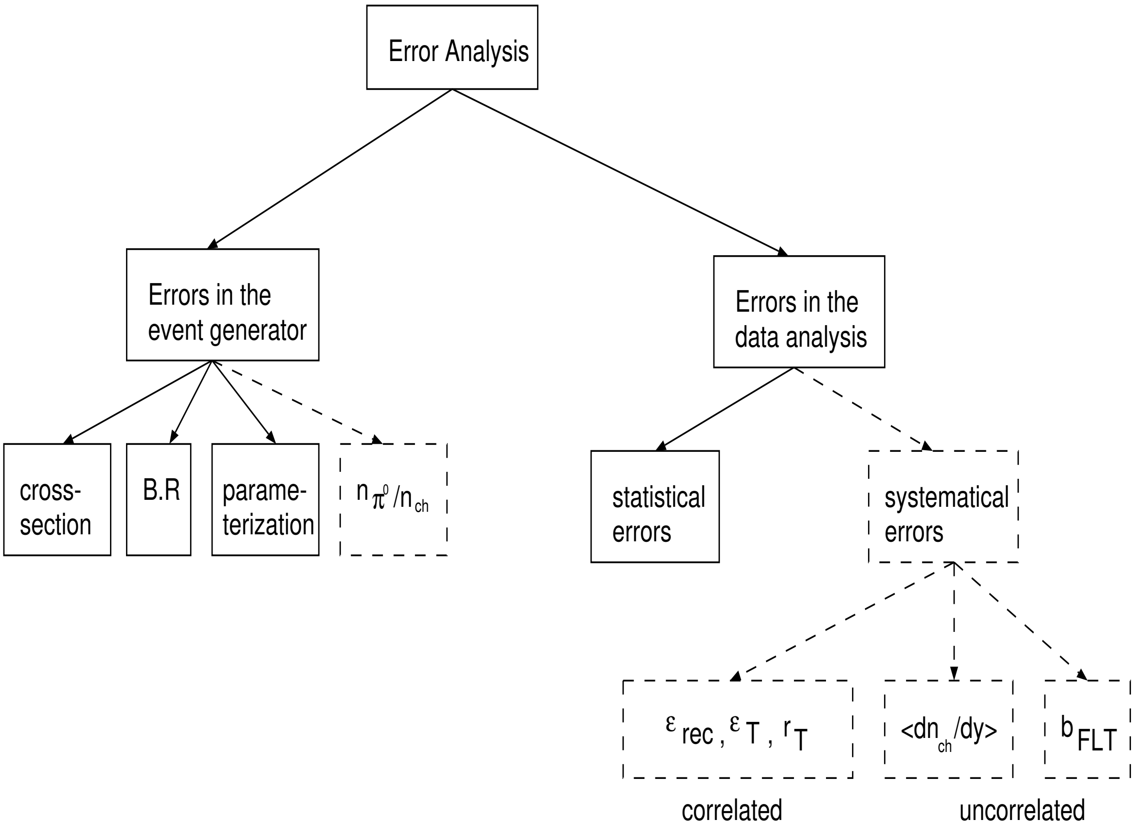

Figure 5.9: Error analysis hierarchy. Dashed lines represent errors that belong only to normalization method a) whereas solid lines represent errors in the two methods of normalization a) and b).

Branching ratio

The branching ratios into e^+e^-or $e^+e^-\gamma$ and their errors are quoted in Table 4.1.

Parameterization and form factor

The p$_T$ and y of the parent particles are taken from the modified B-G parameterization discussed in Section 4.3. This parameterization reproduces fairly well experimental p$_T$ and y distributions measured in a variety of systems (NA23 π^0, NA27 π^0 and $\pi^\pm$, NA34 ρ^0/ω and other nucleus-nucleus experiments, see [67] for further details) and this actually puts severe constrains in the coefficients of the parameterization. The systematical errors introduced by the parameterization in the invariant mass spectrum was established to be $\sim 4\%$ by varying the coefficients within reasonable limits, i.e. keeping a reasonable reproduction of the experimental data.

As discussed in Section 1.4, the measured form factors of the η and the $\eta\prime$ are in good agreement with the VDM; however the measured ω form factor is clearly enhanced with respect to the VDM prediction. In our event generator we have consistently used the measured data. The resulting poles and errors are quoted in Table 4.3.

As discussed in Section 4.2.1, the HELIOS data favors a 2 radian ρ^0/ω interference with a very large uncertainty ($\alpha = 2.0 \pm 1.2$ rad.). This interference reduces the yield at the ρ^0/ω region by about 10%. Also the ρ^0 polarization is not known and it is an additional source of a systematic error. Our working assumption is that it is not polarized, but full polarization will decrease the yield up to 20%.

The $\frac{n_{\pi^0}}{n_{\mathrm{ch}}}$ ratio

The value for $\frac{n_{\pi^0}}{n_{\mathrm{ch}}}|_{y=0}$ and its associated error were discussed in Section 4.5.

5.6.2 Errors in the data

The errors associated to the data points are divided into statistical and systematical errors.

Statistical errors:

The statistical error is calculated by: $\Delta S = \sqrt{U + L}$, see Section 3.3.8. Its size depends on the initial sample size and then also on the cuts applied to the data, i.e.

on the S/B level, see Table 3.3. The analyzed mass spectrum with a $S/B = 0.45$ is shown as a table for each of its 30 mass bins (using a bin width of 50MeV/c^2) in Table 5.1.

Systematical errors:

The systematical errors are subdivided into uncorrelated errors and correlated ones, where in this case the correlation must not be ignored, otherwise, the global error would turn out to be incorrect.

Correlated errors

Some of the factors that participate in the data normalization are correlated and therefore their error should not be considered independently, but rather it has to be evaluated in a global manner. For example, the pair reconstruction efficiency ϵ_{rec}, the efficiency ϵ_T and the rejection r_T of the trigger mainly depend on the UV-1 detector gain . The ILT+SLT trigger efficiency, ϵ_T, as a function of the UV-1 detector gain was studied using MC pairs and the trigger emulator. As expected, the efficiency increases with the gain as shown in Figure 5.10. The rejection factor of the trigger, r_T, on the other hand, decreases with the gain. This dependence was determined from the on-line rejection information and the corresponding gain of each run as was found in the off-line analysis and it is shown in Figure 5.11.

The pair reconstruction efficiency as a function of UV-1 gain is obtained using MC pairs overlay on FLT data and the ILT/SLT trigger emulator as explained in Section 5.2. The results are shown in Figure 5.12. The overall product of $A = r_T \cdot \epsilon_T \cdot \epsilon_{rec}$ versus the gain is finally shown in Figure 5.13. If one were to consider those three factors independently, the joint error would be given by:

$$\frac{\Delta A}{A} = \sqrt{\left(\frac{\Delta r_T}{r_T} \right)^2 + \left(\frac{\Delta \epsilon_T}{\epsilon_T} \right)^2 + \left(\frac{\Delta \epsilon_{rec}}{\epsilon_{rec}} \right)^2}$$

and this would result in a total error of 17%. On the other hand, our global treatment, by taking into account the gain correlation, gives an error of about 6%. This is obtained by reading the ordinate variation corresponding to $\pm 1\sigma$ variation (which is about $\pm 13\%$) around the average UV-1 gain in the abscissa.

Non-correlated errors

Other factors that participate in the data normalization are: $< dn_{ch}/dy >$ and b$_{FLT}$:

mass bin (MeV/c^2)	unlike pairs $U = e^+e^-$	like pairs $L = e^+e^+ + e^-e^-$	signal $S = U - L$	statistical error
25	87046	4693	82353.	302.9
75	56765	6125	50640.	250.8
125	12837	6805	6032.	140.2
175	7576	5179	2397.	112.9
225	5264	3768	1496.	95.0
275	3575	2520	1055.	78.1
325	2550	1795	755.	65.9
375	1641	1129	512.	52.6
425	1078	795	283.	43.3
475	814	543	271.	36.8
525	585	407	178.	31.5
575	447	334	113.	28.0
625	340	252	88.	24.3
675	337	177	160.	22.7
725	335	137	198.	21.7
775	275	121	154.	19.9
825	216	104	112.	17.9
875	168	86	82.	15.9
925	142	73	69.	14.7
975	126	59	67.	13.6
1025	73	40	33.	10.6
1075	60	52	8.	10.6
1125	76	40	36.	10.8
1175	44	26	18.	8.4
1225	30	28	2.	7.6
1275	31	21	10.	7.2
1325	27	23	4.	7.1
1375	17	24	−7.	6.4
1425	24	28	−4.	7.2
1475	20	10	10.	5.9

Table 5.1: The unlike and the like sign pairs sample together with the signal and statistical error for the $S/B = 0.45$ p-Be data.

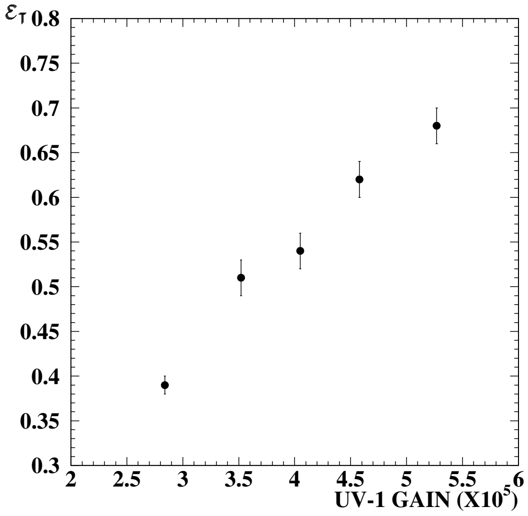

Figure 5.10: The ILT+SLT trigger efficiency as a function of UV-1 gain.

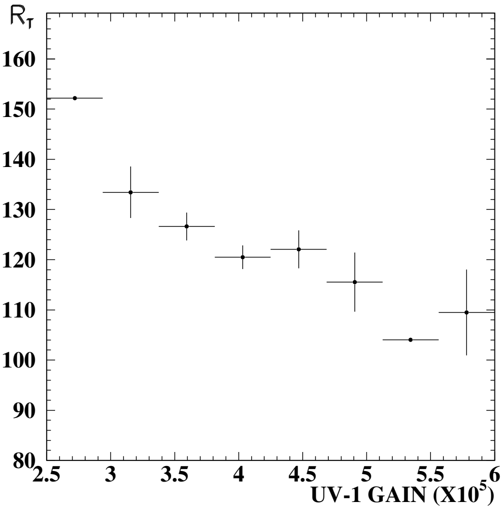

Figure 5.11: Trigger rejection dependence on the gain.

- $< dn_{ch}/dy >$ was discussed in Section 5.3 and its error was estimated to be $\sim 5\%$.
- The b_{FLT} and its error were discussed in Section 3.1.3, see Figure 3.2, $b_{FLT} = 2.42 \pm 0.25$.

5.6.3 Summary and discussion

The systematical errors in the event generator and the data for two representative mass points at $m = 300$ and 800MeV/c^2 are summarized in Table 5.2. The first mass point belongs to the mass region of interest where anomalous pair production has been reported. The yield at $m = 300$MeV/c^2 is dominated by the contribution from the η Dalitz decay. We therefore consider only the errors associated to the η in our estimation of the event generator sources of error in this mass range. The yield at $m = 800$MeV/c^2 comes primarily from the ρ^0 and ω resonance decays. For the event generator we quote here the weighted error of the product$(d\sigma/dy) \cdot \mathrm{BR}$ of these two contributions in Table 5.2. The individual errors are added quadratically to derive a total systematical error in the event generator and the data.

The various systematical errors in the data are quoted in Table 5.2. The over-

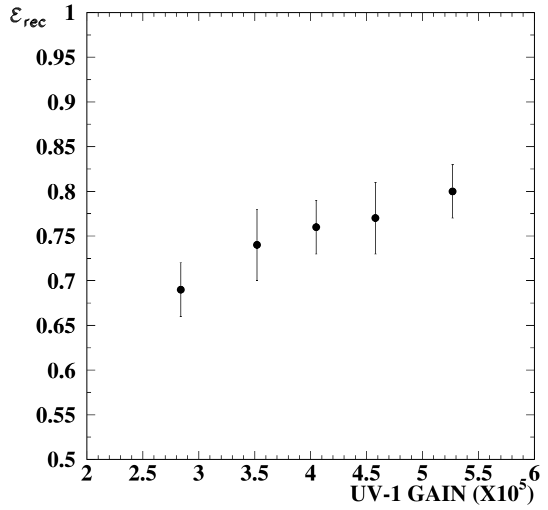

Figure 5.12: ϵ_{rec} versus RICH-1 gain.

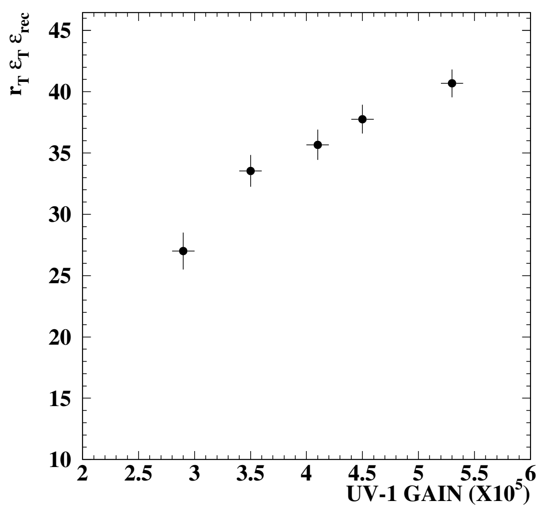

Figure 5.13: $A = r_T \cdot \epsilon_T \cdot \epsilon_{rec}$ versus RICH-1 gain.

all error (derived from their quadratic sum) is also quoted and amount to $\pm 13\%$. These errors are independent of the pair mass, and they count only in the normalization method a). Method b) provides the highest accuracy (total systematical error of 20%) for $200 < m < 600$MeV/c^2. The data are free from systematical errors and the direct determination of the η yield from the coincidence data of $e^+e^-\gamma$ has reduced the systematical errors in the event generator. On the other hand at higher masses method a) give the highest accuracy 11% and 13% systematic errors in the event generator and data respectively. However, ρ^0/ω interference and vector meson polarization were not implemented in the event generator because there is not enough experimental information for a realistic assessment of these quantities. To properly address them it is necessary to have a very good mass resolution allowing to disentangle the contribution of each of the vector mesons separately. The CERES spectrometer is not suited for that since it was designed to be a relatively low-cost spectrometer at the expenses of a very moderate mass resolution. In spirit of that the results shown in Figures 5.5 and 5.6 (the measured yield is lower than the expected one at $m \simeq 800$MeV/c^2) together with the discussions in Section 4.2 favor destructive interference between the ρ^0 and the ω mesons or some polarization in their production (or a combination of the two).

	m = 300MeV/c^2		**m = 800MeV/c^2**	
	method a (%)	**method b (%)**	**method a (%)**	**method b (%)**
event generator				
$(d\sigma/dy)$	16	19	10	36
BR	24			
π^0/n_{ch}	4	-	4	-
paramet.	4	4	4	4
Total	**29**	**20**	**11**	**37**
data				
$r_T \cdot \epsilon_T \cdot \epsilon_{rec}$	6	-	6	-
dn_{ch}/dy	5	-	5	-
b_{FLT}	10	-	10	-
Total	**13**	-	**13**	-

Table 5.2: Systematic errors summary in the event generator and in the data for two representative mass points.

5.7 p_T and rapidity distributions

In Figure 5.14 a comparison between the p_T and y distributions of the e^+e^-pairs from the p-Be analyzed data and the Monte-Carlo event generator is shown. In both plots of Figure 5.14 a p_T cut of 50MeV/c was applied to the electron tracks, an angular cut of 35mrad was applied to the pair opening angle and we required pair mass greater than 200MeV/c^2. There is a reasonable agreement between the data and the event generator in the p_T and rapidity distributions. The only discrepancy occurs at the first bin in the p_T distribution. This is due to the low track efficiency at low p_T, which was not corrected in the event generator.

5.8 Summary and outlook

The major goal of the present work is to clarify the long standing problem of the excess in the low-mass pair production ($200 \leq m \leq 600$MeV/c^2) that was claimed by several groups over the last two decades. The source of the anomalous mass spectrum was not understood and several new physics mechanisms were proposed in order to explain it. The direct measurement, within the same experimental setup,

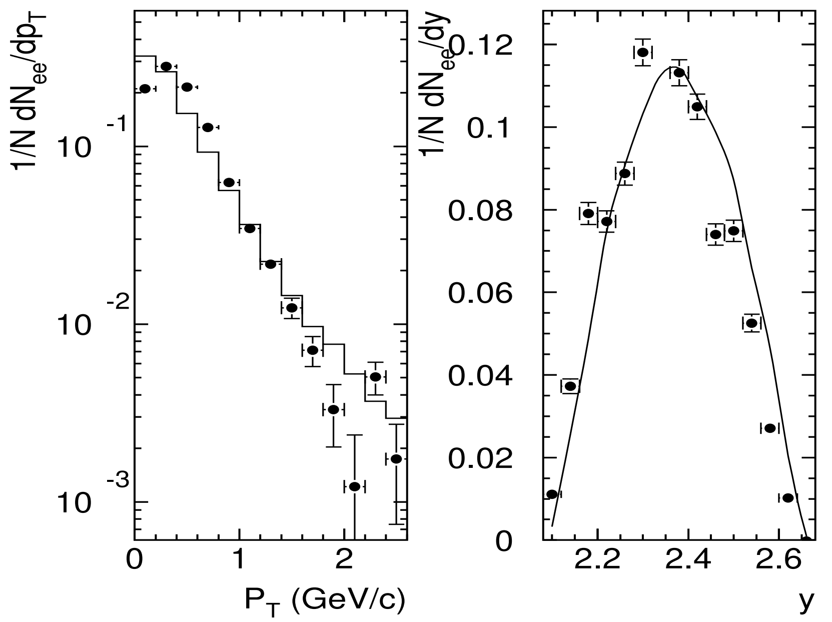

Figure 5.14: p_T (left) and rapidity (right) for pairs with $m > 200\text{MeV/c}^2$, single track $p_T > 50\text{MeV/c}$ and pair opening angle cut $\theta > 35\text{mrad}$. The histogram is the modified B-G simulation.

of the relative production cross section of the π^0, η and ω mesons, which are the main sources of hadron decays in the inclusive low-mass spectrum, has allowed us to achieve the highest accuracy of all previous measurements of inclusive e^+e^-pairs in the mass range $200 \leq m \leq 600\text{MeV/c}^2$ in p-Be (a very good approximation to p-p) collisions. Using a direct normalization of the yields (referred to as normalization method b) we achieve a total systematical error of 20% in this mass range. The statistical error of the integrated yield in this mass range is negligible.

Within these errors there is very good agreement between the measured invariant mass spectrum and the expected one from known hadronic sources (hadronic cocktail). Therefore, there is no need to invoke any new or "anomalous" source. This result confirms the recent HELIOS/NA34-1 measurement [43] of e^+e^-pairs in 450GeV/c p-Be collisions, but with much larger error, although with a better mass resolution, as seen in Figure 5.15.

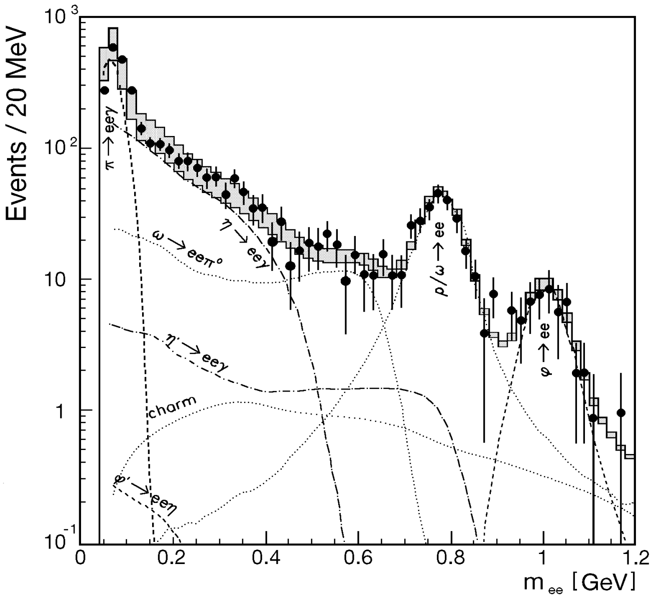

Figure 5.15: HELIOS/1 measurement of e^+e^- mass spectrum in 450GeV/c p-Be reaction.

A good agreement is also found using an absolute normalization of the data (referred to as normalization method a). However, the total systematical error is now 29%, dominated by the 24% error in the $\eta \rightarrow e^+e^-\gamma$ branching ratio.

The mass range $0.6 \leq m \leq 1.4$GeV/c^2 dominated by the resonance decays $\rho^0, \omega, \phi \rightarrow e^+e^-$ is also well reproduced by the hadronic cocktail. The best accuracy is achieved here with normalization method a), with a total systematical error of 11%, whereas with normalization method b) the total error is 37% (dominated by the error in the event generator cross sections, and in particular the error in the $\eta \rightarrow e^+e^-\gamma$ branching ratio, see Section 5.4). These errors do not include the uncertainties originating from ρ^0/ω interference and polarization of the produced vector mesons.

The e^+e^-invariant mass spectrum measured in p-Au collisions is also well described by the hadronic cocktail (however due to the lower statistics the error is somewhat larger). This is not a trivial statement since in the p-Au case the incident proton can interact with several target nucleons, whereas the p-Be case is a very good approximation to a p-p system.

The present p-Be and p-Au results have also provided a solid reference basis for the measurements of low-mass pairs in nuclear collisions. They have allowed to identify a striking effect in the 200GeV/u S-Au data, see Figure 5.16. The S-Au mass spectrum shows a different shape and a strong enhancement in the mass region $m > 0.2$GeV/c^2 of a factor of $5.0 \pm 0.7_{\mathrm{stat}} \pm 2.0_{\mathrm{sys}}$ over the hadronic sources. The onset of the excess starting at a mass of $\sim 2m_\pi$, together with a possible quadratic dependence on the event multiplicity, suggest the opening of the $\pi^+\pi^- \rightarrow e^+e^-$ annihilation channel. This would be the first observation of thermal radiation from dense hadronic matter [82, 83]. The addition of the $\pi^+\pi^-$ annihilation channel to the hadronic cocktail accounts for a sizable fraction of the observed excess [84, 85]. An excellent reproduction of the excess is achieved if one includes also the effects of dropping masses, in particular of the ρ^0 meson, as a precursor of chiral symmetry restoration [14]. However, the experimental errors are too large to convincingly rule out more conventional results.

Last year CERES took data of 160GeV/u Pb-Au collisions. A preliminary Pb-Au mass spectrum, presented at Quark-Matter '96, is shown in Figure 5.17. This mass spectrum seems to be consistent with the previous S-Au results and it also exhibits an enhancement in the same mass range. At the end of 1996 CERES will have a relatively longer run of 40 days of Pb-Au data. This will enable a collection of a larger data sample and a precise measurement of the enhancement observed so far, providing also additional information on the excess, in particular its multiplicity dependence and p$_T$ distribution.

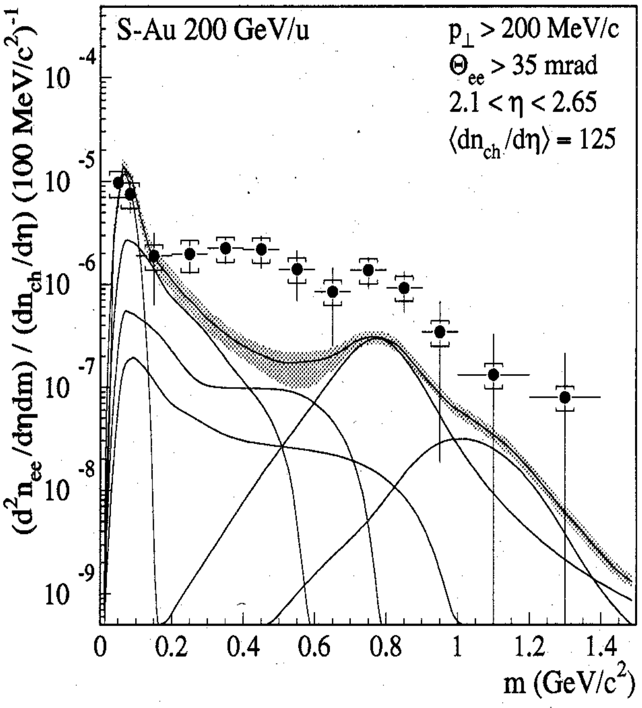

Figure 5.16: The S-Au mass spectrum.

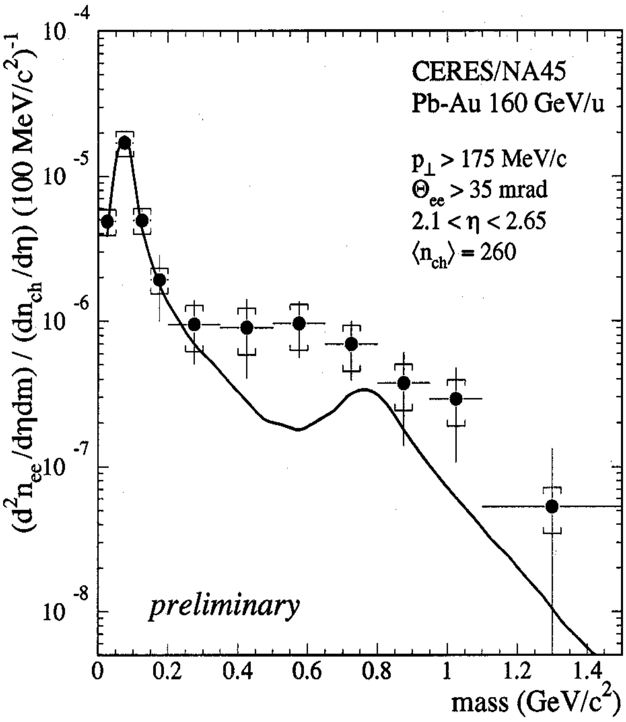

Figure 5.17: A preliminary Pb-Au mass spectrum.

Appendices

Appendix A

Some kinematic variables

A particle of mass m and a momentum $\vec{p} = (p_x, p_y, p_z)$ has a transverse mass, m_T, defined by:

$$m_T = \sqrt{m^2 + p_T^2} \tag{A.1}$$

where,

$$p_T = \sqrt{p_x^2 + p_y^2} \tag{A.2}$$

is the transverse momentum (the longitudinal momentum p_z is also denoted by p_L.). The particle energy is given by:

$$E = \sqrt{m^2 + |p|^2} \tag{A.3}$$

The rapidity is then defined:

$$y = \tfrac{1}{2} \ln \left(\tfrac{E+p_z}{E-p_z} \right) = \ln \left(\tfrac{E+p_z}{m_T} \right) \tag{A.4}$$

The following relations hold between (E, p_z) and (m_T, y):

$$E = m_T \cosh y \ , \qquad p_z = m_T \sinh y \tag{A.5}$$

The rapidity can also be written as:

$$y = \tanh^{-1} \left(\tfrac{p_z}{E} \right) \tag{A.6}$$

Let us denote by θ the particle polar angle, that is the angle between the z-axis and $\vec{p}$, then uppon expanding Equation A.4 in θ one gets:

$$y = \frac{1}{2} \ln \frac{\cos^2(\theta/2) + m^2/4p^2 + \cdots}{\sin^2(\theta/2) + m^2/4p^2 + \cdots} \simeq -\ln \tan(\theta/2) \equiv \eta \tag{A.7}$$

where η is the pseudorapidity. The pseudorapidity is approximately equal to the rapidity for relativistic particles ($|p| >> m$).

Appendix B

Basic Cherenkov radiation formulae

A charged particle moving with a velocity $v = \beta c$ in a medium with a refractive index n will emit Cherenkov radiation if v exceeds the velocity of light in the medium.

The polar emission angle θ relative to the particle direction is given by:

$$\cos\theta = \frac{1}{n\beta} \tag{B.1}$$

whereas, the azimuthal emission angle ϕ has a flat distribution between 0 and 2π.

Radiation will be emitted only if $v > c/n$ ($\cos\theta \leq 1$), therefore:

$$\beta \geq \beta_{\mathrm{th}} = \frac{1}{n} \tag{B.2}$$

where β_{th} is a threshold velocity. The corresponding expression for the Lorentz factor at the threshold speed is:

$$\gamma_{\mathrm{th}} = \frac{n}{\sqrt{n^2 - 1}} \tag{B.3}$$

The threshold momentum depends on the particle mass and on the medium index of refraction:

$$p_{\mathrm{th}} = m\gamma_{\mathrm{th}}\beta_{\mathrm{th}} = \frac{m}{\sqrt{n^2 - 1}} \tag{B.4}$$

The Cherenkov angle for ultra-relativistic particles, $\beta \simeq 1$ is given by:

$$\cos\theta = \frac{1}{n} = \frac{\sqrt{\gamma_{\mathrm{th}}^2 - 1}}{\gamma_{\mathrm{th}}^2} \tag{B.5}$$

For small angles,

$$\sin\theta \simeq \theta \simeq \frac{1}{\gamma_{\rm th}} \tag{B.6}$$

In the present experiment, the particle identification is done using RICH (Ring Imaging CHerehkov) detectors where Cherenkov light is imaged into rings. The ring image formation principle in a RICH detector is shown schematically in Figure B.1.

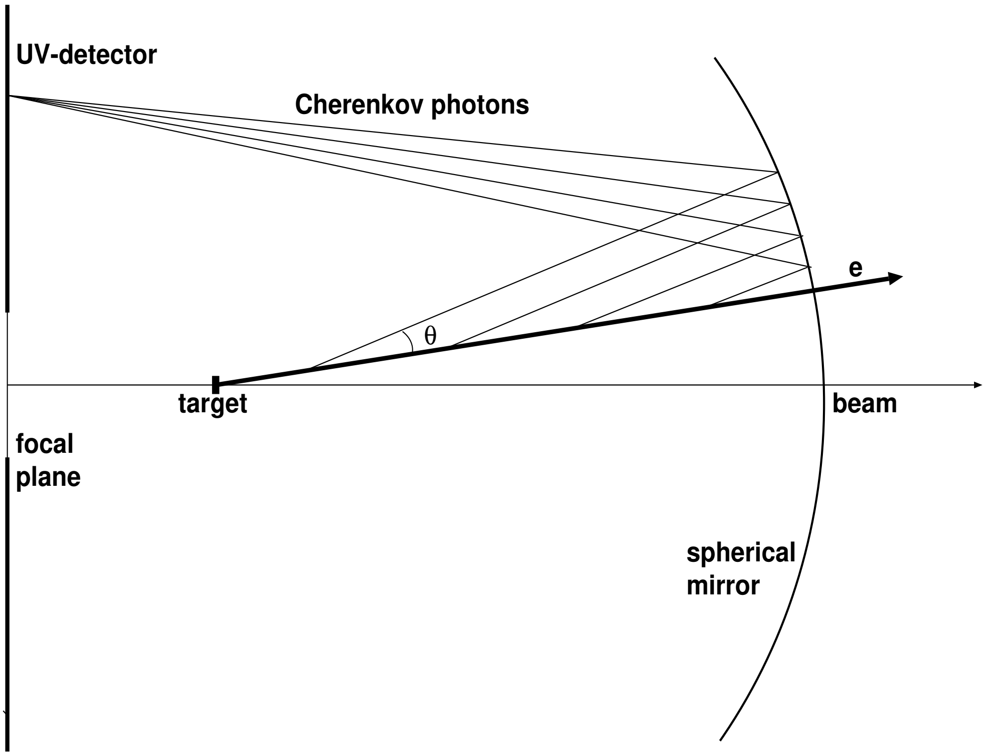

Figure B.1: A schematic view of a Cherenkov ring image formation.

The ring radius is given by:

$$R = f\tan\theta \tag{B.7}$$

where f is the mirror focal length. For ultra relativistic particles this radius is fixed and known in advance and it is called the asymptotic radius, R_∞. In addition, for small Cherenkov angles, the asymptotic radius is approximated by:

$$R_\infty \simeq f\theta \simeq \frac{f}{\gamma_{\rm th}} \tag{B.8}$$

In order to discriminate between electron rings and other charged particles rings, in particular pions, it is important to check the fraction of the asymptotic radius that pions reach as a function of their momentum. Substituting θ in Equation B.7 by n and β, from Equation B.1 one gets,

$$R = f\sqrt{\beta^2 n^2 - 1} \;\; ; \quad R_\infty = f\sqrt{n^2 - 1} \tag{B.9}$$

therefore,

$$\frac{R}{R_\infty} = \sqrt{\frac{\beta^2 - \beta_{th}^2}{1 - \beta_{th}^2}} \tag{B.10}$$

where in Equation B.10 n was replaced by $1/\beta_{th}$. Using the relation between β and γ, Equation B.10 is re-written:

$$\frac{R}{R_\infty} = \sqrt{1 - \frac{\gamma_{th}^2}{\gamma^2}} \tag{B.11}$$

Upon replacing $\gamma = \sqrt{p^2 + m^2}/m$:

$$\frac{R}{R_\infty} = \sqrt{1 - \gamma_{th}^2 \frac{m^2}{p^2 + m^2}} \tag{B.12}$$

A plot of Equation B.11 for electron, muon and pion is shown in Figure B.2. For $\gamma_{th} \simeq 32$ the momentum threshold for Cherenkov light emission by pion is $p > 4.5$GeV/c. Therefore, most of the pions will not produce Cherenkov light and thus the spectrometer is "hadron blind". In addition, pions will produce rings with radius $> 95\%$ of the asymptotic ring radius for $p > 14.3$GeV/c, this means that only the very small fraction of energetic pions will produce Cherenkov rings which resemble electron rings.

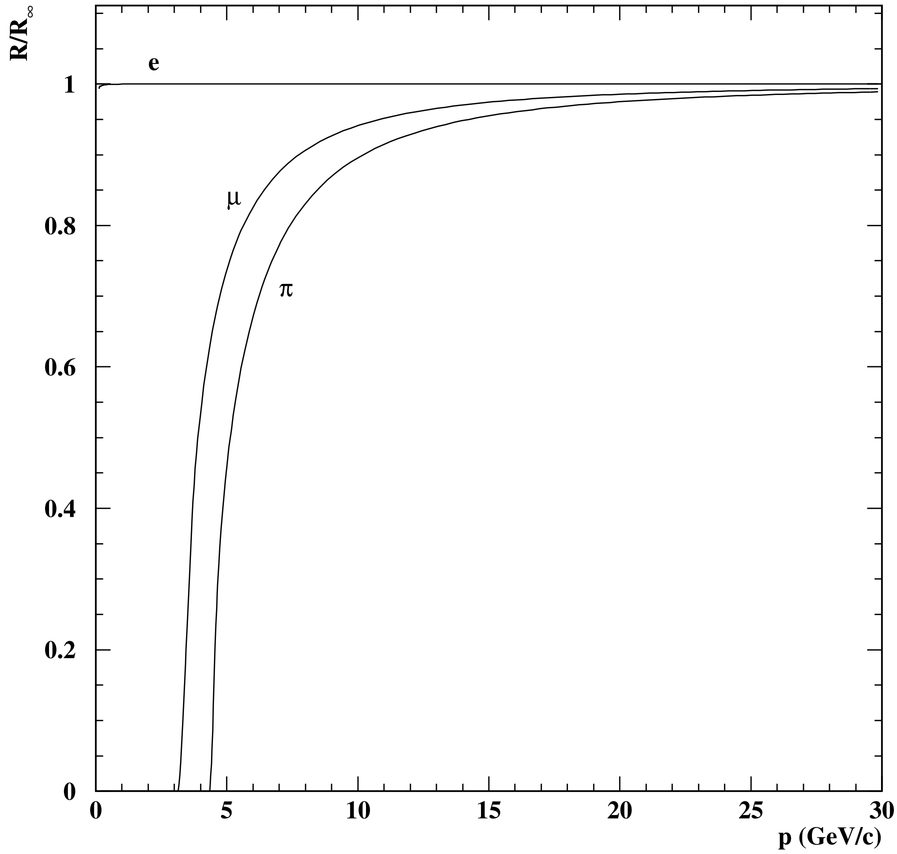

Figure B.2: Cherenkov ring radius for electron, muon and pion as a function of the particle's momentum (normalized to the asymptotic radius).

Appendix C

Hardware and Software resources

The the 1993 p data analysis and simulations were completely performed at the Weizmann Institute of Science (WIS). The analysis took place in two steps: First, the data was compressed by a factor of ~ 10 by requiring at least one pair per event. Then, DSTs in a form of "ntuples" were produced for each run and finally merged into a single file. The final merged ntuple size is about 1.1GB.

C.1 Hardware

The available hardware resources for the p analysis were 4 Unix HP workstations and about 5GB of disk space. The disks were fed with raw data from 8mm$\times$112m exabyte tapes. A total of about 120GB of p-Be raw data were processed. The hardware configuration for this analysis is shown schematically in Figure C.1.

C.2 Software

There are 3 main software packages (all of them written in FORTRAN-77) for the p data analysis:

- The main analysis program reads raw data (or simulated data) and generates compressed DST files (ntuples), where only events containing at least one pair with p_T above 50MeV/c are kept. The analysis program can be connected to a trigger emulator software in order to study trigger efficiency.

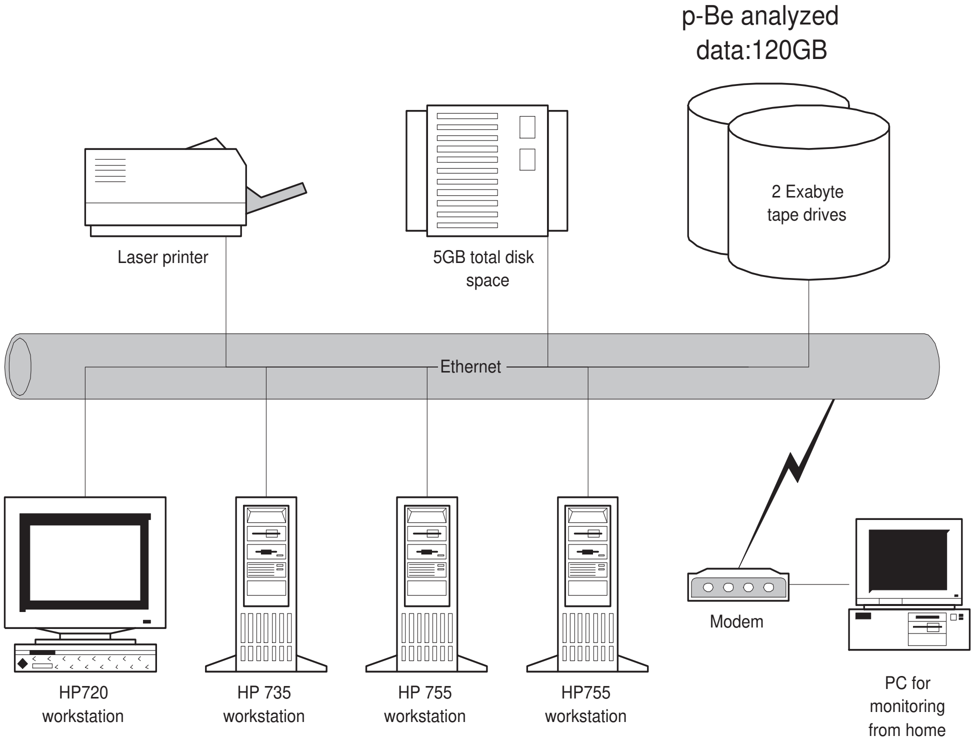

Figure C.1: Computing environment for the 1993 p run off-line analysis.

- The event generator which generates 2 electrons in the CERES acceptance in a form of 2 four-vectors. This data is read by the main analysis program.
- Spectrometer simulation software which is called by the main analysis program and produces electron rings on the UV-detectors from the event generator pairs.

The ntuple itself was later processed using PAW[1] (Physics Analysis Workstation) by executing KUIP macros which call COMIS (a Fortran interpreter) routines. Several short routines were written in C and as Unix scripts in order to operate and monitor the analysis. A TCL/TK graphical user interface (GUI) was used for interactive operation and monitoring of the analysis processes on the different workstations.

---

[1] Online documentation on the World-Wide Web is available at URL: *http://wwwcn1.cern.ch/asd/paw/index.html.*

The analysis and the two MC simulation programs were completely written at the WIS. In addition, important routines in the general CERES library, CARMEN (e.g. event cleanup, pad clusters, photon hits, ring candidates etc.), were also written at the WIS. The I/O library, CECILIA, parts of CARMEN and the trigger emulator were written by the CERES group at the Heidelberg university, Germany.

Most of the figures were produced using CERN's HBOOK/HPLOT for histogramed data. Some of the drawings were produced by 'tgif' and VISIO 3 on a PC. Other images were scanned by an HP ScanJet 3C scanner. All the figures were finally kept in encapsulated Postscript format. This document was prepared with LaTeX2ϵ, spelling was checked with 'ispell'. The hebrew abstract was written using Microsoft WORD 6. MATHEMATICA 2.0 was used for the preparation of Figure 4.2. An extensive usage of the World-Wide Web (WWW) was done in this research for obtaining papers, e.g. 'hep-ph' preprints and other relevant information.

Appendix D

The CERES/NA45 collaboration members in 1993

- **Brookhaven National Laboratory,**
  Upton, NY 11973, USA
  P. Rehak.

- **CERN, 1211 Geneva 23, Switzerland**
  J. Schukraft.

- **JINR, Dubna, Russia**
  G. Agakichiev, Y. Minaev, Y. Panebrattsev, S. Razin, S. Shimansky.
- **Max-Planck-Institut für Kernphysik,**
  69117 Heidelberg, Germany
  U. Faschingbauer, F. Hess, C. Jacob and J. P. Wurm.

- **Physikalisches Institut der Universität Heidelberg,**
  69120 Heidelberg, Germany
  R. Baur, A. Drees, P. Fischer, J. Frieben, P. Glässel, Th. Günzel, D. Irmscher, R. Männer (Mannheim Univ.), L. H. Olsen, A. Pfeiffer, A. Schön, H. J. Specht, S. Tapprogge, Th. Ullrich.
- **Politecnico di Milano,**
  20133 Milano, Italy

E. Gatti, A. Longini and M. Sampietro.

- **The Weizmann Institute of Science,**
  76100 Rehovot, Israel
  Z. Fraenkel, C. de Los Heros, I. Ravinovich, V. Steiner, G. Tel-Zur and I. Tserruya (Spokesman).

Members of the TAPS Collaboration

- **Giessen University,**
  D-35392 Giessen, Germany
  M. Appenheimer, A. Brenschede, M. Franke, W Kühn, V. Metag, M. Notheisen, R. Novotny and H Stroeher.

- **Gronigen KVI,**
  Gronigen, The Netherlands
  H. Löhner, J. van Pol and H. Wilschut.

- **Dramstadt GSI,**
  Planckstrasse 1, D-64291 Darmstadt, Germany
  R. Averbeck, R. Holzmann, A. Schubert and R.S. Simon.

- **GANIL,**
  Caen, France
  M. Marques, T. Matulewicz, R. Ostendorf and Y. Schutz.

- **Univ. Valencia,**
  Valencia, Spain
  J. Diaz, J.L. Ferrero, A. Marin, G. Martinez, J.C. Pachelo and J.A. Ruiz.

Appendix E

List of symbols

α fine structure constant.

β particle speed divided by the speed of light.

η pseudo-rapidity. also a meson: $\eta(550)$.

$\Delta\eta$ pseudo-rapidity range.

$\Delta\phi$ azimuthal deflection by the magnetic field.

ϵ_T trigger efficiency.

ϵ_{rec} pair reconstruction efficiency.

ϕ azimuthal angle. also a vector meson $\phi(1020)$.

Γ full particle width.

Γ_i partial width for a decay into channel i.

γ Lorentz factor.

γ_{th} threshold Lorentz factor for producing Cherenkov light.

Λ pole mass.

λ_I interaction length.

θ polar angle.

σ cross section.

$\sigma_{M.S.}$ r.m.s error due to multiple-scattering.

$\sigma_{d.h.r}$ double hit resolution distance.

$\sigma_{s.h.r}$ single-hit resolution.

σ_θ track match.

σ_r ring center resolution.

σ_ϕ error in the azimuthal direction.

σ_p momentum resolution.

τ life time.

Ω opening angle.

A amplitude.
B background, the number of $e^+e^+ + e^-e^-$ pairs.
BR branching ratio.
b_{FLT} First Level Trigger (FLT) bias.
c speed of light.
E energy.
E_T transverse energy.
e electron charge.
$F(q^2)$ form factor.
f focal length.
L sample size of like-sign pairs.
L length.
m mass.
m_T transverse mass.
N number of hits per ring.
N_0 spectrometer figure of merit.
n index of refraction.
n_{ch} number of charged particles.
p probability.
p momentum.
p_L longitudinal momentum.
p_T transverse momentum.
q momentum transfer.
R_{ch} Cherenkov satuated radius.
r_T trigger rejection.
S signal, the number of e^+e^- pairs minus $e^+e^+ + e^-e^-$ pairs.
s center of mass energy squared.
T temperature.
T_c phase transition critial temperature.
U sample size of unlike-sign pairs.
X_0 radiation length.
x length.
y rapidity.

Bibliography

[1] H.J. Specht. Direct photon and lepton production in high energy collisions. *Lecture Notes in Physics*, 221, 1985.

[2] H.R. Schmidt and J. Schukraft. The physics of ultra-relativistic heavy-ion collisions. *J. Mod. Phys. G*, 19:1705–1796, 1993. CERN-PPE/92-42.

[3] M. Jacob and H. Satz - Editors. Bielefeld workshop on quark matter formation and heavy ion collisions. *World Scientific, Singapore*, 1983.

[4] T. Ludlam and H.E. Wegner - Editors. 3rd int. conf. on ultra relativistic nucleus nucleus collisions. *Nucl. Phys.*, A418, 1984. Brookhaven, USA.

[5] K. Kajantie - Editor. 4th int. conf. on ultra relativistic nucleus nucleus collisions. *Lecture Note in Physics*, 221, 1985. Helsinki.

[6] S. Schroeder and M. Gyulassy - Editors. 5th int. conf. on ultra relativistic nucleus nucleus collisions. *Nucl. Phys.*, A461, 1987. Asilomar.

[7] H. Satz, H.J. Specht and R. Stock - Editors. 6th int. conf. on ultra relativistic nucleus nucleus collisions. *Z. Phys.*, C38, 1988. Nordkirchen.

[8] G. Baym, P. Braun-Munzinger and S. Nagamiya - Editors. 7th int. conf. on ultra relativistic nucleus nucleus collisions. *Nucl. Phys.*, A498, 1989. Lennox, USA.

[9] J.P. Blaizot - Editor. 8th int. conf. on ultra relativistic nucleus nucleus collisions. *Nucl. Phys.*, A525, 1991. Menton.

[10] T.C. Awes et al. - Editors. 9th int. conf. on ultra relativistic nucleus nucleus collisions. *North Holland*, 1992. Gatlingburg.

[11] E. Stenlund et al. - Editors. 10th int. conf. on ultra relativistic nucleus nucleus collisions. *Nucl. Phys.*, A566, 1994. Borlange, Sweeden.

[12] A.M. Poskanzer et al. - Editors. 11th int. conf. on ultra relativistic nucleus nucleus collisions. *Nucl. Phys.*, A590, 1995. Monterey, USA.

[13] 12th int. conf. on ultra relativistic nucleus nucleus collisions. 1996. Heidelberg, Germany. To be published.

[14] I. Tserruya. Heavy ion collisions. CERN-PPE/95-185 and Proceedings of the International Europhysics Conference on High Energy Physics, Brussels, Belgium, 1995.

[15] M. Birse and J. McGovern. Seeing the lighter side of quarks. *Physics World*, pages 35–40, October 1995.

[16] E.V. Shuryak. Quark - Gluon Plasma and hadronic production of leptons, photons and psions. *Phys. Lett. B*, 78:150, 1978.

[17] E.V. Shuryak. Quark - Gluon Plasma and hadronic production of leptons, photons and psions. *Sov. J. Nucl. Phys.*, 28:408, 1978.

[18] I. Tserruya. Summary of low-mass dilepton and direct photon results. *Nucl. Phys.*, A590:127c–138c, 1995.

[19] I. Tserruya. Ehanced dilepton production in sulphur induced reactions at 200-GeV/nucleon. *Moriond '95*, pages 559–566. Invited Talk at the 30th Rencontres De Moriond - QCD and High Energy Hadronic Interactions, Les Arcs, France, 19 - 25 March 1995. CERN-PPE/95-088.

[20] L. McLerran K. Kajantie, J. Kapusta and M. Mekjian. Dilepton emission and the QCD phase transition in ultrarelativistic nuclear collisions. *Phys. Rev. D*, 34(9):2746–2754, 1986.

[21] A. Shor. ϕ meson production as a probe of the Quark-Gluon Plasma. *Phys. Rev. Lett.*, 54(11):1122–1125, 1985.

[22] M. Herrmann et al. Properties of the ρ-meson in dense nuclear matter. *Z. Phys. A*, 343:119–120, 1992.

[23] T. Hatsuda et al. Finite temperature QCD sum rules reexamined: ρ, ω and A1 mesons. *Nucl. Phys.*, B394:221–266, 1993.

[24] R.D. Pisarski. Phenomenology of the chiral phase transition. *Phys. Lett.*, 110B(2):155–158, 1982.

[25] R.D. Pisarski. Thermal rhos in the Quark - Gluon Plasma. *HEP-PH-9503329*, 1995. Talk presented at Quark Matter '95.

[26] U. Heinz and K.S. Lee. The ρ peak in the dimuon spectrum as a clock for fireball lifetimes in relativistic nuclear collisions. *Phys. Lett*, 259B(1,2):162–168, 1991.

[27] S.D. Drell and T.M. Yan. Massive lepton pair production in hadron - hadron collisions at high-energies. *Phys. Rev. Lett.*, 25:316–320, 1970.

[28] S.D. Drell and T.M. Yan. Partons and their applications at high-energies. *Ann. Phys.*, 66:578, 1971.

[29] K.J. Anderson et al. Inclusive μ-pair production at 150 GeV by π^+ mesons and protons. *Phys. Rev. Lett.*, 37(13):799–802, 1976.

[30] J.G. Branson et al. Hadronic production of massive muon pairs: Dependence on incident-particle type and target nucleus. *Phys. Rev. Lett.*, 38(23):1334–1337, 1977.

[31] K. Bunnell et al. Production of dimuons in 16-GeV/c πp interactions and the observation of a low-mass continuum of unfamiliar origin. *Phys. Rev. Lett.*, 40(3):136–139, 1978.

[32] B. Haber et al. Dimuon production in 15.5-GeV/c πp interactions and the observation of a low-mass continuum. *Phys. Rev. D*, 22(9):2107–2121, 1980.

[33] J. Ballam et al. Direct electron-pair production in $\pi^{\pm}p$ interactions at 18 GeV/c. *Phys. Rev. Lett.*, 41(18):1207–1210, 1978.

[34] A.G. Clark et al. Electron pair production at the CERN ISR. *Nucl. Phys.*, B142:29–52, 1978.

[35] A. Chilingarov et al. Production of high transverse momentum low-mass electron-poistron pairs in high-energy collisions. *Nucl. Phys.*, B151:29–45, 1979.

[36] R. Stroynowski et al. Observation of a direct low-mass e^+e^- continuum in π^-p interactions at 16 GeV/c. *Phys. Lett.*, 97B(2):315–319, 1980.

[37] D. Blockus et al. Direct electron pair production in π^-p interactions at 16 GeV/c and a model for direct lepton and photon production at low p$_T$. *Nucl. Phys.*, B201:205–249, 1982.

[38] S. Mikamo et al. Production of direct e^+e^- pairs in proton-nucleus collisions at 13 GeV/c. *Phys. Lett.*, 106B(5):428–432, 1981.

[39] J. Stekas et al. Low-mass electron-pair anomaly in 17-GeV/c π^-p collisions. *Phys. Rev. Lett.*, 47(24):1686–1689, 1981.

[40] M.R. Adams et al. Anomalous electron-pair production in 17-GeV/c π^-p collisions. *Phys. Rev. D*, 27(9):1977–1998, 1983.

[41] V. Cerny et al. Comparison of the soft annihilation model of the low mass dilepton production with the data. *Phys. Rev. D*, 24:652–661, 1981.

[42] J.D. Bjorken and H. Weisberg. Direct lepton production and the Drell-Yan mechanism. *Phys. Rev. D*, 13(5):1405–1408, 1976.

[43] T. Åkesson et al. Low-mass lepton-pair production in p-Be collisions at 450 GeV/c. *Z. Phys. C*, 68:47–64, 1995. CERN-PPE/94-140.

[44] D.H. Perkins. *Introduction to High Energy Physics*. Addison-Wesley Publishing, Inc., third edition, 1987.

[45] J.J. Sakurai. Theory of strong interactions. *Ann. Phys. (NY)*, 11:1–48, 1960.

[46] D.R. Yennie T.H. Bauer, R.D. Spital and F.M. Pipkin. *Rev. Mod. Phys.*, 50(2), 1978.

[47] R.I. Dzhelyadin et al. Study of the electromagnetic transition form-factor in $\omega \to \pi^0\mu^+\mu^-$ decay. *Phys. Lett.*, 102B(4):296–298, 1981.

[48] L.G. Landsberg. Electromagnetic decays of light mesons. *Phys. Rep.*, 128(6):301–376, 1985.

[49] The CERES/NA45 Collaboration. *Addendum II to proposal SPSC/P237*, August 1992. CERN/SPSLC 92-48. SPSLC/P237 Add2.

[50] L. Carroll. *Alice advantures in the wonderland.* Oxford university press edition.

[51] V. Steiner. *The CERES spectrometer for the measurement of electron-positron pairs in relativistic hadron collisions.* PhD thesis, Weizmann Institute of Science, Rehovot, Israel, 1993.

[52] R. Baur et al. The pad readout of the CERES RICH detectors. *Nucl. Inst. Meth. Phys. Res.*, A355:329–341, 1995.

[53] T.F. Günzel et al. A silicon pad counter for first level triggering in ultra-relativistic proton-nucleus and nucleus-nucleus collisions. *Nucl. Inst. Meth. Phys. Res.*, A316:259–266, 1992.

[54] The CERES collaboration. CERES/NA45 status report. Technical report, 1994. CERN/SPSLC 94-2, SPSLC/M529.

[55] W. Chen et al. Performance of the multianode cylindrical silicon drift detector in the CERES NA45 experiment: First results. *Nucl. Inst. Meth. Phys. Res.*, A326:273–278, 1993.

[56] D. Irmscher. *Search for direct photons from S-Au collisions at* 200 *GeV/u.* PhD thesis, Heidelberg University, Heidelberg, Germany, 1994.

[57] R. Novotny. The BaF_2 photon spectrometer TAPS. *IEEE Trans. Nucl. Sc.*, 38(2):379–385, 1991.

[58] P.V.C. Hough. Methods and means for recognizing complex patterns. *U.S. Patent 3069654*, 1962.

[59] J. Seguinot and T. Ypsilantis. Photo-ionization and cherenkov ring imaging. *Nucl. Inst. Meth.*, 142:377–391, 1977.

[60] Review of particle properties. *Phys. Rev. D*, 50(3), 1994. Also available online on the WWW at: *http://www-pdg.lbl.gov/.*

[61] T. Francke et al. Particle identification by Cerenkov ring imaging using a neural network approach. *Nucl. Inst. Meth. Phys. Res.*, A307:47–51, 1991.

[62] T. Altherr and J. Seixas. Cerenkov ring recognition using a nonadaptable network. *Nucl. Inst. Meth. Phys. Res.*, A317:335–338, 1992.

[63] F. James and M. Roos. *Function Minimization and Error Analysis.* CERN, 89.12j edition, 1981. CERN Program Library entry D506.

[64] G. Agakichiev et al. Cherenkov ring fitting techniques for the CERES RICH detectors. *Nucl. Inst. Meth. Phys. Res.*, A371:243–247, 1996.

[65] N.I. Chernov and G.A. Ososkov. Effective algorithms of circle fitting. *Comp. Phys. Comm.*, 33:329–333, 1984.

[66] A. Bloch. *More Murphy's law*. Methuen edition, 1982.

[67] I. Ravinovich and G. Tel-Zur. The CERES event generator. WIS/CERES internal notes, 1993,1995.

[68] M. Aguilar-Benitez et al. Inclusive particle production in 400 GeV/c pp-interactions. *Z. Phys. C*, 50:405–426, 1991.

[69] M. Franke et. al. Neutral meson production in ultrarelativistic proton nucleus collisions. Technical report, Gesellschaft fuer Schwerionenforschung. Darmstadt, 1996. GSI ANNUAL REPORT, 96-1.

[70] The HELIOS collaboration. Low p_T π^0 and η production in p-Be interactions at 450 GeV. *6th international conference on Hadron spectroscopy - HADRON - 95*, 1995. Manchester, UK.

[71] V.V. Anisovich and V.M. Shckhter. Quark model for multiparticle and inclusive reactions. *Nucl. Phys.*, B55:455–473, 1973.

[72] Yu.M. Antipov et al. Analysis of experimental data on inclusive production of ρ^0 and ω mesons in the framework of certain theoretical models. *Sov. J. Nucl. Phys.*, 39(6):923–926, 1984. Yad. Fiz. 39, 1461–1465 (1984).

[73] J. Bartke et al. Eta and omega meson production in medium energy $\pi^{\pm}p$ and k^-p interactions. *Nucl. Phys.*, B118:360–370, 1977.

[74] R. Veenhof. *Low mass muon pair production in 450 GeV p-Be collisions*. PhD thesis, NIKHEF-H, Amsterdam, the Netherland, 1993.

[75] G.J. Gounaris and J.J. Sakurai. Finite-width corrections to the vector-meson-dominance prediction for $\rho \rightarrow e^+e^-$. *Phys. Rev. Lett.*, 21(4):244–247, 1968.

[76] N.M. Kroll and W. Wada. Internal pair production associated with the emission of high-energy gamma rays. *Phys. Rev.*, 98(5):1355–1359, 1955.

[77] M. Bourquin and J.M. Gaillard. Vector meson and ψ contributions to single lepton spectra. *Phys. Lett.*, 59B(2):191–196, 1975.

[78] M. Bourquin and J.M. Gaillard. A simple phenomenological description of hadron production. *Nucl. Phys.*, B114:334–364, 1976.

[79] D. Rohrich et al. Hadron production in S-Ag and S-Au collisions at 200 GeV/n. *Nucl. Phys.*, A566:35c–44c, 1994.

[80] J.G. Branson et al. Production of the J/ψ and $\psi\prime$ by 225-Gev/c $\pi^{\pm}$ and proton beams on C and Sn targets. *Phys. Rev. Lett.*, 38(23):1331–1334, 1977.

[81] C. Fuchs. PhD thesis, Heidelberg, Germany, 1996.

[82] G. Agakichiev et al. Enhanced production of low-mass electron pairs in 200 GeV/nucleon S-Au collisions at the CERN super-proton synchrotron. *Phys. Rev. Lett.*, 75(7):1272–1275, 1995.

[83] C.P. de los Heros. *Low-mass dielectron production in S-Au collisions at* 200 *GeV/n.* PhD thesis, Weizmann Institute of Science, Rehovot, Israel, 1996.

[84] G.Q. Li, C.M. Ko and G.E. Brown. Enhancement of low mass dileptons in heavy ion collisions. *Phys. Rev. Lett.*, 75:4007–4010, 1995. And Nucl. Phys. A, in press.

[85] I. Tserruya. Dileptons and photons at the CERN SPS. Proc. of the XXVI International Symposion on Multi-Particle Dynamics. September 1-5, 1996, Faro, Portugal. In press.

Index